

ABSTRACT

Title of Dissertation:

THE EFFECT OF PHASE CONSTITUTION AND MORPHOLOGY ON ROOM TEMPERATURE DEFORMATION BEHAVIOR OF BINARY TITANIUM ALLOYS

Zane William Wyatt, Doctor of Philosophy, 2011

Dissertation Directed By:

Professor Sreeramamurthy Ankem
Department of Materials Science and Engineering

Currently, titanium alloys are used in a variety of applications, including defense, aerospace, biomedicine, and even common consumer products such as bicycles and golf clubs. In many applications such as the landing gear of aircraft and geothermal energy production, titanium components may be subjected to stresses for extended periods of time. It has long been known that single-phase α (HCP), single-phase β (BCC), and two-phase $\alpha + \beta$ Ti alloys can creep at low temperatures ($<0.25T_m$). For this reason, creep is an important factor to consider when designing titanium alloys for various applications.

The first part of this investigation is concerned with single-phase α -Ti alloys. It was found that the twin size (lamellar thickness) decreases with an increase in strain rate. This behavior is unexpected based on the classical understanding of instantaneous twinning. This investigation was able to for the first time demonstrate a time-dependent twinning phenomenon during high strain rate tensile deformation.

The second part of this investigation is concerned with experimentally and theoretically studying low-temperature creep deformation behavior of two-phase $\alpha + \beta$ Ti alloys. Deformation mechanisms were seen in two-phase $\alpha + \beta$ Ti alloys that are not

present during creep of the respective single-phase alloys with compositions equivalent to the individual phases.

To investigate the possible interphase interaction stresses, 3D anisotropic Finite element modeling (FEM) was used. These simulations revealed that due to the Burgers orientation relationship between the two phases, deformation such as slip or twinning in the α phase can create very high additional shear stresses on different slip systems in the β phase. This work also revealed that the interfacial stresses that develop between the two phases during elastic deformation will often be much greater than the applied stress. These results were used to help explain the additional deformation mechanisms seen in two-phase alloys that are not seen in the respective single-phase alloys during creep.

This work was supported by the National Science Foundation under Grant Number DMR-0906994.

THE EFFECT OF PHASE CONSTITUTION AND MORPHOLOGY ON
ROOM TEMPERATURE DEFORMATION BEHAVIOR OF BINARY
TITANIUM ALLOYS

By

Zane William Wyatt

Dissertation submitted to the Faculty of the Graduate School of the
University of Maryland, College Park, in partial fulfillment
of the requirements for the degree of
Doctor of Philosophy
2011

Advisory Committee:

Professor Sreeramamurthy Ankem, Chair
Professor Abhijit Dasgupta, Dean's Representative
Professor Lourdes Salamanca-Riba
Professor Mohammad Al-Sheikhly
Professor Aris Christou

©Copyright by
Zane William Wyatt
2011

Acknowledgements

I first want to thank my wife, Renika, for your love, support, encouragement, and above all, patience. I'm fairly certain I would have lost my mind without your doses of reality. I would also like to thank my family—the people in my life who never once doubted my abilities and pushed me to always be better and continue to grow. A very special thank-you goes to Mom and Dad; two people who taught me that science is cool and hard work is rewarding.

I would like to thank my advisor, Dr. Ankem, for guiding my research and challenging my conclusions. I will remember the last minute deadlines just as fondly as the celebratory lunches afterward. I would like to thank the entire faculty and staff of the Materials Science and Engineering Department, the staff of the FabLab, and of the NISP lab at the University of Maryland; this place has been my home for over four years and all your efforts make it much more enjoyable. I also sincerely appreciate the time and effort of my Dissertation Committee for reviewing this work. One last shout-out goes to a very deserving Dr. Phil Piccoli for his help with the numerous microprobe sessions.

Big thanks go to my co-workers, particularly Will Joost, Paul Lambert, Alex Kao, and Ryan Mulholland, for their friendship, conversations, and laughs.

Finally, I am extremely grateful for the financial support of this Department and the NispLab which is supported in part by the National Science Foundation as a Materials Research Science and Engineering Center (MRSEC) Shared Experimental Facility. My ultimate financial acknowledgements go to the National Science Foundation who funded this work under Grant Number DMR-0906994.

Table of Contents

List of Tables	v
List of Figures	vi
Chapter 1: Introduction and Project Aims	1
Chapter 2: Technical Background	5
2.1 The α and β phases	
2.2 Low temperature deformation mechanisms of Ti alloys	
2.3 Plastic deformation of two phase alloys	
2.4 Elements of twinning	
2.5 Recent developments in α -Ti alloys	
2.6 Recent developments in β -Ti alloys	
2.7 Recent developments in two-phase Ti alloys	
2.8 What is not known, but should be	
Chapter 3: Experimental Procedures	17
3.1 Heat treatment	
3.2 Tensile and creep specimen preparation	
3.3 Attachment of fiducial grids	
3.4 Tensile testing	
3.5 Creep testing	
3.6 SEM and optical microscopy	
3.7 TEM sample preparation	
3.8 TEM procedures	
3.9 Manual calculation of resolved shear stress	
Chapter 4: Deformation Mechanisms and Kinetics of Time-Dependent Twinning in an α-Ti-1.6wt% V alloy	28
4.1 Crystallography of time-dependent twinning	
4.2 Time dependent twinning during creep of α -Ti-1.6V	
4.3 Model for diffusion of oxygen at twin front	
4.4 Model for stress-assisted interstitial diffusion in α -Ti	
4.5 Tensile testing results	
4.6 Optical and SEM microscopy	
4.7 TEM microscopy	
4.8 Effect of strain rate on twinning in α -Ti-1.6V	
4.9 Concluding remarks	
Chapter 5: The Effect of β-phase Metastability on Low Temperature Deformation Behavior of β and $\alpha + \beta$ Ti alloys	52
5.1 β -phase metastability	
5.2 Deformation mechanisms in metastable Ti alloys	

5.3 The role of β -phase stability on tensile deformation mechanisms	
5.4 The role of β -phase stability on creep deformation mechanisms	
5.5 Concluding remarks	
Chapter 6: Influence of Microstructure and the Second Phase on the Room Temperature Creep Deformation Mechanisms of $\alpha + \beta$ Ti-V Alloys	73
6.1 Experimental procedures	
6.2 Results	
6.3 Discussion	
6.4 Summary of creep deformation process	
6.5 Conclusions	
Chapter 7: Finite Element Studies of the Interaction Between α and β Phases in Two-Phase Ti Alloys	104
7.1 Input properties and model development	
7.2 Coordinate system development	
7.3 Geometry of the two-phase system	
7.4 Mesh generation	
7.5 Mesh generation incorporating slip or twinning in α	
7.6 Results	
7.7 Discussion	
7.8 Conclusions	
Chapter 8: Conclusions	128
Chapter 9: Suggestions for Future Work	131
Appendices	132
References	163
Curriculum Vitae	176

List of Tables

Table 4.1. Mechanical testing results of α -Ti-1.6V tested at different strain rates at 298K.

Table 4.2. Quantitative analysis of deformation twinning in selected area in α -Ti-1.6V tensile tested to 3% strain at 298K. The values for twin volume fraction are accurate to +/- 3%.

Table 4.3. Results of the experimental calculations and results of the constitutive relations for twinning observed during the tensile investigations. The modified constitutive relation incorporated a stress factor into the predictive equation described by Eq. (4.2).

Table 7.1. Maximum resolved shear stresses in β Ti, normalized to applied stress in α , on twinning and hexagonal martensite shear systems.

List of Figures

Figure 2.1. Titanium rich end of the Ti-V phase diagram and respective alloy compositions used in this investigation [2, 3].

Figure 2.2. Schematic illustration of planes and directions associated with twinning.

Figure 2.3. Schematic illustration of $\{10\bar{1}2\}$ twinning in the HCP lattice of α -titanium. Projection of the lattice is onto the $\{11\bar{2}0\}$ plane. (a) Shear of the lattice in the $\langle\bar{1}10\bar{1}\rangle$ direction moves only atoms in **A**-type sites (blue) directly to twinned position. (b) Arrows give the shuffles required to move the atoms in **B**-type sites (red) to either the **B** (red) or **C**-type sites (green) in the twinned lattice. Reorientation of the lattice will eliminate the octahedral sites (marked with an 'X') where an oxygen atom could reside. These models are an extension of earlier twinning models by Song and Gray [43, 44], but now include the corresponding movements of octahedral sites [45].

Figure 2.4. Projection of bcc substitutional and octahedral interstitial atoms onto $(1\bar{1}0)$ plane. (a) Untwinned structure showing direction of $[113]$ twinning shear, and (b) Final twinned structure showing mirror symmetry across twin-matrix interface [23].

Figure 2.5. (a) TEM micrograph and (b) SEM image showing connection between twinning in α -phase and stress induced martensite in β -phase [21, 22].

Figure 2.6. High resolution TEM (HREM) micrograph of the slightly rough, semi-coherent α/β interface of Ti-8.1V, viewed from the $[1\bar{2}10]_{\alpha} // [1\bar{1}1]_{\beta}$ direction [21, 22].

Figure 2.7. High resolution TEM micrograph showing the interface of stress induced martensite (α') and the α phase. Notice the $\{10\bar{1}1\}$ twin relationship between the phases. Selected area diffraction patterns from each phase and the interface taken parallel to the $(1\bar{2}10)$ zone axis are inset. [21, 22]

Figure 4.1. Schematic illustration of $\{10\bar{1}2\}$ twinning in the HCP lattice of α -titanium. Projection of the lattice is onto the $\{11\bar{2}0\}$ plane. (a) Shear of the lattice in the $\langle\bar{1}10\bar{1}\rangle$ direction moves only **A**-type Ti atoms (large, dark circles) directly to twinned positions. (b) Arrows give the shuffles required to move the Ti atoms in **B**-type sites (large, lighter circles) to their twinned **B**-type or **C**-type positions. Reorientation of the lattice eliminates the octahedral sites (small circles with "x" mark) where oxygen could reside. (c) Schematic illustration of a completed $\{10\bar{1}2\}$ twinning event. The completed positions for **B**-type Ti atoms and the corresponding possible octahedral sites and the completed positions for **C**-type Ti atoms and the corresponding possible octahedral sites are indicated by the arrows. These models are an extension of earlier twinning models by Song and Gray (Song and Gray, 1995b,c), but now include the corresponding movements of octahedral sites where oxygen may reside [45].

Figure 4.2. Mechanical testing results of α -Ti-1.6V tested at different strain rates. (a) True stress – true strain curves of alloy tested at different strain rates. (b) Strain hardening rate of the plastic region of each of the curves. The alloy exhibits a low strain hardening rate for all tested strain rates.

Figure 4.3. Before and after optical micrographs of deformation twinning in α -Ti-1.6V at (a) 10^{-1} /s, (b) 10^{-2} /s, (c) 10^{-4} /s, and (d) 10^{-6} /s. All samples were tested to 3% strain. All micrographs were taken at 100x magnification. The fiducial grids are 50 μ m square. Note the gradual increase in twin thickness as the strain rate decreases, as indicated by the arrows.

Figure 4.4. Optical micrograph taken under different polarizing light conditions of α -Ti-1.6V, showing multiple twins. $T = 298\text{K}$, $\varepsilon = 3.0\%$, strain rate = 10^{-6} /s. The fiducial grids are 50 μ m square. Note twins at the arrows which disappear under non-polarized light. This method of twin identification was used for the other strain rates as well but is not shown here.

Figure 4.5. Bright field TEM micrograph from tensile deformed α -Ti-1.6V, of $\{1102\}$ twin and SADPs of the $\{2\bar{1}\bar{1}0\}$ foil plane from: (a) the untwinned matrix, (b) inside the twin, and (c) across the twin-matrix interface. $T = 298\text{K}$, $\varepsilon = 3.0\%$, strain rate = 10^{-1} /s.

Figure 4.6. Bright field TEM micrograph from tensile deformed α -Ti-1.6V, of $\{1102\}$ twin with $[2\bar{1}\bar{1}0]$ zone axis. $T = 298\text{K}$, $\varepsilon = 3.0\%$, strain rate = 10^{-1} /s. Note the twin indicated by the arrow.

Figure 4.7. Optical micrograph from tensile deformed α -Ti-1.6V. $T = 298\text{K}$, $\varepsilon = 3.0\%$, strain rate = 10^{-1} /s. Note the very fine twins indicated by arrows.

Figure 5.1. A schematic of a pseudo-binary equilibrium diagram showing the ranges of β and ω stability as a function of added β stabilizer [119].

Figure 5.2. Selected area diffraction pattern comparing the degree of formation of omega phase in the β phase of the $\alpha + \beta$ (a) Ti-6.0 wt pct Mn (β -phase MoE=19.9) and (b) Ti-8.1 wt pct V (β -phase MoE=9.9) alloys. Note pre-omega-phase streaking of ω spots of the β phase of $\alpha + \beta$ Ti-6.0 wt pct Mn SADP, which are consistent with incommensurate ω formation, compared with the sharply defined spots of the β -phase $\alpha + \beta$ Ti-8.1 wt pct V SADP. The ω phase indices and orientation are provided. The extra spots in the Ti-8.1V pattern are due to double diffraction [21, 22, 156].

Figure 5.3. Illustration of the $[1\bar{2}10](0001)//[1\bar{1}1](110)$ Burgers orientation relationship between the α and β phases in an $\alpha + \beta$ titanium alloy with Widmanstatten microstructure. Diagram shows the $(0001)_\alpha$ and $(110)_\beta$ planes. The interface plane is $(\bar{5}140)//(334)$; which is normal to the $(0001)_\alpha$ and $(110)_\beta$ planes and is indicated as a trace in each phase [21, 22].

Figure 5.4. Elastic interaction stress on α and β phases of a titanium alloy. The interaction of the stronger but lower modulus β phase with the α phase initially increases the stress in α . Once significant plastic deformation occurs in α , elasto-plastic interaction stresses act on the β phase [21, 22].

Figure 6.1. SEM micrograph of $\alpha + \beta$ Ti-8.1V with Widmanstätten microstructure before testing; showing fiducial grid used in these investigations.

Figure 6.2. Tensile curves of Ti-4.3wt% V, tested at a strain rate of 3.28×10^{-5} /s to a 3% total strain.

Figure 6.3. Creep curves of Ti-4.3V alloys, creep tested at ambient temperature at 95% of their respective YS.

Figure 6.4. SEM micrographs of $\alpha + \beta$ Ti-4.3V (a) before and (b) after creep deformation at 95% YS for 200 hours to 0.86% total plastic strain. There are no coarse deformation features visible on the polished and etched surface, although fine slip in the α phase (light) was noted due to an increase of the fiducial line spacing during testing.

Figure 6.5. Bright field TEM micrograph of fine slip lines in the α -phase of Ti-4.3V. Slip is $\langle a \rangle$ type dislocations on prism planes. The dislocations are of the type $\mathbf{b} = 1/3\langle 11\bar{2}0 \rangle$.

Figure 6.6. SEM micrographs of $\alpha + \beta$ Ti-4.3V with Widmanstätten microstructure (a) before and (b) after creep testing at 95% YS for 200 hours to 0.90% total plastic strain. Note the coarse deformation features spanning multiple α (light) and β (dark) grains. These were identified during this study as stress induced martensite in the β phase and coarse slip or twinning in the α phase.

Figure 6.7. SEM micrograph of $\alpha + \beta$ Ti-4.3V with Widmanstätten microstructure creep tested to 0.90% total plastic strain. Note the coarse deformation features spanning the α (light) and β (dark) phases. These features were identified as coarse slip and twinning in the α phase and stress induced martensite (α') in the β phase.

Figure 6.8. TEM bright field micrograph of slip bands in the β phase of $\alpha + \beta$ Ti-8.1V with Widmanstätten microstructure.

Figure 6.9. TEM bright field micrograph showing a hexagonal martensite plate (α') in the β phase connected to a $\{10\bar{1}2\}$ type twin in the α phase. The twin was classified specifically as $(\bar{1}012)[10\bar{1}1]$. Accompanying diffraction patterns are from the (a) α /twin interface and (b) the α'/β interface. Zone axis is $[1\bar{2}10]_{\alpha} // [1\bar{1}1]_{\beta}$.

Figure 6.10. Bright field TEM micrograph showing three stress induced hexagonal martensite plates (α') within the β phase of Ti-8.1V creep tested at 95% YS for 200 hours.

Accompanying diffraction patterns show that both planes have a near{10 $\bar{1}$ 1} twin relationship to the α phase. The zone axis is $[1\bar{1}1]_{\beta} // [1\bar{2}10]_{\alpha}$.

Figure 6.11. Tensile curves of Ti-8.1wt% V, tested at a strain rate of 3.28×10^{-5} /s to a 3% total strain.

Figure 6.12. Creep curves of Ti-8.1V alloys, creep tested at ambient temperature at 95% of their respective YS.

Figure 6.13. SEM micrographs of $\alpha + \beta$ Ti-8.1V (a) before and (b) after creep deformation at 95% YS for 200 hours to 0.41% total plastic strain. Note the coarse deformation features in the β phase (dark). These features were identified to be coarse slip and stress induced martensite. Fine slip has been noted in the α phase (light) due to an increase in the fiducial line spacing during testing. Note that deformation features do not cross phase boundaries.

Figure 6.14. SEM micrographs of $\alpha + \beta$ Ti-8.1V (a) before and (b) after creep deformation at 95% YS for 200 hours to 0.41% total plastic strain. Note the coarse deformation features in the β phase (dark). These features were identified to be coarse slip and stress induced martensite. Fine slip has been noted in the α phase (light) due to an increase in the fiducial line spacing during testing. Twinning in the α phase was also noted, but was rare.

Figure 6.15. Bright field TEM micrograph of stress induced hexagonal martensite (α') plate in the β phase of Ti-4.3V. To the right are selected area diffraction patterns taken from the (a) β phase and (b) α' plate. The zone axis is $[1\bar{1}1]_{\beta} // [1\bar{2}10]_{\alpha}$.

Figure 6.16. SEM micrographs of $\alpha + \beta$ Ti-8.1V with Widmanstätten microstructure (a) before and (b) after creep testing at 95% YS for 200 hours to 0.52% total plastic strain. Note the coarse deformation features spanning many grains. These features were identified to be twinning or coarse slip in the α phase (light) and stress induced martensite in the β phase (dark).

Figure 6.17. Bright field TEM micrograph showing stress induced martensite plates in the β phase and twins in the α phase of Ti-8.1V with Widmanstätten microstructure. The martensite plates and twins alternate across the width of the β and α grains [22].

Figure 6.18. Tensile curves of Ti-12.6wt% V, tested at a strain rate of 3.28×10^{-5} /s to a 3% total strain.

Figure 6.19. Creep curves of Ti-12.6V alloys, creep tested at ambient temperature at 95% of their respective YS.

Figure 6.20. SEM micrographs of $\alpha + \beta$ Ti-12.6V (a) before and (b) after creep deformation at 95% YS for 200 hours to 0.11% total plastic strain. Note the stress induced plates (SIP) in the β phase (dark) and lack of coarse deformation features in the α phase (light).

Figure 6.21. TEM micrograph of $\alpha + \beta$ Ti-12.6V showing diffraction of stress induced plate which is $\{3\bar{2}3\}[131]$ twin. The additional spots are from the ω phase and double diffraction.

Figure 6.22. SEM micrograph of $\alpha + \beta$ Ti-12.6V after creep deformation at 95% YS for 200 hours to 0.11% total plastic strain. Note the stress induced plates (SIP) and coarse slip in the β phase (dark) and lack of coarse deformation features in the α phase (light). The SIP are $\{332\}\langle 113\rangle$ twins.

Figure 6.23. SEM micrographs of $\alpha + \beta$ Ti-12.6V (a) before and (b) after creep deformation at 95% YS for 200 hours to 0.12% total plastic strain. Note the stress induced plates (SIP) in the β phase (dark) connected to deformation twinning in the α phase (light).

Figure 6.24. TEM micrograph of $\alpha + \beta$ Ti-12.6V alloy with Widmanstätten microstructure with $\{332\}\langle 113\rangle$ twinning. Alloy was creep tested at 95% YS for 200 hours. Diffraction pattern was taken from inside the twin. Zone axis is $\langle 110\rangle$.

Figure 6.25. SEM micrographs of $\alpha + \beta$ Ti-12.6V (a) before and (b) after creep deformation at 95% YS for 200 hours to 0.12% total plastic strain. Note the stress induced plates (SIP) in the β phase (dark) connected to deformation twinning in the α phase (light) and no visible deformation in the α phase.

Figure 6.26. Composite graph of the creep curves of the two different microstructures for the three different alloys. As shown, the effect of microstructure decreases with increasing volume fraction of β phase.

Figure 6.27. Graph showing the relationship between creep strain of the alloys compared with what the law of mixtures would predict. As shown, the β phase exerts a much stronger influence on alloy behavior than predicted.

Figure 6.28. A graph of the creep constants from the equation $\epsilon = A' + B \ln(t)$ for each of the tests during this investigation. As shown, the constants do follow general self-consistent trends.

Figure 7.1. A stereographic projection showing the interface plane $(\bar{5}140)//(\bar{3}34)$, Burgers orientation relationships $\langle 1\bar{2}10\rangle(0001)//\langle 1\bar{1}1\rangle(110)$, the standard crystallographic orientations and the prime coordinates (Widmanstätten orientation) for the FEM models in this investigation.

Figure 7.2. Test scenario schematic showing coordinate system orientation and reference points A-N for the bicrystal model base used in this investigation.

Figure 7.3. ANSYS bicrystal meshed for the study of elastic interactions between α (blue) and β (red) phases of titanium alloys.

Figure 7.4. A stereographic projection showing the relationship between the orientation of the α phase in the ANSYS coordinate system, and the orientation of the twinned region in the ANSYS coordinate system.

Figure 7.5. A schematic diagram showing the relationship between the twinning and basal slip systems to the oriented model in the ANSYS simulation.

Figure 7.6. ANSYS bicrystal meshed for the study of elastic interactions between α (blue), α twin (purple), and β (red) phases of titanium alloys.

Figure 7.7. Displacements of the nodes in the Y' direction. Note that the displacement of the top nodes is appropriate for the elastic compliance values in the $[0001]$ direction for an applied stress of 359 MPa.

Figure 7.8. Normal stresses in the Y' direction. Note the higher stresses in the α phase as opposed to the β phase.

Figure 7.9. Resolved YZ shear stress for elements in the two-phase titanium bicrystal shown in Figure 7.6. Note the interaction stresses at the interface.

Figure 7.10. The resolved shear stress distribution for a horizontal row of elements in the mesh shown in Figure 7.3. α phase is on the left and β phase is on the right. Notice the very high interaction stresses at the interface.

Figure 7.11. The resolved shear stress distribution for a horizontal row of elements in the mesh shown in Figure 7.3. Note that for this orientation of β phase, the resolved shear stress on the martensite system is higher than on the twinning system.

Figure 7.12. The ANSYS simulation results of stresses in the Y' direction. Note that the stresses have been relieved in the twin (as appropriate) and the α phase experiences higher stresses than the β phase.

Figure 7.13. The resolved YZ shear stress nodal results as produced by the ANSYS simulation. Note increase in interfacial shear stresses as well as the stresses on the twinning planes.

Figure 7.14. The resolved shear stress distribution for a horizontal row of elements between points “Q” in the schematic shown in Figure 7.5. Note that for this orientation of β phase, the resolved shear stress on the martensite system is higher than on the twinning system and the presence of a twin magnifies that effect.

Figure 7.15. The resolved shear stress distribution for a horizontal row of elements along line “S” in the schematic shown in Figure 7.5.

Chapter 1

Introduction and Project Aims

Titanium (Ti) and its alloys are technologically important. With applications in various areas such as aerospace, naval, industrial, and biomedical, the superior specific strength, excellent corrosion resistance and biocompatibility of these materials is making them more and more popular. Its higher cost compared to aluminum or steel is justified by its performance. Products using titanium alloys can now be found in sports equipment, architecture, fashion, and electronics, and the applications for titanium alloys are certain to grow in the 21st century, making it critical to understand the microstructure and mechanical behavior of these alloys.

Over the years, considerable research has been performed examining and seeking to improve the mechanical properties of titanium. For the purpose of this investigation, low temperature will be defined as less than $0.25 \cdot T_m$, where T_m is the melting temperature of the material in question (1941 K for Ti). Many previous studies have been performed to examine the low-temperature tensile deformation mechanisms of single-phase α and β , as well as two-phase $\alpha + \beta$ titanium alloys. These $\alpha + \beta$ and β titanium alloys are specifically important because they have excellent mechanical properties including a high strength to weight ratio. However, in many of these applications, low temperature creep resistance is an important factor. It has long been known that titanium alloys may plastically deform over time under constant load, or creep, at low temperatures, which could compromise the mechanical reliability of titanium components. Creep is an important consideration in high-pressure vessels,

aircraft components, structural components and artificial joints such as hips or knees. Given the importance of reliability in these cases, it is vital to understand the deformation mechanisms of Ti alloys under these conditions. In this sense, the tensile strength and creep resistance of the two-phase $\alpha + \beta$ Ti alloys are dependent upon a number of parameters such as microstructure, the properties of the component phases, interactions between phases, and β -phase stability.

There is currently a lack of understanding regarding some of the fundamental aspects of low temperature deformation of Ti alloys, which will be addressed in this investigation. Of particular interest in this investigation is deformation twinning. Slow twin growth (hereafter known as time-dependent twinning) has been identified as a low temperature creep deformation mechanism in coarse grained ($>200 \mu\text{m}$) single-phase α and single-phase β titanium alloys. Furthermore, time-dependent twinning itself is unusual because twinning is classically understood as a deformation mechanism which occurs at speeds close to the speed of sound in the material (5,090 m/s in Ti) and only at high strain rates or very low (cryogenic) temperatures. It has been suggested in previous investigations that interstitial impurities, particularly oxygen, may be responsible for slow twin growth and some crystallographic models were developed to explain this.

In regard to two-phase titanium alloys, it was found that the deformation mechanisms in these alloys could be quite different from those of the single-phase alloys. The reasons for this unexpected behavior are not known. A clear understanding of this behavior will lead to the development of new titanium alloys for improved low temperature creep resistance and specific strength. To address some of these issues, a systematic investigation has been undertaken. The unique aspect to this investigation is

the combination of both experimental and theoretical studies to build a model of twinning-based deformation in titanium alloys. The specific aims and components of this investigation are as follows:

1. Carry out tensile studies with varying strain rates (10^{-6} - 10^{-1} /s) on an α -Ti-1.6wt% V alloy to determine what effect if any strain rate has on deformation twinning. If there is an effect, determine how this effect be related to the time-dependent twinning phenomena observed during creep deformation of this alloy.
2. Determine the tensile and creep properties at 298 K of $\alpha + \beta$ Ti-8.1wt% V ($\sim 50\%$ α , 50% β) with a fine-grained equiaxed type microstructure. Compare these properties with those of the same alloy with a Widmanstätten microstructure. Determine how the results would best help us optimize the microstructure for improved low temperature creep resistance.
3. Carry out tensile and creep studies at 298 K of the $\alpha + \beta$ Ti alloys Ti-4.3wt% V ($\sim 80\%$ α , 20% β) and Ti-12.6wt% V ($\sim 17\%$ α , 83% β) for both Widmanstätten and equiaxed microstructures. This information will help in optimizing the volume fraction of phases and morphology for improved low temperature creep resistance.
4. Systematically identify and characterize the deformation products by optical, scanning electron microscopy (SEM), and transmission electron microscopy (TEM), with a particular focus on the interactions between deformation mechanisms and how the microstructure (i.e. grain size or orientation) or volume fraction of phases may affect creep behavior.

5. Determine the effect of interphase interactions for both Widmanstätten and equiaxed microstructures with three-dimensional anisotropic finite element (FEM) modeling of the elastic interaction stresses between the inter-phase interfaces of α/β , twin in α /martensite in β , and twin in α /twin in β .

A thorough literature review and technical background is provided in Chapter 2. Chapter 3 gives an outline of the experimental procedures. The results and discussion of the strain rate effect of twinning in α -Ti alloys is provided in Chapter 4. Chapter 5 is a comprehensive review of the effect of the second phase on low temperature deformation mechanisms. The results and discussion of the experimental work with regard to creep and tensile testing of two-phase Ti alloys are contained in Chapter 6. Chapter 7 provides the FEM analysis of the experimental work seen in the earlier chapters. Lastly, Chapter 8 gives the main conclusions and Chapter 9 provides some potential avenues for future work.

Chapter 2

Technical Background

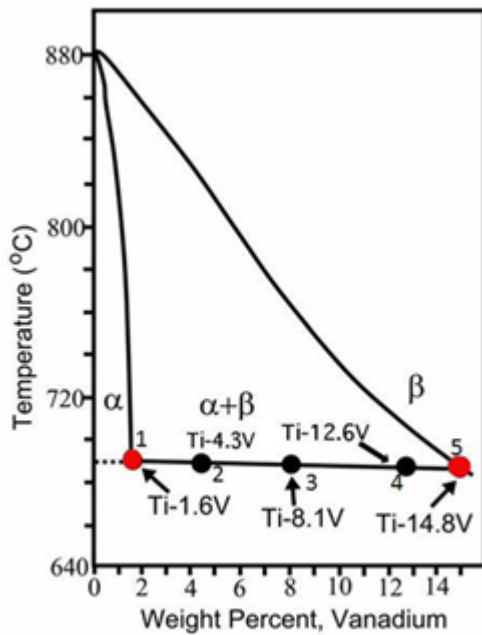
This chapter consists of a brief review of titanium, titanium alloys, titanium phases, creep deformation behavior, and the previous studies which are most relevant to the present investigation.

2.1 The α and β phases

The titanium α -phase is a hexagonally close packed (HCP) crystal structure. The titanium β -phase is a body centered cubic (BCC) structure. Pure titanium will undergo an allotropic phase transformation from $\alpha \rightarrow \beta$ as the temperature is increased above 1156 K (883°C). Alloying elements are most often added to pure titanium to enhance its material properties. Elements that have little effect or increase the transformation temperature are called α -stabilizers, where elements that decrease this transformation temperature are called β -stabilizers. Elements that have been shown to stabilize the α -phase include Al, Ga, Sn, and O [1]. Elements that have been shown to stabilize the β -phase are generally transition metals and noble metals, including, V, Nb, Ta, Mo, and Mn [1].

As mentioned before, titanium alloys can be commercially available as either a single phase α or β microstructure, or present as a two-phase $\alpha + \beta$ microstructure of several different morphologies. Single-phase titanium alloys have very good mechanical properties; however, they are often characterized by a lower strength to weight ratio than other alloys available. The β alloys, like other BCC metals have a ductile to brittle

transformation temperature, and have some processing difficulties including the inherent instability of the β -phase. Two-phase alloys have the advantage of desirable mechanical properties as well as stabilized phases. The two-phase alloys used in this study are β -stabilized binary alloys that have a sufficient amount of β -stabilizing element to retain the β -phase upon quenching; the α -phase is then nucleated and grown by heat-treatment in the $\alpha + \beta$ field of the phase diagram, as shown in Figure 2.1 [2, 3].



ALLOY	ALLOYING ELEMENT	PHASES
	V (wt%)	
1*	1.6	~ 100% α
2	4.3	~80% α , 20% β
3	8.1	~50% α , 50% β
4	12.6	~17% α , 83% β
5*	14.8	~100% β

Figure 2.1. Titanium rich end of the Ti-V phase diagram and respective alloy compositions used in this investigation [2, 3].

2.2 Low temperature deformation mechanisms of titanium alloys

Various mechanical properties of two-phase alloys, including low temperature creep, have been recently reviewed by Ankem *et al* [4]. Among these two-phase alloys, titanium alloys are of particular interest. The attractive properties of titanium and its alloys include: high strength to weight ratio, excellent corrosion resistance, and biocompatibility. For these reasons, they are used in a number of high technology areas. In many of these applications, components are subjected to constant loads over extended periods of time at low temperatures ($<0.25T_m$). For example, titanium alloys were being considered as candidate materials for use in the nuclear waste storage system at the Yucca Mountain Nuclear Waste Repository [5], titanium alloys make up a large fraction by weight of the F-35 Joint Strike Fighter (JSF) [6], the largest fraction by weight of any material in the F-22 series of military fighter jets [7], and titanium alloys are used extensively in the biomedical field [8-13]. Additionally, there are many other applications where low temperature creep is important, including pressurized fuel tanks found in satellites [14].

In addition to creep deformation leading to creep failure, creep deformation can also affect other failure modes such as fatigue failure and stress corrosion cracking. This is due to the fact that low temperature creep deformation can result in such features as twins and martensite [15-25] that can act as fatigue crack initiation sites. There are many deformation mechanisms which play a role during creep of titanium. In regards to α titanium alloys, it was found that slip and time-dependent twinning play a significant role [15, 24]. Further, it was shown that a decrease in grain size results in a decrease in time-dependent twinning and hence lower creep strain [15, 24]. Similarly, in the case of β

titanium alloys, both slip and time-dependent twinning were found to be important mechanisms [17, 23, 25]. A decrease in grain size in β alloys was also found to decrease creep strain as in α alloys [17, 23, 25]. Further, it has been shown that for a given grain size, an increase in stability of the metastable β alloy will result in a decrease in creep strain [17, 23, 25].

In regard to $\alpha + \beta$ titanium alloys, the deformation mechanisms found include: slip, interface sliding, twinning, and stress-induced martensite formation [21, 22]. Additional deformation mechanisms were found in α and β phases of $\alpha + \beta$ alloys when compared to deformation mechanisms in the single-phase α and β alloys [21, 22]. The reasons for this are not known. In addition, the creep strain of the $\alpha + \beta$ alloy with low stability of the β phase was found to be high. It is important to know how the morphology and volume fraction of the phases affects the creep mechanisms and hence creep strains in the $\alpha + \beta$ alloys with low stability of the β phase. This is the focus of the present investigation. The outcomes of the investigation will be of great help in designing new titanium alloys and optimizing the processing parameters of the existing alloys for improved low temperature creep resistance.

2.3 Plastic deformation of two phase titanium alloys

The deformation behavior of two-phase alloys depends upon the properties of the component phases, the morphology and volume fraction of the component phases and the orientation of the interface between the phases. When two-phase alloys are subjected to a stress, the individual phases deform differently, resulting in elastic, elasto-plastic, and

plastic deformation [26]. Therefore, deformation in these two-phase alloys is a process that cannot be modeled just on individual phase deformation and the rules of mixing.

One characteristic of titanium alloys is that they are prone to creep at low temperatures ($<0.25T_m$) and at low stresses [27-29]. Creep can cause failure in components by a change in dimensional tolerances [29-36]; oftentimes, components that depend heavily on titanium, such as aircraft landing gear, require precise part tolerances so predicting low temperature creep becomes very important. Creep in α -titanium alloys has been primarily explained by slip [33]. However, in comparison with α -titanium, studies of low temperature creep in β and near- β alloys have been very limited with a few exceptions [17, 18, 25, 37-40]. Creep studies of two-phase titanium alloys have primarily concerned commercial alloys [29, 30, 32-36, 41], and have been attributed to slip in the individual phases as well as across the interphase boundaries.

2.4. Elements of Twinning

As twinning will be the focus of the majority of this investigation, the elements of twinning will be reviewed here. According to the classical theory of deformation, the original untwinned (matrix) lattice is transformed by displacements which are equivalent to, or an integral fraction of, a simple shear of the lattice points [42]. There are two planes which are not distorted by the shear of the lattice. One of these, denoted \mathbf{K}_1 , is referred to as the twinning plane and the shear direction is given by $\boldsymbol{\eta}_1$. The second undistorted, or conjugate plane is denoted \mathbf{K}_2 . The plane of shear, \mathbf{P} , contains $\boldsymbol{\eta}_1$ and the normals to \mathbf{K}_1 and \mathbf{K}_2 . The intersection of \mathbf{K}_2 and \mathbf{P} gives the conjugate or reciprocal shear direction, $\boldsymbol{\eta}_2$. When describing a twin, it is typical to identify the twin by the shear

plane, \mathbf{K}_1 and the shear direction, $\boldsymbol{\eta}_1$, i.e. $\{hkl\}\langle uvw \rangle$. Twins are typically classified as Type I or Type II depending on the nature of the twinning elements [42]. The planes and directions associated with twinning are schematically illustrated in Figure 2.2.

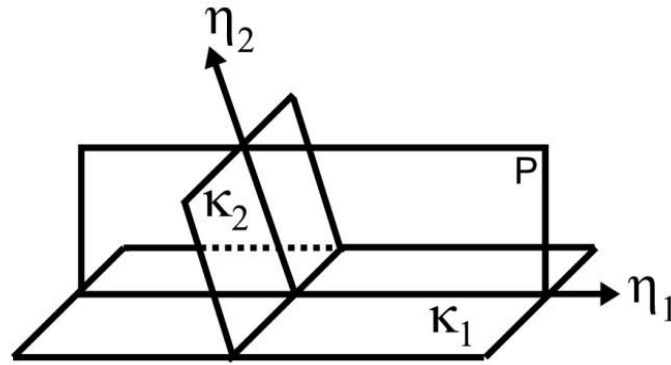


Figure 2.2. Schematic illustration of planes and directions associated with twinning.

2.5. Recent developments in α -Ti alloys

When an α -Ti-1.6V alloy with a coarse grain size ($225\mu\text{m}$) was creep deformed in tension at a stress level of 95%YS and 298 K, time-dependent twinning was observed [15, 24]. Similar phenomena were also observed earlier in a coarse-grained α -Ti-0.4wt% Mn alloy [16, 20]. To prove that the features observed were indeed twins, TEM investigations were carried out [24].

The next question is why the twins grow so slowly. It has been traditionally believed that twins grow at speeds approaching the speed of sound. To understand this phenomenon, a crystallographic model was developed. The model in Figure 2.3 is an extension of the model proposed by Song and Gray [43-45], where the movement of

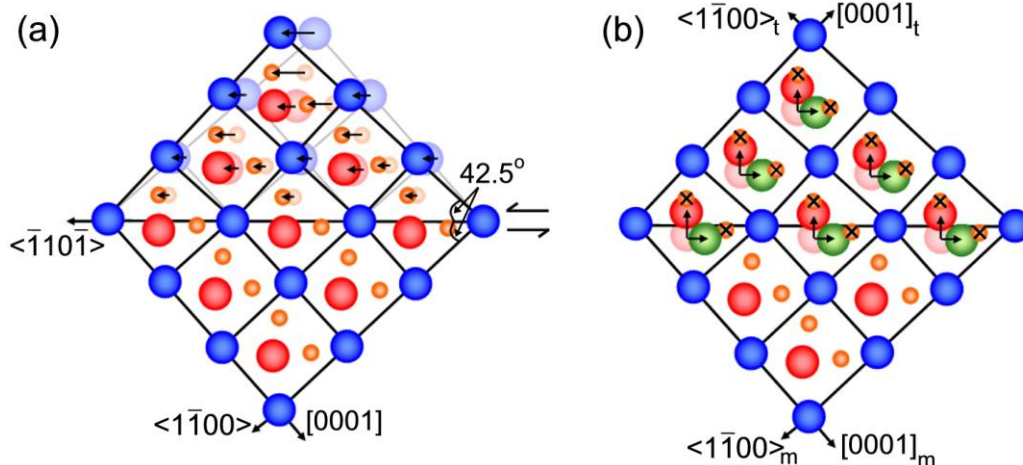


Figure 2.3. Schematic illustration of $\{10\bar{1}2\}$ twinning in the HCP lattice of α -titanium. Projection of the lattice is onto the $\{11\bar{2}0\}$ plane. (a) Shear of the lattice in the $\langle\bar{1}10\rangle$ direction moves only atoms in **A**-type sites (blue) directly to twinned position. (b) Arrows give the shuffles required to move the atoms in **B**-type sites (red) to either the **B** (red) or **C**-type sites (green) in the twinned lattice. Reorientation of the lattice will eliminate the octahedral sites (marked with an 'X') where an oxygen atom could reside. These models are an extension of earlier twinning models by Song and Gray [43, 44], but now include the corresponding movements of octahedral sites [45].

interstitial sites in addition to the movement of the parent atoms are shown. This figure shows that none of the octahedral sites are conserved, i.e. they are all displaced. What this means is that if oxygen is present at these interstitial sites, the oxygen atoms will interfere with the twin propagation, and the oxygen must diffuse away from the twin/matrix interface before the twin can grow. Therefore, originally a shear and shuffle process for the formation of the twin, is now controlled by the diffusion process of oxygen atoms. If indeed the oxygen diffusion controls the twin growth, then the activation energy for the twin growth would correspond to the activation energy of oxygen diffusion in α -Ti. The activation energy of twin growth in α -Ti was calculated by measuring individual twin growth rates. This activation energy was found to be 66 kJ/mol [24]. This activation energy was compared to the activation energy of diffusion

of oxygen in α -Ti. At 298K, the experimentally measured activation energy for oxygen in α titanium ranges from about 65 - 200 kJ/mol [46]. The low end of this range is close to the value of the model, suggesting that the growth of twins is controlled by the diffusion of oxygen. Details are reported by Oberson and Ankem [24].

2.6. Recent developments in β -Ti alloys

Similar to α -titanium alloys, it was found that twinning also plays a significant role in the low temperature creep behavior of some coarse-grained β -titanium alloys, depending on the stability of the β phase [17, 23]. In these investigations [17, 23], the creep behavior of a coarse-grained β -Ti-14.8V with a grain size of 350 μm was studied which was deformed at 95% yield stress and at 298 K. It was found that slip as well as $\{332\}\langle 113\rangle$ twinning are the major deformation mechanisms [17, 23, 25]. Similar to α titanium alloys, a detailed crystallographic mechanism was proposed for the growth of twins, the results of which are shown in Figure 2.4. These results show that oxygen can play a significant role in controlling the growth of twins; thereby controlling the extent of creep strain. A comparison for the activation energy of diffusion of oxygen in β -titanium and a calculated activation energy based on the twin growth rates suggests that the growth of twins is controlled by the diffusion of oxygen in BCC titanium as well. As in the case of α -titanium, the predominant deformation mechanism at the beginning of the creep deformation process was found to be slip, followed by slip and twinning at later stages of deformation [23].

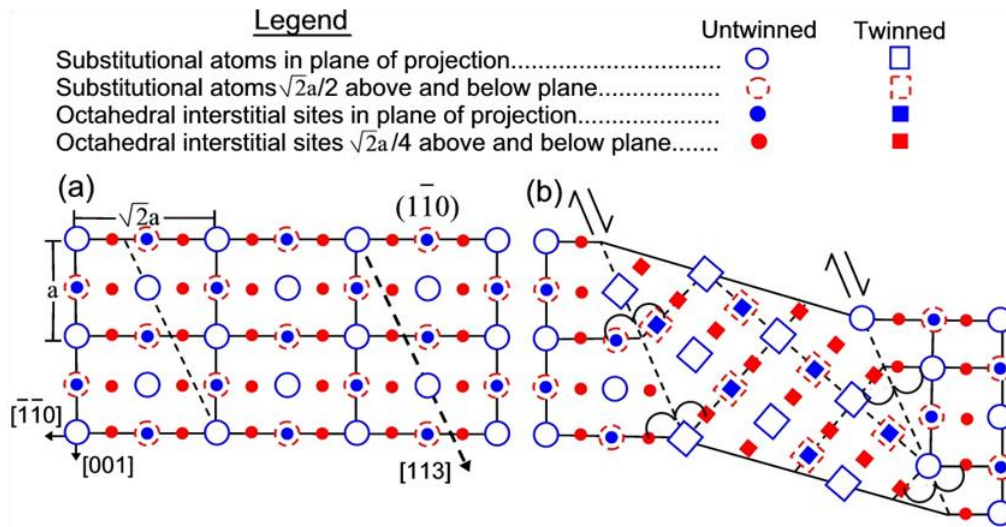


Figure 2.4. Projection of bcc substitutional and octahedral interstitial atoms onto $(1\bar{1}0)$ plane. (a) Untwinned structure showing direction of $[113]$ twinning shear, and (b) Final twinned structure showing mirror symmetry across twin-matrix interface [23].

2.7. Recent developments in two-phase Ti alloys

In regard to $\alpha + \beta$ titanium alloys, it was found that the deformation mechanisms could be quite different from those observed in single-phase α and β alloys. For example, in the case of 51% α - 49% β Ti-8.1V, with Widmanstätten $\alpha + \beta$ microstructures, creep deformation mechanisms were found to be twinning in α and stress-induced martensite in β [21, 22]. The creep tests were conducted at 95% YS at room temperature (298 K).

There were at least two surprising results here. First, twinning along with slip was found to be the major deformation mechanisms in single phase α -Ti-1.6V where the grain size was $>60 \mu\text{m}$ [15]. However, in the case of this two-phase alloy, twinning was observed in α even though the α plate thickness is about $3.0 \mu\text{m}$ (twinning was not previously seen in small grain size α -Ti alloys). Second, in the case of the single-phase β alloy discussed above, twinning, along with slip were found to be the major mechanisms.

However, in this two-phase alloy, stress induced martensite was found to be a major mechanism in the β phase, a phenomenon which had not previously been seen [21, 22].

2.8. What is not known, but should be

The interesting results from Section 2.7 were explained on the basis of elastic interaction stresses [4, 21, 22], but there are still many unknowns. For example, as shown in Figures 2.5, 2.6, and 2.7, the twins in α are connected to the martensite in β and it is not known which one started first or how these interfaces will change with a change in volume fraction of the phases. Further, it is not known how these elastic interactions decay from the α/β interface. In addition, it is not known if such combination of twinning in α and stress-induced martensite (α') in β will exist if the morphology of α and β phases are changed from the morphology shown in Figure 2.4, to equiaxed microstructure. Furthermore, it is not known which one is the slower process: twinning in α or stress induced martensite in β . The slower of the two processes will control the extent of creep deformation. In the proposed investigation, all these issues will be addressed.

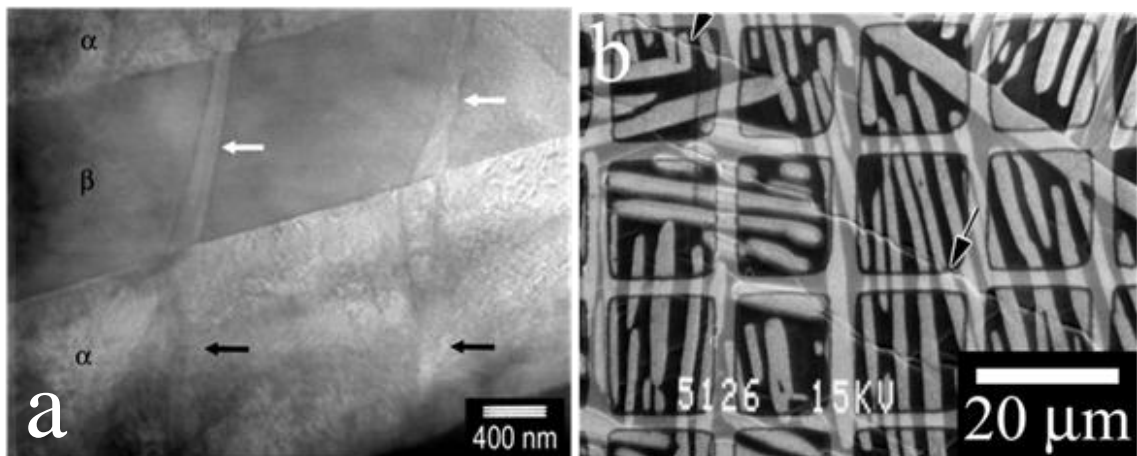


Figure 2.5. (a) TEM micrograph and (b) SEM image showing connection between twinning in α -phase and stress induced martensite in β -phase [21, 22].

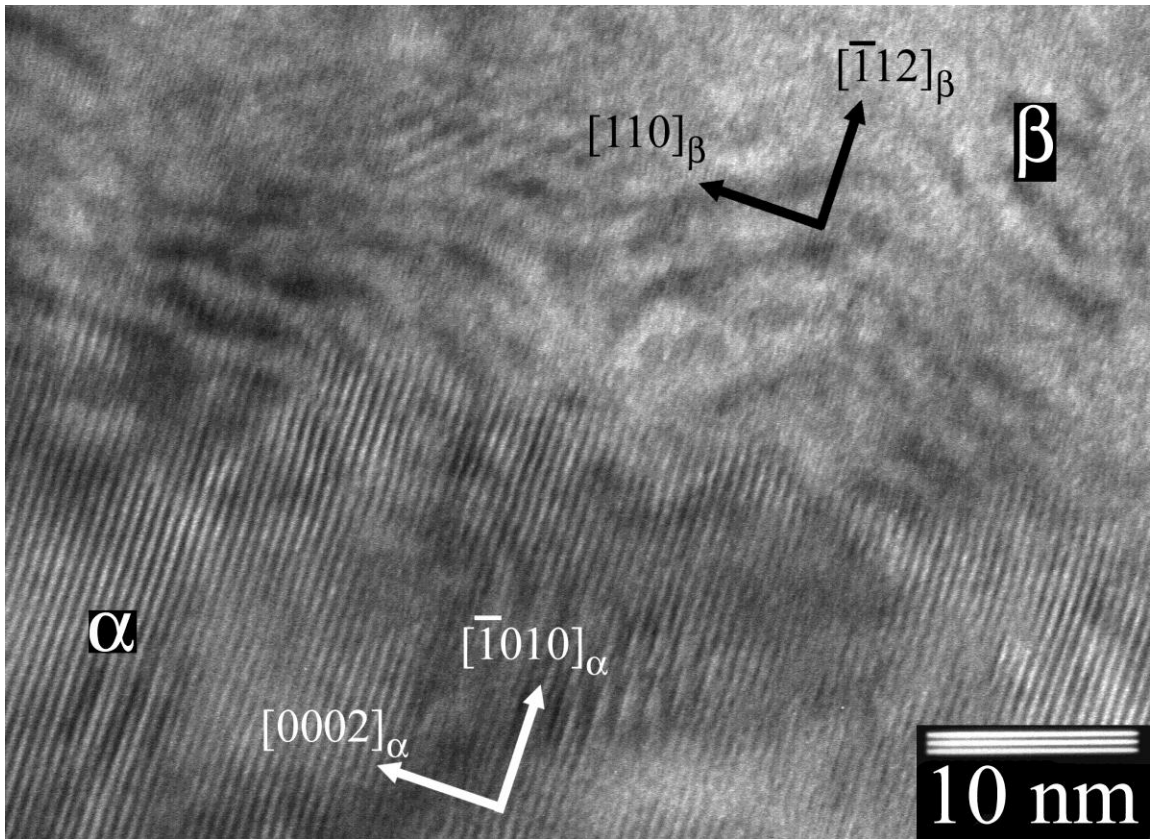


Figure 2.6. High resolution TEM (HREM) micrograph of the slightly rough, semi-coherent α/β interface of Ti-8.1V, viewed from the $[1\bar{2}10]_{\alpha} // [1\bar{1}1]_{\beta}$ direction [21, 22].

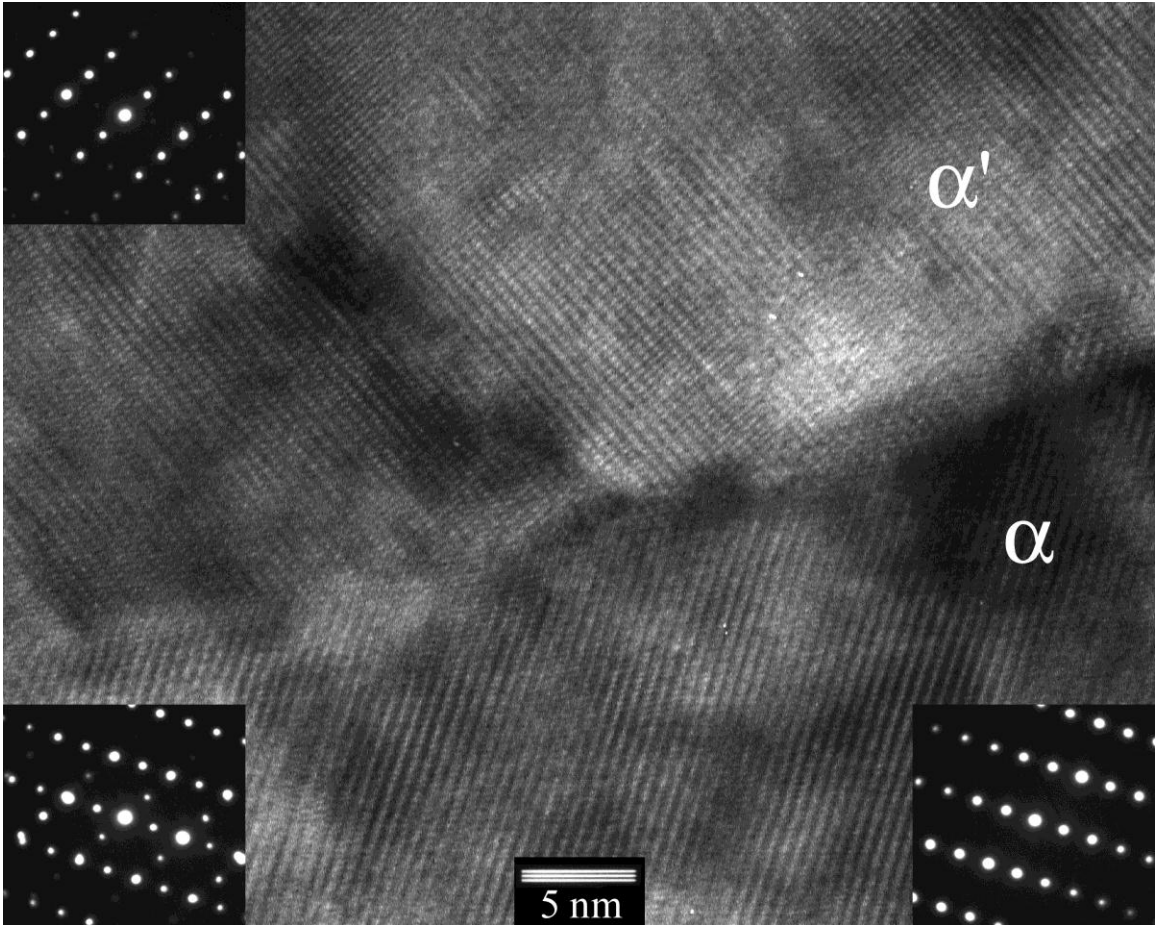


Figure 2.7. High resolution TEM micrograph showing the interface of stress induced martensite (α') and the α phase. Notice the $\{10\bar{1}1\}$ twin relationship between the phases. Selected area diffraction patterns from each phase and the interface taken parallel to the $(1\bar{2}10)$ zone axis are inset. [21, 22]

Chapter 3

Experimental Procedures

The following are general procedures used in the course of this investigation. They are referenced as required in Chapters 4 and 5 for individual investigations. A selection of single and two-phase Ti-V alloys were selected such that the chemistry of the single-phase α and β alloys researched previously [17, 47] would match the component α and β phases of the two-phase alloys. Two different microstructures were also used in this investigation to study the effects of phase morphology and grain size on the creep deformation mechanisms. The extent of low temperature creep strain in titanium alloys has been shown by many researchers to be dependent on grain size [16, 17, 19, 47-52]. Additionally, it has been shown previously that certain microstructures can result in deformation mechanisms not present in the single-phase alloy versions of the respective phases [53]. As such, both of those effects will be addressed here.

3.1. Heat treatment

The Ti-1.6wt% V, Ti-4.3wt% V, Ti-8.1wt%V, and Ti-12.6wt% V alloys used in this investigation were melted as 13.6 kg ingots and processed to 1.74 cm diameter bars at RTI International Metals, Inc. in Niles, Ohio. The final rolling step to a 60% reduction in area was carried out in the $\alpha + \beta$ field at 973 K. To obtain the desired microstructure, the Ti-1.6V alloy was vacuum encapsulated in quartz tubes at 10^{-5} Pa, then annealed at 1173 K for 2 hours, furnace cooled to 963 K and annealed for 200 hours, then water quenched to room temperature. To obtain the fine equiaxed microstructure for the Ti-

4.3V, Ti-8.1V, and Ti-12.6V alloys, the bars were vacuum encapsulated in quartz tubes at 10^{-5} Pa, then heat treated for 200 hours at 963 K (just below the tie line), followed by a water quench. To obtain the coarse equiaxed microstructure for the three intermediate alloys, the bars were vacuum encapsulated and then heat treated for 168 hours just *below* the beta transus temperature and then furnace cooled 10 degrees every 48 hours to 963 K. The samples were then annealed for 200 hours at 963 K, followed by a water quench. To obtain the Widmanstätten microstructure, the alloys were vacuum encapsulated and then heat treated for 2 hours just *above* the beta transus temperature followed by a furnace cool to 963 K. After annealing for 200 hours at 963 K, the bars were then water quenched. The quartz tubes were broken right before quenching to ensure a fast quench. The chemical compositions are actual chemical compositions of the alloys after fabrication as determined by wet etch method and shown in Appendix A.

3.2. Tensile and creep specimen preparation

Tensile and creep specimens were then machined from the bars according to the specifications detailed in Appendix B, with flat surfaces cut onto the gage length sections by electric discharge machining (EDM). The flat gage sections were then mechanically polished using progressively finer grit down to 1200 grit, followed by a final polishing step on a Chemomet[®] polishing cloth with a 0.5 μm Buehler Mastermet[®] silica solution. After polishing, the specimens were etched with a combination of A-etch (2.5 mL HF, 2.5mL HNO₃, 5.0 mL glycerin) and R-etch (16 mL glycerin, 14 mL ethanol, 7.5 g benzalkonium chloride, 10 mL HF) for a few seconds each. The A-etch will reveal grain boundaries while the R-etch dyes the beta phase for imaging in SEM.

3.3. Attachment of fiducial grids

Gold-palladium fiducial lines were deposited on the polished specimen surfaces. The fiducial grid serves several purposes: to allow easy identification of the same area for pre and post testing microscopy, to measure strain in local areas, and to aid in the identification of interphase interface sliding, indicated by displacement of lines across boundaries.

ShIPLEY Microposit 950 A10 PMMA positive electron resist was spun onto the specimen surface at 3300 RPM for 50 seconds on a Headway EC-101 spinner in a UV free clean room (FabLab) and pre-baked at 170°C for 30 minutes. The specimens were transported inside a film bag to guard the resist from light. A JEOL JXA 8900R microprobe was used to expose the resist. The specimen is placed into the microprobe with the lights off to avoid prematurely exposing the resist. The grid line spacing was set to 50 μm . Beam writing conditions were 30kV, 25x magnification, and an aperture size of 4. Test lines were drawn with beam currents ranging from 1 – 100 nA and exposure times ranging from 1 – 10s. This procedure should be performed for any new batch of photoresist. The optimal settings for this investigation were 10 nA and 10s. The resist was then developed for 90s with agitation and light swabbing in Shipley MIBK:IPA 1:3 developer. The specimen surface was etched lightly for 15 seconds by dilute titanium etch (2 mL HF, 4 mL HNO₃, and 194 mL H₂O) to facilitate removal of the resist after sputtering. Gold-palladium was deposited to a thickness of 20 nm (120 seconds) by an Anatech LTD Hummer X sputtering system. To remove the remaining photoresist, the specimen was sonicated in acetone for 10 – 30 minutes.

3.4. Tensile testing

Tensile testing was conducted at room temperature in an Instron 8502 floor model servo-hydraulic materials testing machine with a 500kN load cell. Testing was performed at a strain rate of 3.28×10^{-5} /sec to a total strain of 3% for all two-phase specimens and at 1×10^{-6} , 1×10^{-4} , 1×10^{-2} , and 1×10^{-1} /s to a total strain of 3% for the single-phase α specimens. An Instron clip on extensometer with a 12.7 mm gauge length and 5% maximum extension was used to measure strain.

3.5. Creep testing

Specimens examined for this work were creep tested in an ATS lever arm creep test machine at 95% of the measured yield stress. Interrupt creep tests were performed and the samples were taken off for imaging after 60 s, 10 minutes, 1 hour, and 200 hours. A clip-on extensometer was used for recording the strain and data sampling rates ranged from 10 per second early in the testing to one per hour after 8 hours of testing. SEM micrographs were taken of the same area on the samples before testing as well as at each of the interrupts and after 200 hours of total testing time.

3.6. SEM and optical microscopy

SEM micrographs were taken of the polished specimen surfaces prior to and following tensile and creep deformation. This procedure is useful for separating deformation products that arise during tensile and creep testing from those that may be

present prior to testing. A Hitachi S-3400N (FabLab) and Zeiss ICM 405 inverted metallographic light microscope were used to record images of the alloys.

3.7. TEM sample preparation

The success of transmission electron microscopy (TEM) depends on the careful preparation of specimens, which must (1) remain unadulterated and (2) be sufficiently thin for electron transparency. There are many common preparation methods, some better suited to the two-phase metallic specimens than others for a variety of reasons. Several basic steps are involved for the preparation of specimens from titanium tensile and creep samples. These are outlined below.

3.7.1 Cutting TEM samples from creep or tensile specimens

The first step is removal of a specimen from the bulk material. A Buehler Isomet Low Speed Saw with diamond wafering blade was used to slice sections of material from the bulk, from both the deformed material in the gage length and the undeformed material in the threaded ends of the tensile and creep specimens. Buehler Isocut[®] fluid was used to lubricate and cool the wafering blade while removing debris and a saw speed of 5 was selected. Cutting speeds were kept slow to prevent sample damage due to cutting forces. One slice was made initially to reveal the interior of the sample material of interest, and then subsequent slices were made by moving the sample holder a set distance in relation to the blade. This is accomplished by dialing in the attached micrometer the desired displacement. 18 divisions of the micrometer yielded specimens of approximately 120 μm thick. A Gatan model 659 disc punch was then used to produce 3 mm discs from the

cut slices. The Gatan punch is designed such that no additional deformation is introduced into the specimen.

3.7.2 Pre-thinning

Pre-thinning was performed with jet-polishing. Jet polishing is a chemical process that uses a combination of an acid containing electrolyte and electric current to remove material from the sample. A South Bay Technology Inc. Model 550 jet thinning electropolisher was used for this investigation. An electrolyte solution of 94% methanol, 3% sulfuric acid and 3% hydrochloric acid cooled to 210 K (-60°C) in a dry-ice/methanol bath was used. The samples were polished using a pump speed of 4, sensor sensitivity of 5, and a current of 25 mA. It will be necessary to adjust the voltage between 75 – 100 V to maintain a constant current. The polishing should take about 2 minutes per side and leave a very shiny surface. If the surface is not shiny, the voltage will need to be adjusted. The Ti alloys used in this investigation will build up a surface oxide layer at the contact point with the polisher after an extended amount of time. Therefore it is important to only flip the sample once during polishing to maintain a clean contact. Jet-polishing is relatively rapid, but etches the α phase of the two-phase titanium alloys more rapidly than the β phase. The result is a thickness difference at the α/β interface that makes any study of the interface, difficult. To solve for this, an additional ion-milling thinning step was performed.

3.7.3 Final thinning

Final thinning was performed with ion milling. The ion milling machine used is a Fischione Instruments Model 1010 Ion Mill. Milling was performed at a 10° incidence to the sample, with power settings of 5.0 V and 3.0 mA to perforation. The laser sensitivity was set to 2. The specimen stage was cooled with liquid nitrogen and maintained at ≤ -30 °C. Depending on the thickness and unevenness of the sample, the initial milling step may take up to 1 hour. Once a hole is formed in the sample, the power was reduced to 3V and 3.0 mA for an additional milling time of 30 minutes and then to 1 V and 3.0 mA for 10 minutes in order to remove amorphous material from the sample edge and leave a very thin sample area. The complete instructions for operating the ion mill are included in Appendix C.

3.8. Transmission electron microscopy – TEM

TEM was used for the majority of characterization and analysis in this study. A JEOL 2100F field emission TEM (NispLab) as well as a JEOL 2100 LaB6 TEM (NispLab) both operating at 200 keV were used. A combination of many techniques was required to understand the microstructure and deformation mechanisms, including selected area diffraction (SAD), bright field imaging, and dark field imaging. A complete description of these techniques is beyond the scope of this chapter, but an excellent resource for various TEM techniques is “*Practical Electron Microscopy in Materials Science*” by J.W. Edington [54]. Several important points must be kept in mind for the safety and operation of the instruments which are outlined in Appendix D. In order to determine some deformation mechanisms, the diffraction pattern must be oriented

correctly with respect to the image. This rotation depends on the magnification of the image. This calibration is provided in Appendix E.

The various deformation mechanisms were identified in several ways. Slip was identified by dark field imaging using three different g vectors, and $g \bullet b$ analysis. To determine if slip involving screw dislocations with a Burgers vector $\bar{b} = \frac{1}{3}\langle 11\bar{2}0 \rangle$ were gliding on basal or prism planes, bright and dark field images were taken along both $\langle 11\bar{2}0 \rangle$ and $[0001]$ zone axes and tilted slightly to determine if the dislocation lines visible were single dislocations or stacks of dislocations on single planes in projection. This was necessary because a -type screw dislocations in hexagonal crystals can glide on basal or prism slip planes.

To identify twins in the α phase, selected area diffraction patterns (SADPs) were taken from the matrix, the twin/matrix interface, and where possible the twin. In general to identify the type of twin the specimen must be tilted along a zone axis that contains the g vector for the twin plane common to both the twin and the matrix. For the $\{10\bar{1}2\}\langle \bar{1}011 \rangle$ twins observed in this investigation it was required to tilt along a $\langle 11\bar{2}0 \rangle_\alpha$ zone axis. In the case of $\{10\bar{1}2\}$ twins there is a rotation of $\sim 94^\circ$ between the $[0001]$ planes of the twin and matrix. The exact rotation depends of the c/a ratio of the α phase. The spots in the interface diffraction pattern will be mirrored across the g vector of the twin plane. Since there are three independent $\langle 11\bar{2}0 \rangle_\alpha$ directions, and the twin plane contains only one of these directions, for each twin there is only a 1/3 chance that the correct zone axis for identification will be attainable, as tilting 60° to the next $\langle 11\bar{2}0 \rangle_\alpha$

axis is impossible due to limits of the TEM specimen holder. In even more cases the alignment of the α grain where the twin is visible is oriented close to the $[0001]_{\alpha}$ zone axis, where a tilt of $\sim 90^\circ$ would be required. Therefore identification of any given twin is extremely difficult, and some twins could not be identified due to the tilt limits of the specimen holder. Persistence and patience must be used during this process.

As discussed briefly in the introduction, there have been several type of stress induced martensite reported in titanium alloys. To identify which type of martensite was present, the martensite selected area diffraction patterns were indexed and measured. The crystal structure was identified as hexagonal, and the Burgers orientation relationship $[0001]_{\alpha'} // \{110\}_{\beta}$, which exists between the martensite and the β phase, was obeyed. This was evidence for stress induced hexagonal martensite as opposed to the orthorhombic martensite. The stress induced hexagonal martensite can form in six orientations in any given β grain with the $[0001]_{\alpha'} // \{110\}_{\beta}$ relationship, so the martensite may not be oriented along an equivalent β zone axis to the one aligned with the beam, so identification of an individual martensite plate is difficult.

It should be noted at this time that undeformed material was examined to insure that the deformation mechanisms in the deformed material were the result of testing and not TEM specimen preparation. Also, the frequency of twins and martensite is quite low, therefore slow and careful surveying of each TEM specimen was necessary to find areas with twins and martensite for analysis. The objective lens aperture must be used in order to distinguish these plates from the matrix, and even then the contrast can be faint.

3.9. Manual calculation of resolved shear stresses

In order to understand the effect of interactions between α and β phase deformation mechanisms, the magnitude of resolved shear stress that the observed α phase deformation mechanisms place on the shear systems for twinning and the $\beta \rightarrow \alpha'$ (hexagonal martensite) transformations were calculated for all possible combinations of observed deformation mechanisms. Due to the Burgers orientation relationship between the α and β phases and the α' and β phases, the orientation of the various directions and planes are fixed in relation to one another within the alloy system.

The 4-index 120° coordinate systems for the hexagonal α and α' phases were first transformed to a 90° 3-coordinate Cartesian system. Transformation matrices were calculated to transform directions and planes in the α phase into parallel directions in the β phase, as shown in Appendix F. Directions and planes important for calculating resolved shear stresses, such as slip planes, Burgers vectors, twinning planes and directions, and planes and directions important for the $\beta \rightarrow \alpha'$ transformation were then converted to equivalent directions in the β phase. The result is a common Cartesian coordinate system to perform calculations of resolved shear stresses between the α , β , and α' phases.

Within this coordinate system the magnitude of resolved shear stress from deformation products in the α phase were calculated. The maximum shear stresses for the basal slip systems, prism slip systems, and twinning shear systems were resolved onto the maximum possible shear systems for twinning and $\beta \rightarrow \alpha'$ stress induced transformation. The magnitude of these resolved shear stresses was calculated for every combination of

the above deformation products in a Microsoft Excel spreadsheet using the equations for vector transformation given below [55]:

$$\begin{aligned} \sigma'_{x'y'} = & \alpha_1\alpha_2\sigma_{xx} + \beta_1\beta_2\sigma_{yy} + \gamma_1\gamma_2\sigma_{zz} + (\alpha_1\beta_2 + \alpha_2\beta_1)\sigma_{xy} + \\ & (\beta_1\gamma_2 + \beta_2\gamma_1)\sigma_{yz} + (\alpha_1\gamma_2 + \alpha_2\gamma_1)\sigma_{xz} \end{aligned} \quad (3.1)$$

where:

$$\begin{aligned} \alpha_1 &= i' \cdot i & \alpha_2 &= j' \cdot i \\ \beta_1 &= i' \cdot j & \beta_2 &= j' \cdot j \\ \gamma_1 &= i' \cdot k & \gamma_2 &= j' \cdot k \end{aligned}$$

and $[ijk]$ is the original vector and $[i'j'k']$ is the vector on which the stress is resolved.

The complete results of these calculations are presented in Appendix G.

Chapter 4

Deformation Mechanisms and Kinetics of Time-Dependent Twinning in an α -Ti-1.6V alloy

With some exceptions [50, 56-60], few researchers have studied the strain-rate sensitivity of α -titanium alloys at *ambient* temperatures. In the present study, the strain-rate response of polycrystalline α -titanium is examined, with particular focus on the deformation mechanisms which control that response.

The unique challenge associated with studying deformation mechanisms in HCP metals, such as α -titanium, stems from the occurrence of both slip and twinning during plastic deformation. The three most common slip modes are the $\{10\bar{1}0\}$, $\{10\bar{1}1\}$, and $\{0001\}$ planes, with $\langle 11\bar{2}0 \rangle$ as the slip direction. These three glide planes with the slip direction in the basal plane make up four independent slip systems [61]. However, five independent slip systems are necessary for the polycrystalline material to be able to homogeneously plastically deform. It's also the case that none of the slip systems identified can support deformation in the c -direction. Therefore, twin systems or $\langle c+a \rangle$ pyramidal slip are necessary to maintain deformation compatibility and the two deformation mechanisms will occur together [56, 62, 63].

Commonly occurring in: metals [42, 50, 64-68], ceramics [69], intermetallics [70, 71], nanocrystalline materials [72], superconductors [73, 74], and geological systems [75], twinning is an important deformation mechanism. The rate of twin growth has traditionally been observed to be approaching the speed of sound in the material (i.e. 5,090 m/s in α -titanium) [42, 76]. Recent observations have shown however that twin

growth rates can be many orders of magnitude smaller than the speed of sound, on the order of 1 nm/s, in single-phase α (hexagonal close-packed) and β (body centered cubic) titanium alloys [16, 23-25]. A crystallographic model was recently developed which attributes the slow twin growth rates to the diffusion of oxygen from interstitial sites near the twin boundary [23, 24, 45]. When twinning occurs, these interstitial sites are not always conserved and the oxygen atoms must diffuse away from those sites before twinning can take place. According to previous twinning models, there should be no time dependence in twin growth rates; hence strain rate should not affect twin growth rate, for a constant applied stress. However; recent work showing a significant effect of strain rate on twinning, supports the theory that twinning in these materials can be controlled by a process which is much slower than the speed of sound, such as the diffusion of oxygen.

This study presents a comprehensive look at the deformation mechanisms, twinning behavior, and resultant mechanical properties of these alloys and uses these results to explain how traditional views on deformation twinning do not explain the slow twin growth observed in single-phase α -titanium alloys. The broader purpose of this investigation is to develop a constitutive equation which describes the strain rate sensitivity of twinning as a function of oxygen diffusion. Further, both optical and electron microscopy are used to identify and characterize the deformation products present at the differing strain-rates.

Under the conditions of a tensile loading test, the applied stress is continually increased such that the strain rate remains constant. However, creep occurs at a constant stress that is oftentimes below the yield stress of the material. Since a finite amount of stress is available to supply the activation energy required for creep deformation

mechanisms, additional stresses that can contribute to creep deformation are only available from internal sources. These internal stresses (most often caused by interphase interactions) are the focus of this work. To design alloys and processes for improved creep resistance, these interactions must be understood. It should be noted that the results of this investigation can also be applicable to any other hexagonal-close-packed (HCP) system, including Zirconium alloys.

Mechanical twinning was best incorporated into the experimental studies and constitutive models of Zerilli and Armstrong [77] and Kalidindi [78]. Tomé et al. [79] developed a constitutive equation for the combined slip/twinning deformation in HCP metals. Meyers et al. [50] were then able to introduce a constitutive description which could describe the onset of twinning as a function of a critical twinning stress. This critical twinning stress can be described in terms of strain-rate, grain-size, texture, and stacking-fault energy [50]. It should be noted however, that all of these studies assume unstable twin *growth* after twin nucleation. The objective of this research effort is to use these constitutive descriptions [50, 77, 79] as a basis to obtain a linkage between the twinning nucleation/growth patterns and the strain rate.

4.1. Crystallography of time-dependent twinning

Fortunately, the crystallography and quantitative analysis of deformation twinning in HCP metals has been extensively studied [80-85] and the lattice relationships between the matrix and the twin on the most common twin planes are known [43, 44]. The twinning crystallography in HCP metals is complex because atomic shuffles as well as twinning shear are an important factor in producing a twinned structure. With regard to

α -titanium, there are four predominant twinning modes, of which the $\{10\bar{1}2\}$ and $\{11\bar{2}1\}$ twin planes involve the smallest shear and simplest shuffles respectively. Of these two, the $\{10\bar{1}2\}$ system is the most common because the Burgers vector for $\langle a \rangle$ type slip along the $\langle 11\bar{2}0 \rangle$ direction doesn't have a c-axis component and twinning is necessary to accommodate strain along $[0001]$. The conventional twinning models in HCP materials presented by Song and Gray [43, 44] demonstrate atoms moving to a twinned position by a simple shear process without shuffles of the interstitial sites. Other models by Crocker [86, 87] demonstrate atoms moving by both shear and shuffle mechanisms in $\{1\bar{1}02\}$ twinning; however, neither of these models consider the conservation of the octahedral interstitial sites if atoms such as oxygen reside there. Oberson & Ankem [45, 88] were the first to develop a $\{1\bar{1}02\}$ crystallographic twinning model based on the models of Song and Gray [43, 44] showing the octahedral interstitial sites which are not conserved and must be reformed for the twin front to advance. These theories are supported by studies done by Cerreta et al. who have shown interstitial oxygen to have a significant effect on deformation mechanisms of α -titanium and zirconium [89, 90]. In particular, it was shown that interstitial oxygen can inhibit twinning and form a resistance to lattice shear [89, 90]. In addition, Khan et al. also demonstrated interstitial oxygen inhibiting direct shear deformation mechanisms [91] which can be attributed to the elimination of octahedral interstitial sites. Figure 4.1 is an extension of Figure 2.3 and shows the crystallographic model of the untwinned and twinned HCP lattice which accounts for these sites and explains the observed behavior.

According to the model developed by Oberson et al. [45], the growth rate of twins in α -titanium at room temperature should be controlled by diffusion of oxygen away from

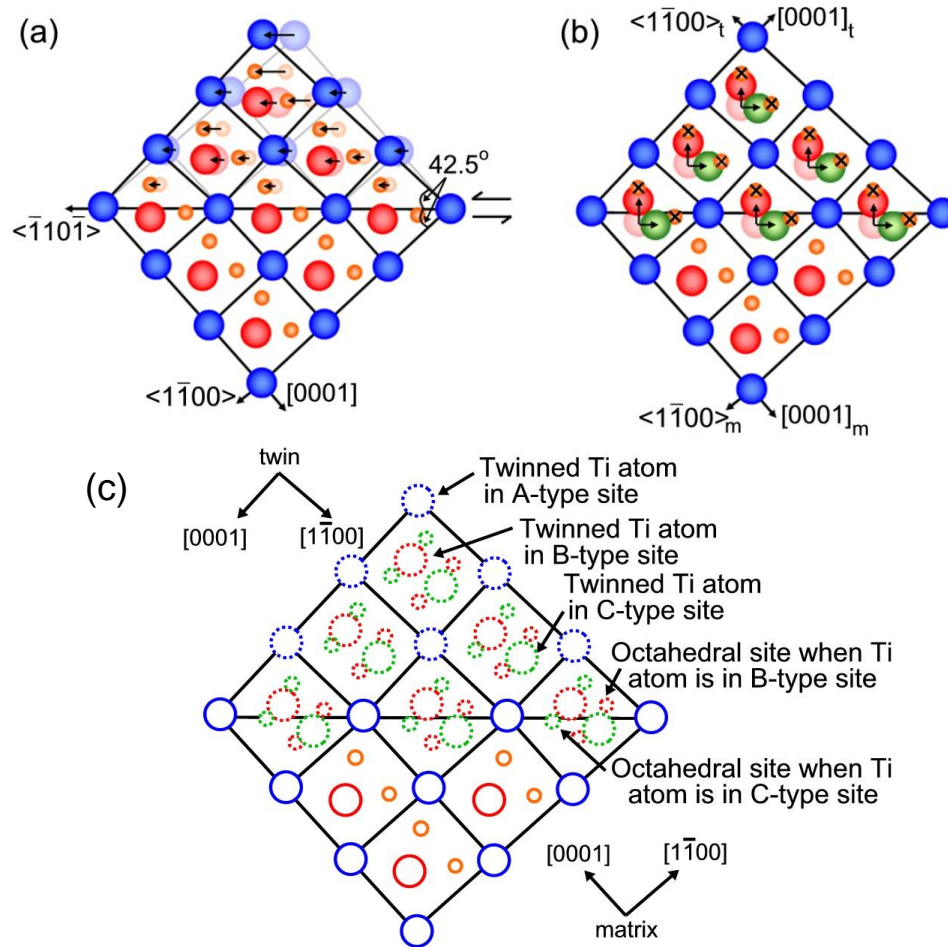


Figure 4.1. Schematic illustration of $\{10\bar{1}2\}$ twinning in the HCP lattice of α -titanium. Projection of the lattice is onto the $\{11\bar{2}0\}$ plane. (a) Shear of the lattice in the $\langle 1\bar{1}0\bar{1} \rangle$ direction moves only **A**-type Ti atoms (large, dark circles) directly to twinned positions. (b) Arrows give the shuffles required to move the Ti atoms in **B**-type sites (large, lighter circles) to their twinned **B**-type or **C**-type positions. Reorientation of the lattice eliminates the octahedral sites (small circles with “x” mark) where oxygen could reside. (c) Schematic illustration of a completed $\{10\bar{1}2\}$ twinning event. The completed positions for **B**-type Ti atoms and the corresponding possible octahedral sites and the completed positions for **C**-type Ti atoms and the corresponding possible octahedral sites are indicated by the arrows. These models are an extension of earlier twinning models by Song and Gray (Song and Gray, 1995b,c), but now include the corresponding movements of octahedral sites where oxygen may reside [45].

eliminated octahedral interstitial sites. Classical observations of twinning suggest that the growth of twins is controlled by a shear process which would mean that for a given amount of strain, twin thickness at various strain-rates should be approximately equal.

4.2. Time dependent twinning during creep of α -Ti-1.6V

Time dependent twin growth has been previously observed during creep of single-phase α -titanium alloys [24, 92]. A model was presented to explain the slow twin growth as a function of the diffusion of oxygen atoms away from octahedral interstitial sites in the matrix. Two important features were identified: (1) the activation energy for creep was very close to the activation energy for oxygen diffusion in this alloy, and (2) twinning is the primary plastic deformation mode as opposed to slip in creep deformation of α -Ti-1.6V [24].

The activation energy for tensile deformation of α -titanium at temperatures less than $0.4 \cdot T_m$ was first measured by Conrad [93]. It was suggested at the time that the rate-controlling process is the thermally activated overcoming of interstitial solute atoms by dislocations gliding on first order prism planes. There have been a number of subsequent studies considering factors such as microstructure and strain rate [57, 94-97], but all have assumed unstable twin growth after nucleation.

4.3. Model for diffusion of oxygen at twin front

According to the crystallographic model for α -titanium developed by Oberson et al. [45], the growth rate of twins is limited by the diffusion of oxygen away from eliminated octahedral interstitial sites. The advancing twin front accompanied by

diffusion of oxygen atoms can be related to the diffusion of an interstitial species into the bulk of a sample, such as carbon into a bulk sample of iron. In such a case, the effective penetration distance is the point at which the concentration of the diffusion species has a value equal to the average of the initial concentration in the bulk and the surface concentration [98]. For the twin growth model, growth is assumed to be one-dimensional, in a direction normal to the center plane of the twin. The center plane of the twin corresponds to the surface of the material and the thickness of the twin (from the center plane to the widest point) corresponds to x_{eff} . This effective penetration distance, x_{eff} is defined as Eq. (4.1) [23, 98]:

$$x_{eff} = \sqrt{Dt} \quad (4.1)$$

where D is the diffusivity and t is time. Further, interstitial diffusion in alloys is governed by Eq. (4.2):

$$D = D_0 * \exp\left(\frac{-Q}{RT}\right) \quad (4.2)$$

where D is the diffusivity of a species, D_0 is the pre-exponential diffusion constant, Q is the activation energy for diffusion, T is the temperature, and R is the ideal gas constant in units of J mol K^{-1} . As modeled by Oberson et al., oxygen can either diffuse deeper into the parent grain or it can diffuse into the twin side of the interface; therefore it is not believed that there will be a significant pile-up of interstitial oxygen atoms at the interface so the values for D_0 and Q should not change during the duration of the test [45].

4.4. Model for stress-assisted interstitial diffusion in α -Ti

Elastic fields, which can be generated by defects such as twins, influence the diffusion process. The study of stress effects on diffusion have been characterized experimentally for decades [99-102]; however, understanding the effects of stress and strain on diffusion in alloys is fairly limited. Eq. (4.2) has been modified to describe various field influences on diffusion; however, this expression does not take into account the difference between the effect of electric fields or thermal energy which affect an individual atom and an elastic field which influences the neighbors of an atom. It is clear that any modification to Eq. (4.2) to account for a stress must consider the position of neighboring atoms and crystallographic structure [103-105]. The clearest theoretical derivation for tracking the effects of stress or strain states on diffusion has been done by M.J. Aziz et al. [106-109]. Aziz theorized that the effect of stress could be characterized by a *migration strain modification factor* which describes the dimension changes of the crystal parallel and perpendicular to the direction of net transport [109]. As such, the stress-induced change in the diffusivity could be described by Eq. (4.3).

$$\frac{D_{\sigma}}{D_0} = \exp\left(\frac{\sigma V'}{k_B T}\right) \quad (4.3)$$

In Eq. (4.3), D_{σ} is the diffusivity under stress, D_0 is the diffusivity under zero stress, σ is the applied stress, k_B is the Boltzmann Constant, T is the temperature in degree Kelvin, and V' is a material specific atomic migration volume which we can assume to be a constant factor for oxygen diffusion in α -titanium [109]. This factor, V' , contains the information about the dimension changes for the crystal both parallel and perpendicular to the direction of net transport when the point defect reaches its saddle point. As the diffusivity of an interstitial atom is proportional to the product of the concentration and

the mobility of the defect, the effect of stress on diffusivity in a specific direction can be described using this factor [109].

4.4.1. Effect of stress on activation energy of interstitial diffusion

When studying the effect of stress on interstitial diffusion, a component besides the change in volume of the crystal must also be considered. An atom's ability to diffuse is not only controlled by the activation energy required to move from one saddle point to another (a function of volume of the unit cell) but also the energy that the atom possesses to begin with. This energy can be increased (making the jump to the required activation energy easier) through electrical and thermal means. With an increase in strain rate, there is also an increase in work done to the sample. This increase in work is converted within the sample to heat and this increase in heat can change the activation energy required for diffusion. Since both Equations 4.2 and 4.3 have a Temperature term, this increase in sample temperature could have a significant impact on values obtained. The increase in sample temperature is found according to the equation $\Delta T = \frac{\beta}{\rho C} \int \sigma d\varepsilon$ [95], in which $\beta = 0.9$ (assuming 90% of work of deformation was converted to heat), ρ is the density of the sample ($\sim 4.506 \text{ g cm}^{-3}$) and C is the heat capacity of the sample ($\sim 25.060 \text{ J mol}^{-1} \text{ K}^{-1}$). It was found during the course of this investigation however, that even the highest strain rate experiment only gave rise to a 5° increase in the sample temperature which would make this change in activation energy for diffusion insignificant and can thus be neglected.

4.5. Tensile testing results

The true stress versus true strain curves are shown in Figure 4.2. The small slope of the curves in the plastic range indicates a low strain-hardening rate which is common for most titanium alloys [110-112]. The strain-rate sensitivity of titanium alloys decreases with increasing strain. A summary of the tensile properties obtained at different strain rates is given in Table 4.1. Three tensile tests were performed for each experiment but only one was polished and etched for microscopy. The results of the tensile test were within +/- 2% (< 7 MPa). It can be seen that the flow stress of the titanium alloy increases with increasing strain rate. The increase in flow stress will have an effect on the twinning behavior of this alloy as discussed in *Section 4.8.2*.

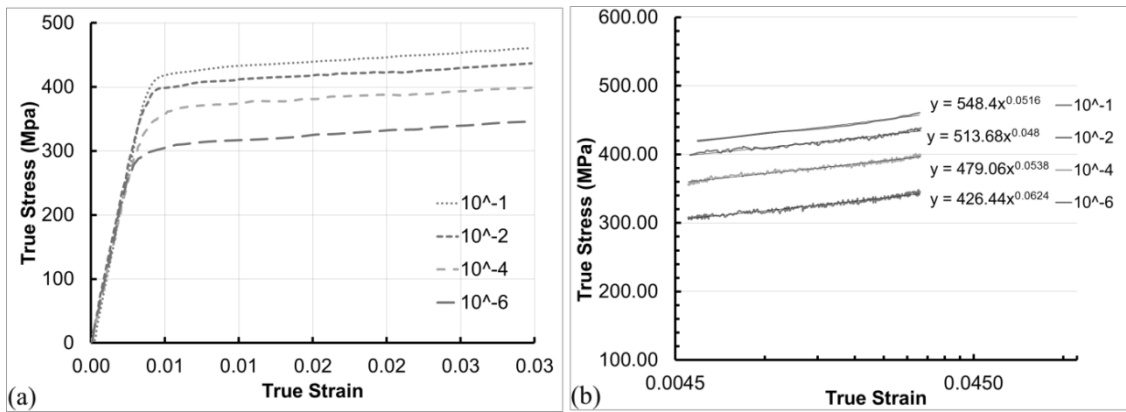


Figure 4.2. Mechanical testing results of α -Ti-1.6V tested at different strain rates. (a) True stress – true strain curves of alloy tested at different strain rates. (b) Strain hardening rate of the plastic region of each of the curves. The alloy exhibits a low strain hardening rate for all tested strain rates.

Table 4.1. Mechanical testing results of α -Ti-1.6V tested at different strain rates at 298K.

Strain Rate	10^{-1} /s	10^{-2} /s	10^{-4} /s	10^{-6} /s
0.2% Yield Stress (MPa)	420	399	357	305
Flow Stress @ 3% Strain (MPa)	460	437	399	346
Elongation (%)	3	3	3	3

4.6. Optical and SEM microscopy

Tensile specimens were examined before and after testing by optical and SEM microscopy to look for evidence of deformation mechanisms such as slip and twinning. The fiducial grid serves as a reference to identify the same area of the specimen before and after testing. The micrographs shown in Figure 4.3 are of the α -Ti-1.6V before and after tensile testing at (a) 10^{-1} /s, (b) 10^{-2} /s, (c) 10^{-4} /s, and (d) 10^{-6} /s respectively, showing deformation mechanisms, specifically deformation twinning as the dominant deformation mechanism across all strain rates. To ensure that the deformation features seen under optical microscopy were twins and not another type of deformation feature or sub-divided grain, polarized light was used and the polarization was changed to see if the features changed. The results for the sample tested at 10^{-6} /s are shown in Figure 4.4, but this technique was performed with the other strain rates as well. As is evident, the deformation features will disappear under certain polarization and are indeed twins. Twinning behavior was characterized using optical microscopy. An area of $\sim 10 \text{ mm}^2$ on each sample was mapped and microstructural features were recorded manually. The results of the deformation maps are organized into Table 4.2.

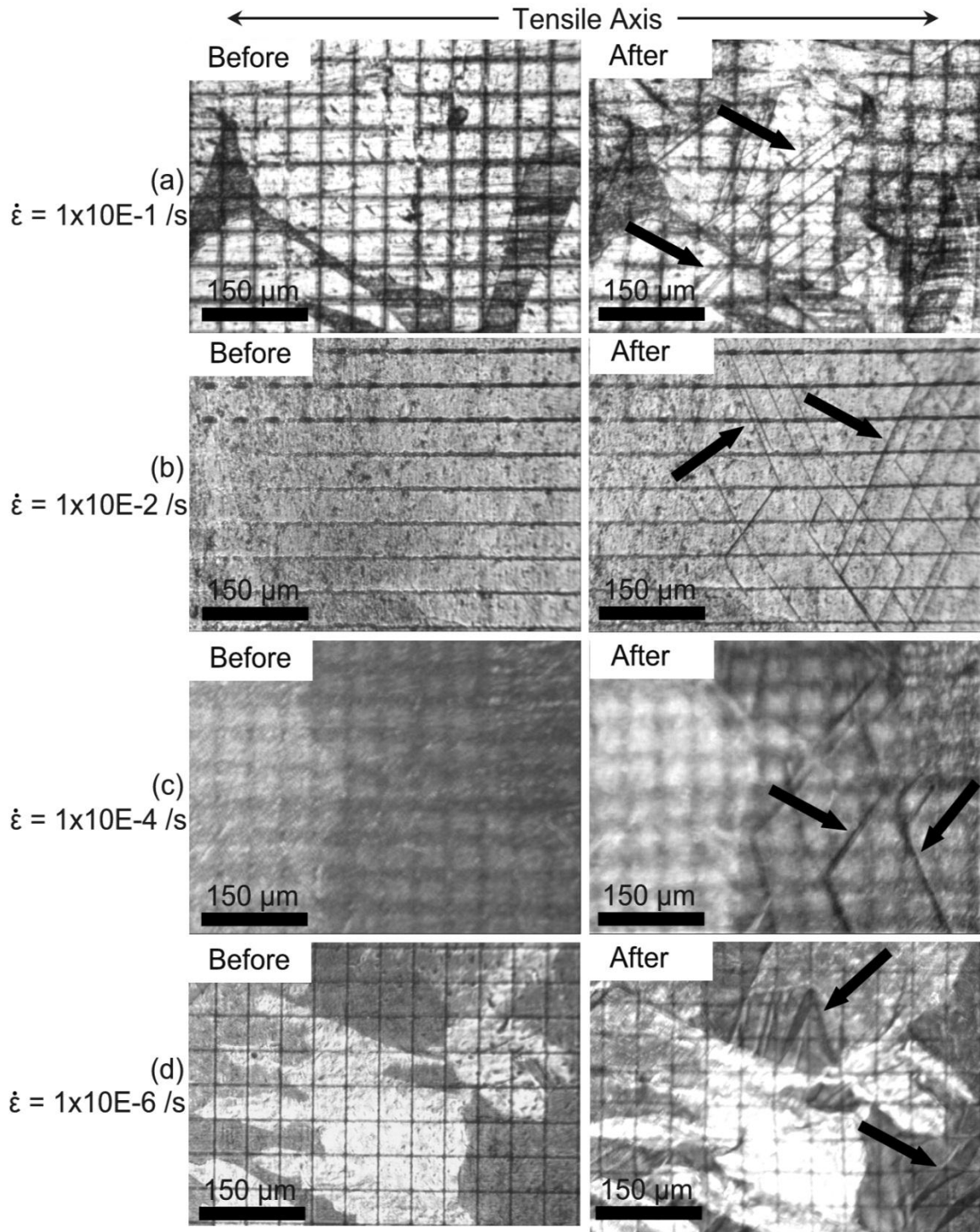


Figure 4.3. Before and after optical micrographs of deformation twinning in α -Ti-1.6V at (a) $10^{-1} /s$, (b) $10^{-2} /s$, (c) $10^{-4} /s$, and (d) $10^{-6} /s$. All samples were tested to 3% strain. All micrographs were taken at 100x magnification. The fiducial grids are $50 \mu\text{m}$ square. Note the gradual increase in twin thickness as the strain rate decreases, as indicated by the arrows.

Table 4.2. Quantitative analysis of deformation twinning in selected area in α -Ti-1.6V tensile tested to 3% strain at 298K. The values for twin volume fraction are accurate to +/- 3%.

Strain Rate	10^{-1} /s	10^{-2} /s	10^{-4} /s	10^{-6} /s
Number of grains in selected area, N_g	125	115	121	123
Number of twinned grains in selected area, N_{tg}	51	41	44	44
Percent of grains twinned, G_t	41%	36%	36%	36%
Number of twins in selected area, N_{tw}	~625	~210	~150	~135
Volume fraction of twins in twinned grains, V_{tg}	7%	7%	9%	22%
Total twin volume fraction, V_t	2.9%	2.5%	3.2%	8%
Approximate average twin thickness, W	0.5 μ m	3.5 μ m	12.5 μ m	20.0 μ m

4.7. TEM microscopy

TEM foils were prepared from specimens tested at each of the strain rates to identify and characterize the deformation products present. There are four main twinning modes which have been identified in HCP materials. In the case of tensile deformed titanium, the $\{1\bar{1}02\}\langle 10\bar{1}\bar{1}\rangle$ twin; hereafter called the $\{1\bar{1}02\}$ twin, is the most common. Figure 4.5 shows a $\{1\bar{1}02\}$ deformation twin and the associated selected area diffraction patterns (SADPs) occurring in the 10^{-1} /s sample. The SADPs were taken from the untwinned matrix (a), inside the $\{1\bar{1}02\}$ twin (b), and across the twin-matrix interface (c).

In addition to identifying the type of twins present during tensile deformation of this alloy, the aim of the TEM investigation was to determine if the twins seen during optical investigations were single twins or close-knit groups of very fine ($<0.1 \mu\text{m}$) twins. As can be seen from the TEM micrographs in Figures 4.5 and 4.6, as well as the high-res optical micrograph in Figure 4.7, the twins present in this investigation are of an appreciably higher thickness than $0.1 \mu\text{m}$ and therefore the calculated twinning thickness averages should not be distorted by an excessive number of unresolvable fine twins.

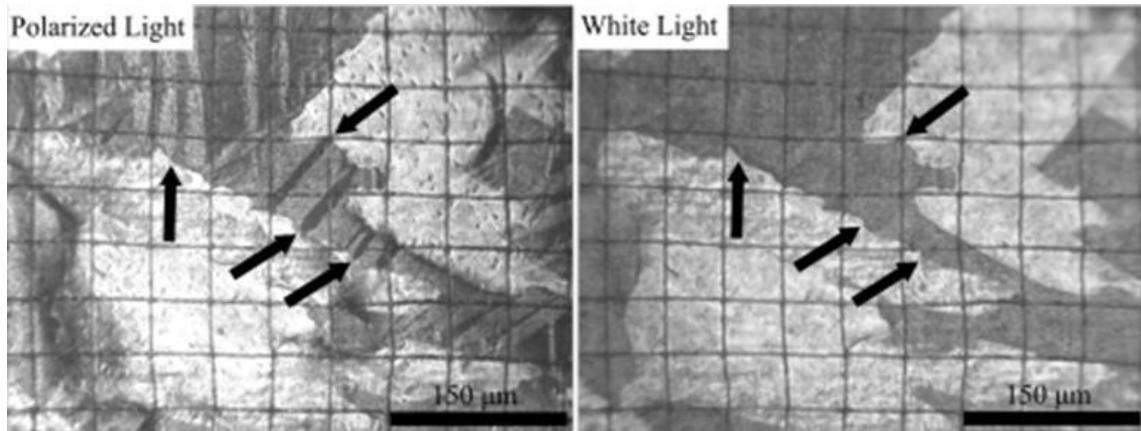


Figure 4.4. Optical micrograph taken under different polarizing light conditions of α -Ti-1.6V, showing multiple twins. $T = 298\text{K}$, $\epsilon = 3.0\%$, strain rate = 10^{-6} /s. The fiducial grids are $50\ \mu\text{m}$ square. Note twins at the arrows which disappear under non-polarized light. This method of twin identification was used for the other strain rates as well but is not shown here.

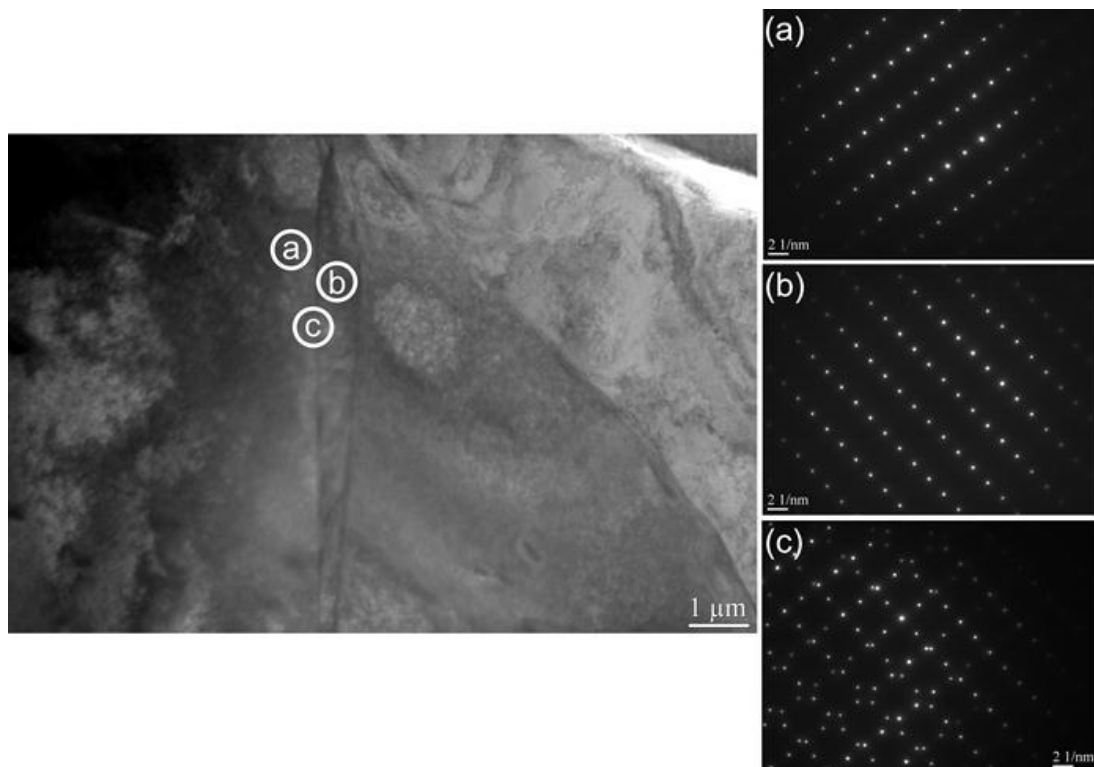


Figure 4.5. Bright field TEM micrograph from tensile deformed α -Ti-1.6V, of $\{1\bar{1}02\}$ twin and SADPs of the $\{2\bar{1}10\}$ foil plane from: (a) the untwinned matrix, (b) inside the twin, and (c) across the twin-matrix interface. $T = 298\text{K}$, $\epsilon = 3.0\%$, strain rate = 10^{-1} /s.

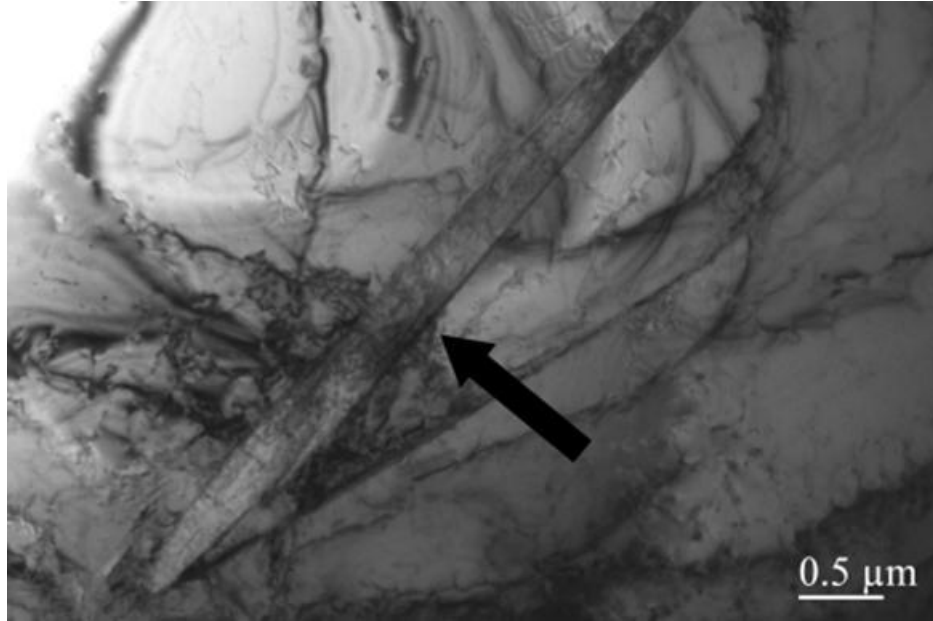


Figure 4.6. Bright field TEM micrograph from tensile deformed α -Ti-1.6V, of $\{1\bar{1}02\}$ twin with $[2\bar{1}\bar{1}0]$ zone axis. $T = 298\text{K}$, $\epsilon = 3.0\%$, strain rate = 10^{-1} /s. Note the twin indicated by the arrow.

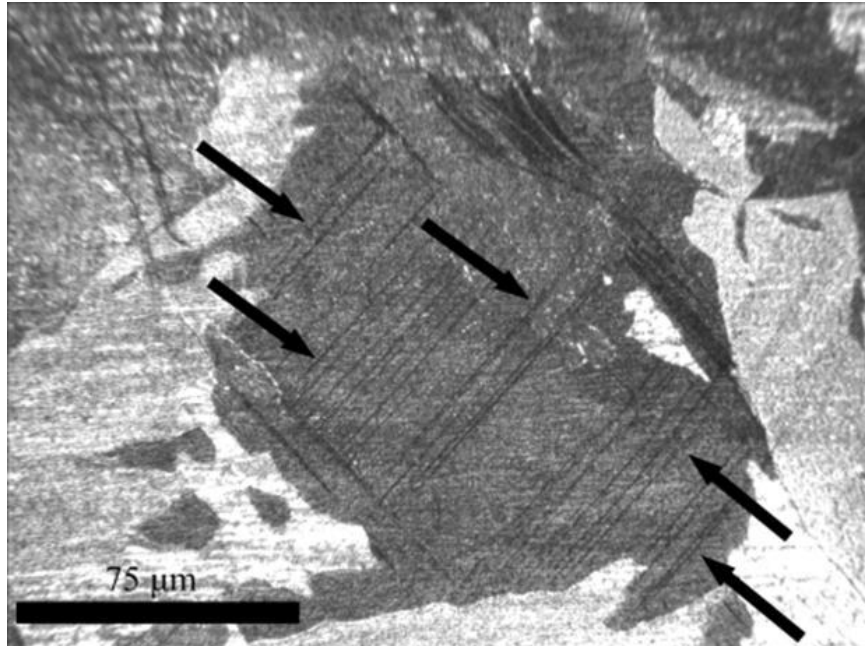


Figure 4.7. Optical micrograph from tensile deformed α -Ti-1.6V. $T = 298\text{K}$, $\epsilon = 3.0\%$, strain rate = 10^{-1} /s. Note the very fine twins indicated by arrows.

4.8. Effect of strain-rate on twinning in α -Ti-1.6V

The critical event in twinning has traditionally been viewed as nucleation. Based on previous research, there seems to be a critical stress for twin nucleation which is temperature insensitive. This issue has been debated in the literature [113, 114], but for the purpose of the subsequent calculations, it will be assumed that the twinning stress has no temperature dependence. Because growth can occur at stresses that are a fraction of the nucleating stress, it has often been assumed that twins can grow at speeds approaching the speed of sound in the material ($\sim 5,090$ m/s in α -Ti). Given that the flow stress in α -titanium is higher at a given strain at higher strain rates, if at all, the thickness of twins at higher strain rates should be larger than at low strain rates. However, twin thickness was found to be much higher at *lower* strain rates, contrary to twin growth based on the classical understanding of twinning. This suggests that there may be another controlling mechanism which is a much slower process, such as the diffusion of solute atoms, for the growth of twins as proposed earlier by the authors and their coworkers [15, 16, 23, 45].

4.8.1. Twin thickness predictions and observations

During a previous investigation, it was found that during creep, the activation energy for twinning is ~ 66 kJ mol⁻¹, which is in agreement with experimentally calculated activation energies for the diffusion of oxygen in α -titanium (65 – 200 kJ/mol) [46]. For this creep test, the activation energy for creep (47 kJ/mol) was lower than for the activation energy for twinning [24]. This was attributed to twinning not being the sole rate-limiting mechanism as slip was still an active deformation mechanism and

twinning can reorient a lattice such that new slip systems can become active. For the experiments conducted during this investigation however, it has been shown that twinning will be the rate-controlling mechanism [15, 50]. This is important because assumptions are made regarding the activation energy for deformation being equal to the activation energy for twinning. To determine the effect of stress on diffusivity, some postulations were made to determine the parameters of Eq. (4.3) using information obtained by Oberson and Ankem [24] .

The α -Ti-1.6V alloy used in this investigation has an oxygen concentration of about 0.07 wt.% (0.21 at.%). At such a concentration value, the experimentally measured activation energy for the diffusion of oxygen in α -titanium ranges from about 65-200 kJ/mol [46]. Oberson and Ankem determined that the activation energy for diffusion-controlled time dependent twinning was close to the low end of that range. Assuming an activation energy of 65 kJ/mol, and a diffusion coefficient of $1.0 \times 10^{-4} \text{ m}^2/\text{s}$ [46], the diffusivity of oxygen in α -titanium under zero stress and at room temperature (D_0) can be calculated using Eq. (4.2) and is approximately $4.04 \times 10^{-16} \text{ m}^2/\text{s}$. As introduced in *Section 4.3*, the ability of a twin to propagate is directly related to the diffusivity of oxygen in α -titanium. If the assumption is made that an advancing twin boundary is related to the diffusion of a species from the surface into the bulk of a specimen, the center plane of a twin would correspond to the surface of the specimen and the distance from the center plane of the twin to the twin boundary at the farthest point corresponds to the effective diffusion distance [98]. If the average twin thickness is represented by W , then $x_{\text{eff}} = 1/2W$. Using this relationship and the test duration of the four experiments, the

average predicted twin thicknesses were calculated using Eq. (4.1) as: $0.02 \mu\text{m}$ ($10^{-1} /\text{s}$), $0.07 \mu\text{m}$ ($10^{-2} /\text{s}$), $0.70 \mu\text{m}$ ($10^{-4} /\text{s}$), and $6.96 \mu\text{m}$ ($10^{-6} /\text{s}$).

The predicted twin thicknesses as calculated all under-estimate the true lamellar thickness of the observed twins. The average twin thickness for the $10^{-1} /\text{s}$ strain rate was $\sim 0.5 \mu\text{m}$. Therefore x_{eff} is equal to $0.25 \mu\text{m}$. Here it is assumed that during the $10^{-1} /\text{s}$ strain rate experiment, twin nucleation occurred at the start of the test. With such a short test duration (0.3 s) and very high ramp rate, the specimen very quickly reaches plastic flow and the authors feel this is a valid assumption. Instantaneous twinning has also been seen in an α -Ti-0.4wt.%Mn alloy [16]. Inserting the values for x_{eff} and t into Eq. (4.1) gives a diffusivity of oxygen under stress (D_{σ}) of $2.08 \times 10^{-13} \text{ m}^2/\text{s}$. The peak flow stress (σ_{app}) observed during this test was $\sim 460 \text{ MPa}$. Using these values in Eq. (4.3), the value of the activation volume constant for this alloy (V') can be solved for and is $\sim 5.59 \times 10^{-29} \text{ m}^3$. This value for V' can now be used to calculate what the diffusivity of oxygen should be at different stress levels. The calculated values for oxygen diffusivity under stress are: $2.09 \times 10^{-13} \text{ m}^2/\text{s}$ ($10^{-1} /\text{s}$), $1.52 \times 10^{-13} \text{ m}^2/\text{s}$ ($10^{-2} /\text{s}$), $9.09 \times 10^{-14} \text{ m}^2/\text{s}$ ($10^{-4} /\text{s}$), and $4.43 \times 10^{-14} \text{ m}^2/\text{s}$ ($10^{-6} /\text{s}$). Using Eq. (4.1), the corresponding twin thicknesses should be approximately: $0.5 \mu\text{m}$ ($10^{-1} /\text{s}$), $1.4 \mu\text{m}$ ($10^{-2} /\text{s}$), $10.5 \mu\text{m}$ ($10^{-4} /\text{s}$), and $73 \mu\text{m}$ ($10^{-6} /\text{s}$). These results are in much closer agreement with the observed results as obtained by SEM and optical microscopy. The complete results, including the corresponding activation energies for each of the testing situations are shown in Table 4.3.

Table 4.3. Results of the experimental calculations and results of the constitutive relations for twinning observed during the tensile investigations. The modified constitutive relation incorporated a stress factor into the predictive equation described by Eq. (4.2).

	Strain Rate	Experimental	Predicted	Modified
Average Twin Thickness (W), μm	10^{-1} /s	0.5	0.02	0.50
	10^{-2} /s	3.5	0.07	1.35
	10^{-4} /s	12.5	0.70	10.44
	10^{-6} /s	20	6.96	72.91
Diffusivity (D), m^2/s	10^{-1} /s	2.08E-13	4.04E-16	2.08E-13
	10^{-2} /s	1.02E-12	4.04E-16	1.52E-13
	10^{-4} /s	1.30E-13	4.04E-16	9.09E-14
	10^{-6} /s	3.33E-15	4.04E-16	4.43E-14
Activation Energy for Deformation Twinning (Q), kJ/mol	10^{-1} /s	50	65	50
	10^{-2} /s	46	65	50
	10^{-4} /s	51	65	52
	10^{-6} /s	60	65	53

The predicted effective penetration distance was at first found to be well off from the experimental results; however, it is known that higher resolved shear stresses can yield thicker twins [94], and after applying the strain modification factor caused by an applied stress with Eq. (4.3), the predicted measurements were much closer. The lowest strain rate experiment was overestimated by a significant margin, but this is not concerning because many factors come into play which could limit a twins final thickness, including the grain size of the material, the orientation of the grain with respect to the stress axis, and the presence of other twins and their stress fields in a particular grain. These factors are discussed in the following sections (*Sections 4.8.2 and 4.8.3*) and the results are consistent with the measurements obtained by this study.

The activation energies calculated from the experimental twin thicknesses are all very close for the three larger strain rates (10^{-1} , 10^{-2} , and 10^{-4} /s). This suggests that the

same general mechanism is operating across the very different testing conditions. The calculated activation energies are also much higher than the activation energy for slip in α -titanium which verifies that twinning is the rate-controlling mechanism for deformation. The theory of oxygen diffusion dependent twinning also holds because the activation energy for stress assisted diffusion (50 - 53 kJ/mol) is very close to the activation energy for twinning (46 – 60 kJ/mol). It is suggested that the lowest strain rate experiment deviates from the trend because other restrictions to twin growth discussed in *Sections 4.8.3 and 4.8.4* prevent the twin from growing for the duration of the test which would affect the final thickness (W). It has been seen before [16] in an α -titanium alloy that twinning can initiate instantaneously, but after a period of time the stress field surrounding the twin becomes high enough that the twin will stop growing even as the material continues to strain.

4.8.2. Effect of flow stress and internal stresses on diffusion

When a stress is applied, randomly distributed interstitial solute atoms will tend to move to a position of minimum local strain energy (position of maximum strain), where there is the most room for the interstitial. With an advancing twin front, that position of minimum local strain energy is away from the twin boundary and away from soon-to-be annihilated sites. It has been shown that the rise in critical twinning stress with interstitial content is much more significant than the rise in critical slip stress [61]. This agrees with the postulation that for twins to grow in α -titanium, oxygen atoms must first diffuse away from the twin front. The diffusivity of a species is directly related to its concentration. The more interstitial sites that are occupied, the more difficult it will be for these atoms to

diffuse into neighboring lower energy sites. Additionally, as strain rate increases, the stress level in deformed samples increases, which also increases the driving stress for twin nucleation. Therefore more twin embryos will be nucleated per unit area, effectively reducing the twin boundary spacing and resulting in thinner twins.

The authors speculate that the twin thickness observed at the lowest strain rate test does not correlate well with the predictions because of a backstress acting on the twin domain due to the resistance in accommodating the large twin shear by the surrounding grains. Twin growth is a competition between this backstress and the local applied stress. As has been researched before [15, 50, 91, 94], twinning in HCP materials is strongly dependent upon grain size. When a twin is formed, it essentially sub-divides the grain further reducing the effective grain size and reducing the ability of the twin to propagate. More importantly, at high strain rates the diffusion of oxygen away from annihilated octahedral interstitial sites limits twin growth so more twin nucleation is required to accommodate more strain.

4.8.3. Volume fraction of twins

A key point to note about the experiments conducted in this study is that all samples were tested to only 3% strain. At higher strains, twinning begins to saturate and the ability to detect an effect on twinning by strain rate disappears [50, 56]. This study, as well as previous research [56, 94, 115], shows no statistically significant difference in the volume fraction or area fraction occupied by twins at different strain rates when the volume fraction of twinning is determined using the ASTM E562 method. Based on the ASTM method and the size of the grid that was used to determine the volume fraction,

the volume fraction values are accurate to +/- 3%. Although the error in the volume fraction determination is larger than the volume fraction occupied by twins that was measured for a few of the tests, the authors do not feel this is a problem. The values calculated support the theory that the volume fraction occupied by twins does not change with strain rate rather than refuting it. If there was a change in the volume fraction of twins with strain rate, then a statistically significant margin would have been seen. Although the average twin thickness significantly decreases, the number density of twinning increases with an increase in stress and strain rate, verifying that *strain* is the dominant parameter controlling the *extent* of deformation twinning [50].

4.8.4. Effect of grain size on volume fraction of twins

The proposed model begins to deviate greatly from the observed experimental results at the very lowest strain rate. This model does not account for the ultimate grain size of the grain containing a specific twin; therefore, given the right conditions it may be possible for a predicted twin thickness to be larger than the grain containing it. As such, at the faster strain rates the predicted twin thickness is much smaller than the grain size of the material so grain size effects would be very small; however, the twin thickness predicted for the slowest strain rate approaches almost $\frac{1}{2}$ the diameter of the grain. At this size it is obvious that grain size constraining effects would be in effect. The effect of grain size on twinning has been extensively studied in α -titanium and other HCP materials [15, 17, 25, 42, 50, 66, 71, 84, 116]. While the propensity for twinning increases with an increase in grain size, a twinning event essentially sub-divides a grain and the effective grain size decreases with increasing strain. Since the model presented

here does not address the influence of grain boundaries, other twin boundaries, dislocations, and other features which inhibit deformation twinning, the size limited twins at lowest strain rate could easily be accounted for by these mechanisms. It should be noted that the alloys used in this investigation had sufficiently large grain sizes to best *reduce* the effect of these mechanisms which could inhibit twinning.

4.9. Concluding remarks

A systematic investigation of the low temperature ($<0.25T_m$) twinning behavior of a large grain sized (200 μm) α -Ti-1.6V alloy at four distinct strain rates was performed. Specimens were tested at strain rates of 10^{-1} /s (a), 10^{-2} /s (b), 10^{-4} /s (c), and 10^{-6} /s (d). It was found that deformation twinning was the primary deformation mechanism during these tests and that the number of twins increased with increasing strain rate as expected. It was also found that twin thickness decreases with increasing strain rate which is contrary to previous thought about the growth behavior of twins. In addition, it was found that for a given strain, the total volume fraction of twins did not vary with a change in strain rate.

It has been previously postulated that the unexpected twinning behavior is the result of twin growth being dependent upon oxygen diffusion away from annihilated interstitial sites. Based on this assumption and the knowledge of the activation energy for oxygen diffusion at room temperatures, predicted twin thicknesses were calculated for the four different strain rates (a-d) used in this investigation. Every one of these predictions *under*-estimated the average thickness of twins actually characterized.

To address the discrepancy between the predicted values and the actual measurements, a stress modification factor was added to the constitutive relation, which predicted twin thickness as a function of the relative flow stress for a given strain rate. After this modification factor was used, the predicted values for average twin thickness, as well as activation energy for twinning/oxygen diffusion, were much closer to the measured values and only the slowest strain rate experiment (10^{-6} /s) deviated from the predictions, where twin thickness was predicted to be much larger than experimentally measured.

The reason for this final discrepancy was attributed to many factors which were not accounted for by the constitutive model but discussed in relation to diffusion-based twinning mechanisms. These include: grain size constraints, number of twins nucleated per unit area as a function of flow stress, backstresses acting on the twin fronts which would be in competition with the applied stress, and test duration. However, the authors feel that the results of these experiments verify the theory that twinning in HCP titanium is highly dependent upon interstitial solute atoms in the alloy and twin growth in α -titanium relies on oxygen diffusion away from the twin front. The results of this investigation demonstrate a way to control deformation twinning and in turn the mechanical properties of these alloys, helping to develop advanced materials with much improved properties.

Chapter 5

The Effect of β -phase Metastability on Low Temperature Deformation

Behavior of β and $\alpha + \beta$ Ti Alloys

In the last two decades, there have been many papers demonstrating the effect of β -phase stability on the mechanical properties of the metastable titanium alloys, but no effort has been made yet to present a comprehensive look at the deformation mechanisms influenced by β -phase stability and grain size in these single phase β and two phase $\alpha+\beta$ alloys. The aim of this paper is to take a comprehensive look at the previous research and put together a methodology for what factors will control β phase stability, what deformation mechanisms β -phase stability influences, and how these deformation mechanisms affect the mechanical properties of these alloys.

5.1 β -phase metastability

Previous research has well established that the stability of the BCC structure in single and two-phase titanium alloys [3, 17, 117-134] depends on the extent of alloying elements and heat treatments as shown in Figure 5.1 [119]. The amount of β stabilizer required to retain 100% of the β phase at room temperature is defined by the Molybdenum Equivalency (MoE) [117]. MoE is used as a measure for the amount of β stabilizer required to prevent a martensitic transformation when quenching to ambient temperature. The MoE for a given stabilizing element is defined as the ratio of the amount of β stabilizing element to the amount of Molybdenum (Mo) required for the

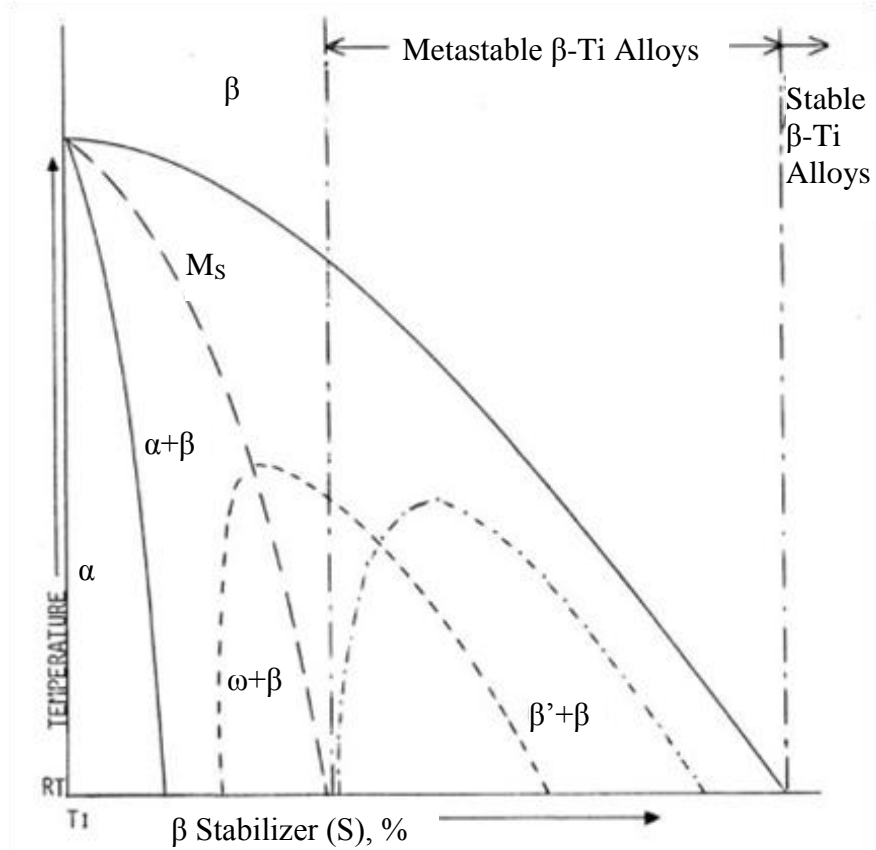


Figure 5.1. A schematic of a pseudo-binary equilibrium diagram showing the ranges of β and ω stability as a function of added β stabilizer [119].

same degree of β -phase stability. A simple formula for Molybdenum equivalency of some of the more common alloying elements of titanium may be derived as:

$$\begin{aligned}
 \text{MoE} = & 1.0 (\text{wt.\%Mo}) + 0.67 (\text{wt.\%V}) + 1.53 (\text{wt.\%Mn}) \\
 & + 0.44 (\text{wt.\%W}) + 1.6 (\text{wt.\%Cr}) + 0.28 (\text{wt.\%Nb}) \\
 & + \dots
 \end{aligned}
 \tag{5.1}$$

During a quench from the β -phase, there are other non-equilibrium phases that can form including martensites (including α'), ω -phase and β' -phase. Jepson et al. [135] showed that the local effect of alloying inhibits martensitic transformation and the speed of transformation. All β alloys have been found to deform at ambient temperature by coarse and fine slip only [126], by slip and formation of stress induced plates (SIP) such as twins or martensite [126], or by the formation of new stress-induced metastable phases like the ω -phase [118, 131, 136-140]. It has also been observed that as the alloying element is increased, i.e. the stability of the β -phase is increased; the deformation mode changes from twinning/martensite formation to slip [120, 124, 125, 128]. This review will also address the effect of the α -phase on the deformation mechanisms of the β -phase, and *vice-versa*, in $\alpha + \beta$ titanium alloys and their relationship to the behavior of single-phase β alloys.

5.1.1 The role of the ω -phase

As can be seen in the previous phase diagram (Figure 5.1), the ω -phase would be present for most alloys of titanium using transition metals and tested at room temperature, depending on the stability of the β -phase. The ω phase is present in the lower stability metastable alloys. For example, when the β stability MoE is 19.9 for a Ti-Mn alloy, only diffuse streaking is observed, indicating that the ω phase is about to form. However, when the β stability MoE is 9.9 for a Ti-V alloy, the ω phase has not completely formed, as shown in Figure 5.2. The ω -phase is metastable with respect to both the α and β phases, and is a nanostructured phase present within the β -phase. The ω -phase has been shown to have drastic effects on the mechanical behavior of metastable β titanium alloys

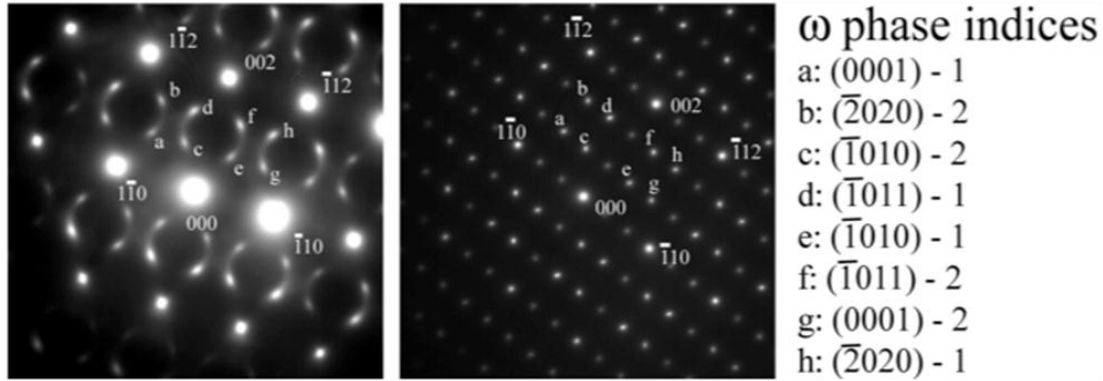


Figure 5.2. Selected area diffraction pattern comparing the degree of formation of omega phase in the β phase of the $\alpha + \beta$ (a) Ti-6.0 wt pct Mn (β -phase MoE=19.9) and (b) Ti-8.1 wt pct V (β -phase MoE=9.9) alloys. Note pre-omega-phase streaking of ω spots of the β phase of $\alpha + \beta$ Ti-6.0 wt pct Mn SADP, which are consistent with incommensurate ω formation, compared with the sharply defined spots of the β -phase $\alpha + \beta$ Ti-8.1 wt pct V SADP. The ω phase indices and orientation are provided. The extra spots in the Ti-8.1V pattern are due to double diffraction [21, 22, 156].

[141-144], and so therefore must be also considered here. The ω -phase is formed when titanium is alloyed with β -stabilizers and can form either upon quenching from the β -phase field, or from ageing of such a quenched alloy. The ω -phase has a hexagonal structure and forms a coherent interface with a $(110)[111]_{\beta}||(\bar{1}\bar{1}\bar{2}0)[0001]_{\omega}$ relationship to the surrounding β -phase.

5.2. Deformation mechanisms in metastable Ti alloys

5.2.1. Single Phase α -Ti Alloys

The room temperature deformation of single-phase α alloys, such as Ti-1.6V and Ti-0.4Mn, has been extensively covered in the works of Oberson, Greene, and Ankem [16, 24, 145] as well as others [33, 146-150]. It was shown first by Ankem *et al.* [16] that extensive creep deformation can occur at room temperature in coarse grained alpha

titanium alloys, when tested at below the 0.2% yield stress. The phenomena was attributed to slip as well as time dependent $\{1\bar{1}02\}\langle 10\bar{1}\bar{1}\rangle$ or $\{1\bar{1}01\}\langle 10\bar{1}\bar{2}\rangle$ twinning. Later, Neeraj *et al.* reported that primary creep in single phase α Ti-6Al alloys can also occur at low temperatures in coarse grained materials. This phenomenon was attributed to planar slip. These studies therefore show that the alloying elements can determine whether the primary creep at room temperature is due to time dependent twinning and slip or solely due to planar slip. While these earlier studies show that the time dependent twinning is due to the coarse grain size, the later studies indicated that in the presence of the β -phase, the twinning can also occur even if the α -platelet size is thin in two phase $\alpha + \beta$ titanium alloys, as described later.

5.2.2 Single phase metastable β -Ti Alloys

Single-phase β alloys have long been shown to have excellent mechanical properties including creep resistance. Additionally, they show a good response to heat treatment and their microstructures can be easily modified. While the deformation modes for β titanium alloys can vary widely depending upon grain size and alloy composition [25, 117, 119-122, 124, 126, 128, 151], one trend involving β stability and resulting deformation mechanisms is apparent and discussed.

While β titanium alloys show good creep resistance in general, it is evidenced from previous research [17, 25], that the net creep strain increases as the grain size increases. There also exists a greater amount of deformation with coarser slip lines in larger grain sized specimens of Ti-13.0Mn, Ti-9.4Mn, and Ti-14.8V [17]. The deformation features observed before and after creep deformation match those observed

during tensile deformation and are detailed in the next section. It should be noted that the creep strain for these specimens increases significantly with increasing grain size. This observation at room temperature is opposite of what is observed at high temperature. This difference in the effect of grain sizes between high temperature and room temperature has been attributed to the difference in operational deformation mechanisms [17]. Specifically, at high temperatures, the predominant deformation mechanism is grain boundary sliding; where an increase in grain size would result in decreased creep strain.

To demonstrate the effect of β -phase stability on the deformation mechanisms of β titanium alloys, two model systems will be reviewed. Single-phase Ti-V and Ti-Mn β alloys have been selected for review due to the extensive amount of research performed on these alloys by Ankem *et al.* [17, 25, 119, 126, 152]. In addition, the deformation mechanisms discovered for the single phase β alloy, Ti-9.4Mn [17] will also be discussed to help illustrate the effect of β stability in one alloy system. Tensile testing, optical microscopy, scanning electron microscopy (SEM), and transmission electron microscopy (TEM) studies have all been performed during the course of the investigations reviewed. The deformation of single-phase β alloys such as Ti-13.0Mn and Ti-14.8V are dependent upon β -phase stability as well as grain size. The MoE has been calculated as 19.9 for Ti-13.0Mn and 9.9 for Ti-14.8V [17]; therefore the stability of Ti-13.0Mn is much higher than that of Ti-14.8V. During tensile tests conducted at a strain rate of $3.128 \times 10^{-5} \text{ s}^{-1}$, Ti-13.0Mn generated a YS of 940 MPa and deformed solely by coarse and wavy slip [21, 22, 146]. Alternatively, Ti-14.8V exhibited a YS of 774 MPa and deformed by slip and the formation of stress-induced $\{332\}[113]$ twins [25, 152]. These twins contained two

orientations of the ω -phase. Additionally, it was found that the Ti-9.4Mn alloy (MoE = 14.3) [17] had a YS of 1030 MPa with negligible work hardening and deformed by extensive slip [17]. It should be noted now that in the Ti-14.8V alloy (less stable MoE), the modes of deformation were stress-induced plates (SIP) and slip; whereas in the Ti-13.0Mn alloy (more stable MoE), the predominant deformation mechanism was slip [17, 146].

The assumption would be that in an alloy with intermediate stability, there should be slip accompanied by some SIP formation. In the Ti-9.4Mn alloy, there was no SIP observed which suggests that there is some critical β -phase stability above which slip is the only operating mode of deformation [17]. The TEM analysis of the undeformed and deformed Ti-9.4Mn specimen revealed the presence of ω -phase as discrete spots in the BCC β -matrix. These investigations showed no evidence or indication of SIP formation and twinning. The matrix appeared to be unchanged after tensile deformation evidently showing that there is no SIP formation or twinning. One should note that in a Ti-14.8V alloy [25], the ω -phase is present before deformation, and in a higher stability Ti-13.0Mn alloy, there is no ω -phase except for a pre- ω -phase streaking. This implies that in a more stable β -alloy, the ω -phase is absent and the deformation is due to slip [17]. These results lead to the important conclusion that the formation or presence of ω -phase in the three β -alloys considered here is associated with the stability of β -phase and not a result of deformation [17]; additionally, the presence of the ω -phase may also be contributing to the formation of twins.

During creep tests, the single-phase alloy, β -Ti-13.0Mn (β -phase of Ti-6.0Mn), with a grain size of 200 μm , showed negligible creep strain of only 0.03% strain over a

test period of 400 hours and deformed only by rare coarse slip, with no observed twinning [16, 119]. Conversely, the single-phase alloy β -Ti-14.8V (β -phase of Ti-8.1V) crept to a strain 0.101% and deformed by slip, instantaneous twinning, and time-dependent twinning [15]. For comparison, the Ti-9.4Mn alloy crept to a strain of \sim 0.07% and deformed by slip. The deformation features for the creep tested Ti-9.4Mn alloy were very similar to those observed during tensile deformation. Only slip was observed in the Ti-9.4Mn alloy, and from micrographs taken during the test, it was determined that most of the slip lines were generated in the first few minutes of the test [17].

Other β alloys have been shown to behave similarly. Specifically, research performed by Xu *et al.* [128], Grosdidier *et al.* [120, 153], Zhao *et al.* [129], and Kim *et al.* [122] have presented similar results. Explicitly, the work of Grosdidier *et al.* showed that microstructure as well as β stability plays an important role in controlling the formation of martensite in a Ti β -Cez alloy. For example, large β grains favor the formation of stress induced martensite, but a decrease in the martensitic temperature as controlled by a higher β stabilized alloy inhibits the formation of SIM [120, 153]. In regards to the newly developed Ti-Nb-Ta-In/Cr β alloys, Xu *et al.* showed that the lower β stability In based alloy deformed by martensite formation, twinning, and slip; whereas, the higher β stability Cr based alloy only deformed by slip [128].

5.2.3 Two-phase α + metastable β Ti Alloys

Many investigations have studied the tensile and creep deformation mechanisms of various two-phase Ti alloys. For reference, a few of these alloys will be discussed here. To demonstrate the effect of β -phase stability on the deformation mechanisms of α

+ β titanium alloys, two-phase Ti-V and Ti-Mn alloys have been selected for review such that the chemistry of the single phase β alloy reviewed earlier would match the component β -phase in the two-phase alloy. Ti-6.0Mn and Ti-8.1V are two titanium alloys whose component β phases have the same chemistry and therefore same MoE as the single phase Ti-13.0Mn and Ti-14.8V alloys. This is due to the fact that all of the single and two phase alloys were heat treated or annealed at the same temperature where the phase composition is determined by the tie lines. Tensile testing, creep testing, optical microscopy, SEM, and TEM have all been performed during the course of the investigations reviewed.

It should be noted that all of the two-phase titanium alloys reviewed exhibited similar behavior in regards to grain size and β stability effects on the resulting deformation products. To illustrate this, the research of Ankem *et al.* [24, 131-134, 145], Balcerza *et al.* [136], and Gerland *et al.* [146], who investigated the interactions between the two phases, is reviewed. During tensile tests conducted by Jaworski & Ankem [21, 22], a two-phase alloy Ti-6.0Mn (higher MoE of metastable β phase) demonstrated a YS of 623 MPa and showed some amount of strain hardening. The $\alpha + \beta$ Ti-6.0Mn alloy demonstrated fine slip in the α -phase and some limited α -phase $\{10\bar{1}2\}$ type twin formation and interphase interface sliding [21, 22]. In contrast, a $\alpha + \beta$ Ti-8.1V alloy (lower MoE of metastable β phase) yielded at approximately 597 MPa, showed no significant strain hardening, and showed many coarse deformation products [21, 22]. After SEM and TEM analysis of the $\alpha + \beta$ Ti-8.1V alloy, these products were shown to be twins in the α -phase and stress-induced martensite (SIM) in the β -phase, which spanned many grains of the specimen, not shown here [21, 22]. Additionally, it should

be noted that TEM analysis also revealed the presence of the ω -phase in the lower stability alloy, as shown in Figure 5.2.

Creep tests performed by Jaworski & Ankem [22] resulted in similar deformation features to the tensile tests. The $\alpha + \beta$ Ti-8.1V alloy (total creep strain $\varepsilon = 0.37\%$) exhibited 16% greater creep strain compared to the $\alpha + \beta$ Ti-6.0Mn alloy ($\varepsilon = 0.22\%$) [22]. Creep deformation in the $\alpha + \beta$ Ti-6.0Mn alloy has been primarily attributed to fine slip in the α -phase and some infrequent interphase interface sliding in SEM micrographs. In stark contrast, the deformation products in $\alpha + \beta$ Ti-8.1V are highly visible and travel over the distance of many grains. Using TEM analysis, these deformation features have been identified as slip bands or twins in the α -phase and stress-induced hexagonal martensite in the β -phase [22].

The additional creep strain experienced by the $\alpha + \beta$ Ti-8.1V over alloys such as β Ti-13.0Mn or even $\alpha + \beta$ Ti-6.0Mn over the same test period can be explained by the difference in deformation mechanisms, specifically the formation of stress-induced martensite in the β -phase and a greater number of twins in the α -phase of $\alpha + \beta$ Ti-8.1V [22]. In both the $\alpha + \beta$ Ti-8.1V and $\alpha + \beta$ Ti-6.0Mn alloys, the α -phase deformed by extensive fine slip with some coarse slip also observed in the $\alpha + \beta$ Ti-8.1V alloy [22].

The TEM analysis of the $\alpha + \beta$ Ti-8.1V specimens as conducted by Jaworski & Ankem [21, 22] revealed that the coarse lines visible in SEM micrographs were actually a combination of stress-induced hexagonal martensitic plates (α') in the β -phase and either twins or coarse slip in the α -phase [21]. However, the single-phase β -Ti-14.8V, which has the same chemical composition as the β -phase of the $\alpha + \beta$ Ti-8.1V, only showed time dependent $\{332\}$ twinning and no martensite was observed [154]. In metastable β

alloys, two types of SIM are common: hexagonal martensite (α') and orthorhombic martensite (α''). The plates in this alloy were confirmed to be hexagonal with selected area diffraction patterns, not shown here. Additionally, the Burgers orientation relationship was obeyed between the martensite and the β -phase, and the martensite was not internally twinned with a straight α'/β interface which suggests a habit plane. These results clearly showed that the deformation mechanisms in the two-phase alloy could differ from those of the single-phase alloy even when the component phase chemical composition is equivalent to the single-phase alloy. The phenomenon of interest is the formation of SIM in the β -phase of $\alpha + \beta$ Ti-8.1V as opposed to twins in the single-phase alloy, as well as the formation of twins in the single phase α -alloy even though the platelet size was small ($<5 \mu\text{m}$). Twinning and martensite formation become the dominant mechanisms at low β stability even though there are many slip systems to accommodate deformation. In order for SIM to occur in the place of twinning, the relative activation energy must be lowered relative to twinning or additional stresses must be applied.

5.3. The role of β -phase stability on tensile deformation mechanisms

5.3.1. Single-phase β -Ti alloys

In single-phase β titanium alloys, the role of β -phase stability and the role of the ω -phase on the stability of the β -phase are not very clear. It is known that as the stability of the β -phase is lowered through the lowering of the amount of a stabilizing element, or the use of a less-effective β -stabilizer, the deformation products change from slip to twinning. There are at least three reasons why the mechanisms of single-phase

metastable β alloys can be different. The first reason is related to the fact that in the higher stability alloys, the weight percent of alloying elements is higher. It is possible that the addition of alloying elements can hinder the formation of twins more effectively than opposing slip; therefore, it is possible to have only slip as you increase β -phase stability.

The second factor is related to the presence of the ω -phase. As mentioned before, in the lower stability alloys, the ω -phase is present. It is possible that this ω -phase is responsible for twinning in lower stability alloys. It should be noted that coinciding with this transformation from slip deformation to twinning and martensite deformation is the appearance of the ω -phase in the β microstructure. This suggests that the ω -phase is playing a critical role to the deformation of the phase. However, after twinning, the ω -phase is still present within the twinned region of the grain. During a martensitic transformation, both the ω -phase and the β -phase would be consumed. The presence of the ω -phase within a twin suggests two possible scenarios. Either the ω -phase sheared along with the β -phase, or it dissolved during twinning and recrystallized along its preferred directions within the twin after twinning was complete. It may be impossible to determine which of these mechanisms is operating. Alternatively, it may be possible that the ω -phase is acting as a nucleation site for the twinning process. Being that the ω -phase is an intermediate phase between the stable α -phase and the metastable β -phase, it may be possible that twinning is occurring in the low stabilized alloys because the ω -phase is lowering the τ_{crss} for twinning close to or lower than slip. The mechanisms for this however are not known and further investigations are needed.

The third reason for the change in deformation mechanisms may be related to the chemical free energy difference between the metastable β -phase and the martensite (α') phase. As the stability decreases, the chemical free energy difference between these two phases increases. Therefore, any minor stresses developed because of various reasons, including cooling from high temperatures or applied stresses, can promote the formation of martensite.

5.3.2 Two-phase $\alpha + \beta$ Ti alloys

In addition to the factors mentioned above for single-phase metastable β alloys, additional factors come into play in regard to the two-phase $\alpha +$ metastable- β alloys. These include elastic and elasto-plastic interaction stresses between α and β phases, crystallographic relations between phases, and residual stresses due to cooling from high temperatures. It is quite possible to have residual stresses in the microstructure because the coefficient of thermal expansion is different between α and β phases; however, observations of the microstructures of the as-quenched alloys reviewed showed no twins and no martensite, indicating that these residual stresses may not be significant enough to produce these transformations.

Initially, interaction stresses develop at the α/β interfaces due to different amounts of strains for the same applied stress. At lower stresses, for a given amount of applied stress, the β phase deforms more than the α phase because the β phase is elastically softer than the α phase, as shown in Figure 5.4. Therefore, at the α/β interface, the stress on β has to come down and the stress on the α phase has to go up so that the interfacial strain will be the same, to maintain compatibility. This means that the

β -phase can apply a stress, in addition to the applied stress, on α -phase causing slip or twinning in the α -phase. This can explain why twinning can be seen in the α -phase even though the α platelet size is very small. Consequently, once slip or twinning initiates in the α -phase, it can apply very strong interaction stresses on the β -phase in addition to the applied stress, see Figure 5.4. Such interaction stresses are found to be significantly higher in the martensitic system in the β -phase as opposed to twinning in the β phase [21, 22]. This is one of the reasons why martensite forms in β instead of twinning in the presence of α -phase.

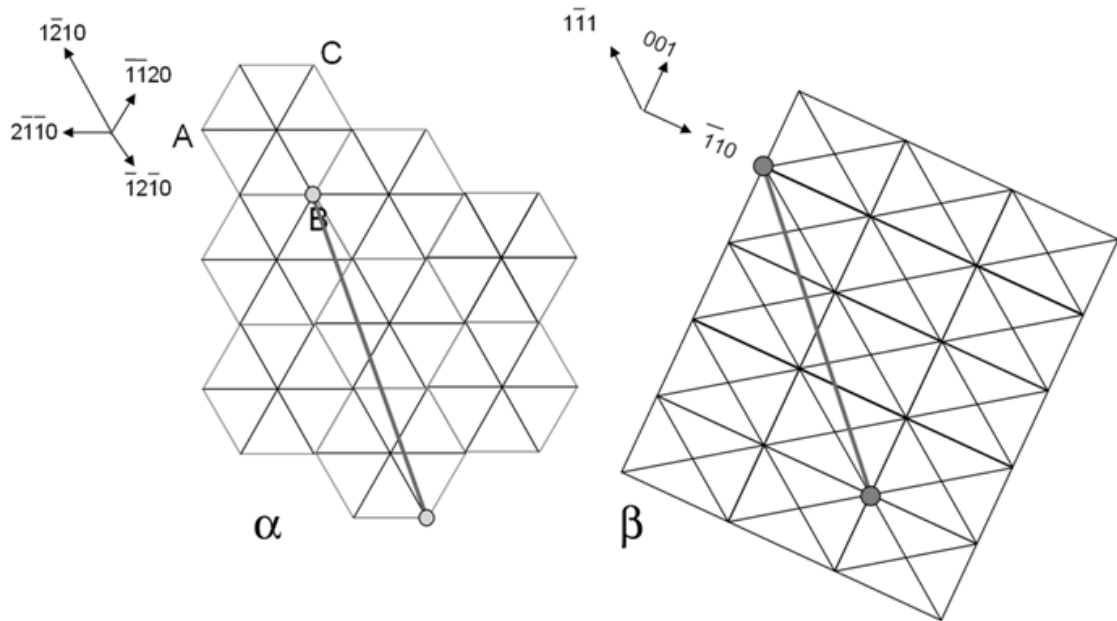


Figure 5.3. Illustration of the $[1\bar{2}10](0001)//[1\bar{1}1](110)$ Burgers orientation relationship between the α and β phases in an $\alpha + \beta$ titanium alloy with Widmanstatten microstructure. Diagram shows the $(0001)_{\alpha}$ and $(110)_{\beta}$ planes. The interface plane is $(\bar{5}140)//(\bar{3}34)$; which is normal to the $(0001)_{\alpha}$ and $(110)_{\beta}$ planes and is indicated as a trace in each phase [21, 22].

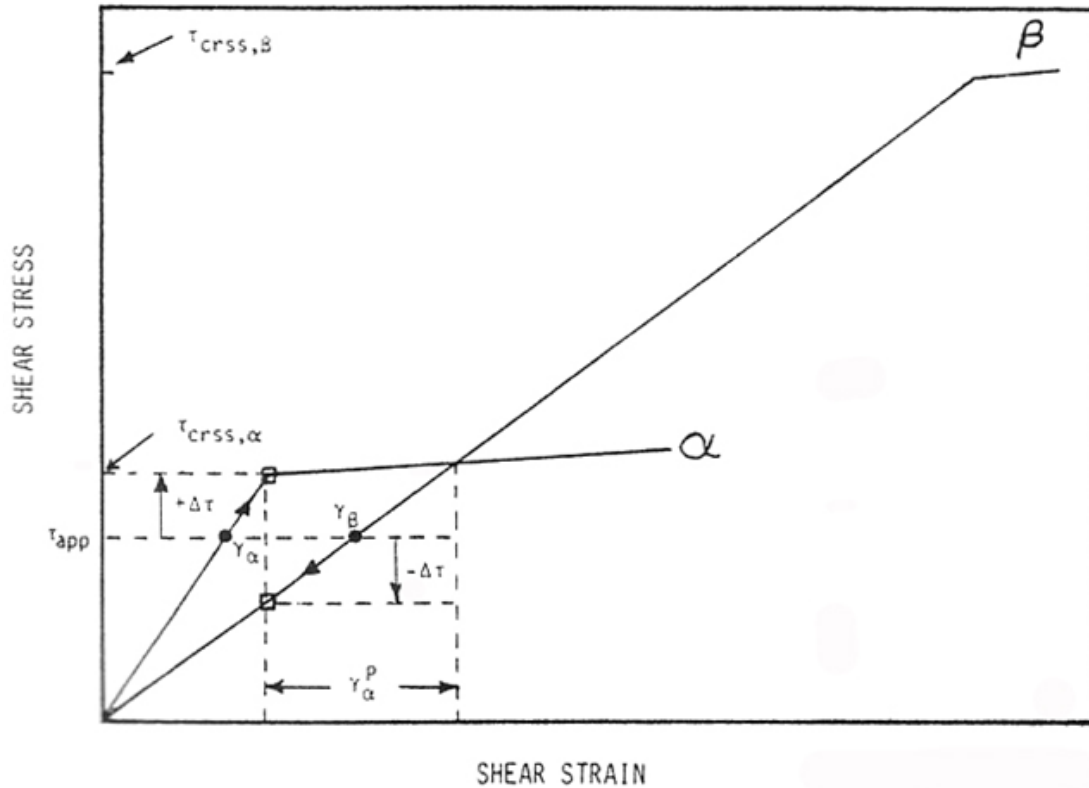


Figure 5.4. Elastic interaction stress on α and β phases of a titanium alloy. The interaction of the stronger but lower modulus β phase with the α phase initially increases the stress in α . Once significant plastic deformation occurs in α , elasto-plastic interaction stresses act on the β phase [21, 22].

The third reason that martensite (α') may form in the β -phase, is related to the templating effect. It was found that the martensite in the β -phase and the α -phase have a twin relationship. This interface between α and α' has a lower misfit orientation than the α - β interface and so a martensitic formation is favored. The additional stresses from slip and twinning in the α -phase that act on the $\beta \rightarrow \alpha'$ transformation, as noted before, are only present in the two-phase alloys. This is why twinning is the predominant mechanism in the single-phase alloy Ti-14.8V rather than SIM seen in the $\alpha + \beta$ Ti-V alloys. Where β -stability comes into play is when SIM is formed in the β phase of Ti-

8.1V but not in the β phase of Ti-6.0Mn or Ti-9.4Mn. SIM occurs because the stress applied effectively raises the martensitic transformation temperature to ambient temperature. The change in Gibbs Free Energy for a martensitic transformation is:

$$\Delta G = A\gamma + \Delta G_S - V\Delta G_V \quad (5.2)$$

In comparing β titanium alloys with different stabilities, the less stable alloys will have a greater change in volume free energy upon transformation, resulting in a greater likelihood of martensitic transformation.

A fourth reason for the differing mechanisms between single phase metastable β alloys and two phase $\alpha + \beta$ alloys may also be due to the presence of the ω -phase in the β -phase of these alloys. Kuan *et al.* [139] suggest that the metastable ω -phase which is also present in Ti-8.1V, is an intermediate phase between the α and β phases. This intermediate phase would effectively lower the free energy change required to form martensite. Because of the lack of ω -phase in the Ti-6.0Mn alloy, stresses required to form stress induced martensite (SIM) are higher. The presence of the ω -phase is illustrated by Figure 5.2 [21]. To properly address the relationship of β -phase stability and deformation mechanisms, various other Ti-V alloys were reviewed. Ramesh *et al.* [25] found $\{332\}[113]$ -type twins containing two variants of the ω phase in single-phase Ti-14.8V alloy, with the same chemistry as the β component of the Ti-8.1 wt pct alloy. This result is consistent with the results of Oka and Teniguchi [151] in a Ti-15.5V alloy. Kouland and Breedis [123] found that the stress-induced plates in Ti-16.2V were hexagonal martensite (α'). Menon and Krishnan [155] investigated Ti-V alloys with 5, 10, and 20 wt. pct. V, and found SIM in the Ti-20V alloy. Ling *et al.* [124] investigated Ti-V alloys ranging from 20 to 40 wt pct V and found that, as the solute concentration

was increased, the deformation mechanisms changed from twinning in the 20 wt. pct. V alloy to fine slip and finally coarse slip in the Ti-40wt.%V alloy. Additionally, Xu *et al.* [128] found that in two β alloys with differing β phase stability, the stability of the second phase played a crucial role in whether or not a martensitic transformation would occur under room temperature stresses.

Both oxygen and hydrogen have marked effects on the ω -phase. Oxygen depresses the temperature at which ω phase forms and hydrogen enhances thermal ω -phase formation. These effects are important because the levels of these two elements can vary from alloy to alloy and would therefore affect the variation in the literature results mentioned above. The interactions between the α -phase and ω -phase become possible because of the high concentration of ω -phase within these lower stability β alloys. The observations suggest that the activation energy for twinning can decrease in the presence of ω -phase in the case of single-phase alloys. In addition, the activation energy for the formation of martensite is also decreased in the presence of the intermediate ω -phase. It is reasonable to believe that the activation energy for the formation of martensite is lower than that for the formation of twinning. If the activation energy is met by the interaction stresses between α and β phases, which are much more prevalent on the martensite system as compared to twin system, then one can explain why martensite has formed in the presence of α -phase even though only twins are found in the single-phase β alloys.

Additionally, because the misfit strain between the α and ω phases is high, at the places along the α/β phase interface where α and ω phase interact the plastic deformation of the α -phase places high stresses on the ω -phase planes and directions which facilitate a

$\omega \rightarrow \alpha'$ transformation. Because the resolved shear stresses from α -phase slip or twinning act more strongly on the ω -phase shear systems than the β -phase twinning systems, stress induced martensite becomes far more likely to occur. It should also be considered that there are four main orientations of the ω -phase present in the β -phase; of these, slip in α affects two of them and twinning in α affects the other two; so no matter the primary deformation mechanism in the adjacent α -phase of a two-phase alloy, martensite will form in the β -phase. It has been shown here how the stress induced martensite may form, but the question as to how the martensite propagates through the β -phase must also be considered. If one looks at the orientation relationship between the ω and β phases, $\{\bar{1}010\}\langle 0001 \rangle_{\omega} // \{\bar{1}12\}\langle 1\bar{1}1 \rangle_{\beta}$, it becomes apparent that each shear system for a $\omega \rightarrow \alpha'$ transformation is exactly parallel to the $\beta \rightarrow \alpha'$ shear system. What this means is that once the transformation is started, it will propagate through the β -phase along parallel systems.

We can say conclusively that the deformation products for metastable β titanium alloys are dependent upon the amount of stabilizing element, hence, as the stability is increased, the mechanisms change from SIM to twinning to slip.

5.4. The role of β -phase stability on creep deformation mechanisms

Similarly to tensile tests which have been performed, deformation mechanisms during creep in the two-phase alloys differed from those observed in the single-phase alloys. Creep test results mirrored the results of the tensile testing for Ti-8.1V and Ti-14.8V (same composition β -phase). In the single-phase alloy, the stress-induced plates responsible for deformation were $\{332\}$ type twins; whereas in the two-phase alloy, stress induced martensitic (α') plates were formed in the β -phase. As a single-phase

alloy, Ti-14.8V has a martensite start temperature low enough to prevent a martensitic transformation; however, the presence of α -phase raises the temperature high enough that martensite can form during creep. Specimens tested under creep conditions differ from tensile testing in that the load is constant and any additional stresses required to initiate creep must come from internal stresses. Therefore, interaction stresses are even more important. Schematics of the orientation relationship between the two phases and the interaction stresses experienced by the two phases are shown in Figures 5.3 and 5.4 [21, 22]. For twin nucleation and growth in the α -phase (which is preferred), the β phase must strain to accommodate the α -phase strain. If the β phase is stable enough, it will retard the growth of twins as evidenced by the two-phase alloy Ti-6.0Mn. The limited interphase interface sliding in Ti-6.0Mn is not enough to accommodate the growth in the α -phase, which limits the overall creep strain. The creep results of the single phase β alloys: Ti-9.4Mn, Ti-14.8V, and Ti-13.0Mn were also compared. It has been hypothesized [23, 24] that interstitial oxygen atoms act as pinning sites at the twin/matrix interface to control time-dependent strain. This diffusion of oxygen atoms away from the twin front would explain the increase in twin width with time for the β alloys. A similar mechanism would also be possible for Ti-9.4Mn as well. However, since slip was much more prevalent in Ti-9.4Mn than in Ti-13.0Mn, the pinning sites are not oxygen because the systems should respond in the same way [17]. TEM diffraction patterns showed ω -phase spots before and after deformation in Ti-9.4Mn but were absent in the stable Ti-13.0Mn. This means that the ω -phase could be responsible for pinning of slip lines and creep strain results from slip lines intersecting with the ω -phase and dissolution of the ω -phase [17, 156].

5.5. Concluding remarks

This study was undertaken to gather together the information regarding the effect of the metastable β phase on deformation in single phase and two phase titanium alloys. As of yet, there had not been a comprehensive review of these relations, nor postulations as to how they affect the alloy's final microstructure and mechanical properties. The magnitude of metastability of the β -phase plays a significant role on the deformation mechanisms and the deformation behavior during tensile and creep deformation. The effect of metastability on single-phase β alloys appears to be threefold. The first reason is related to simply the amount of stabilizers added to the titanium. Since the higher stability β -alloys have more alloying elements, it is quite possible that the alloying elements can interfere more strongly with twinning as compared to slip. Therefore, slip can be preferred in very highly stabilized alloys as compared to twinning. As the stability decreases, it was found that ω -phase is present. This ω -phase can also act as nucleation sites for twinning thereby promoting twinning in the lower stability β -alloys. It is to be noted however that slip is an operating mechanism even though twinning is present. As the stability is decreased further, the chemical free energy difference between the metastable β and martensite becomes so high, that any kind of disturbance can result in the initiation/formation of martensite.

In two-phase $\alpha +$ metastable- β alloys, additional factors come into play. These include interaction stresses between the two phases and crystallographic relationships between the two phases. Therefore, some of the deformation mechanisms which have been observed at much lower stability in single-phase β alloys can also be seen in the

higher stability two-phase $\alpha + \beta$ alloys. For example, the α -phase can act as a template for the martensite in β , promoting its formation; where in the absence of α , this may not happen for the given stability of β -phase.

In regard to the creep deformation behavior, the deformation mechanisms are similar to tensile tests; however, the time-dependent effects are important to recognize. Given that for example the twinning in α can be a time-dependent phenomenon, it is quite possible that the growth of the martensite in β in the lower-stability alloys is also time-dependent. While these suggestions need to be confirmed experimentally, it is very important to recognize at this time how the two-phase alloys deform so that optimal chemistry and microstructure of the two-phase $\alpha + \beta$ alloys can be selected for various structural applications.

Chapter 6

Influence of Microstructure and the Second Phase on the Room Temperature Creep Deformation Mechanisms of $\alpha + \beta$ Ti-V Alloys

A detailed investigation of the ambient temperature creep deformation mechanisms of $\alpha + \beta$ Ti alloys was performed using Ti-4.3wt% V, Ti-8.1wt% V, and Ti-12.6wt% V with both Widmanstätten and fine-grained equiaxed microstructures as the model two-phase systems. The creep deformation mechanisms of the two-phase alloys differs from the mechanisms seen in the single-phase alloys with compositions matching those of the α and β component phases. These deformation mechanisms in $\alpha + \beta$ alloys include twinning in fine-grained α phase and stress-induced hexagonal martensite in the β phase. The effect of the α phase on the deformation mechanisms of the β phase and vice-versa has been investigated. Several factors contribute to the creep deformation mechanism in the model two-phase alloys, including elastic interactions stresses and additional shear stresses due to deformation products in adjacent phases.

In contrast to the tensile plastic deformation of titanium alloys, creep deformation may take place at stresses much lower than the yields stress of the material. Any stresses in excess of the applied stress which contribute to the activation of creep processes are only available from internal sources. These internal interaction stresses are the focus of this investigation. These interactions are what result in additional deformation mechanisms in both the α and β phases, and in turn result in increased creep strain. In order to design alloys for improved creep resistance, these interactions must be fully understood.

6.1. Experimental procedure

The Ti alloys have been selected and prepared as discussed in Chapter 3. Prior to creep testing, gold-palladium fiducial grid lines were sputtered onto the samples and grid line spacing was measured carefully. This grid serves as a measurement to verify creep strain and also as a map to track areas of the sample both before and after testing. Ambient temperature (298 K) creep tests were performed on an ATS lever arm creep testing machine at a constant load equal to 95% of the alloy's respective YS, which was determined using ambient temperature tensile tests described in Chapter 3. A Hitachi S-3400N SEM, JEOL 2100 LaB6 TEM, and JEOL 2100F TEM were used to obtain the images and diffraction patterns for this study.

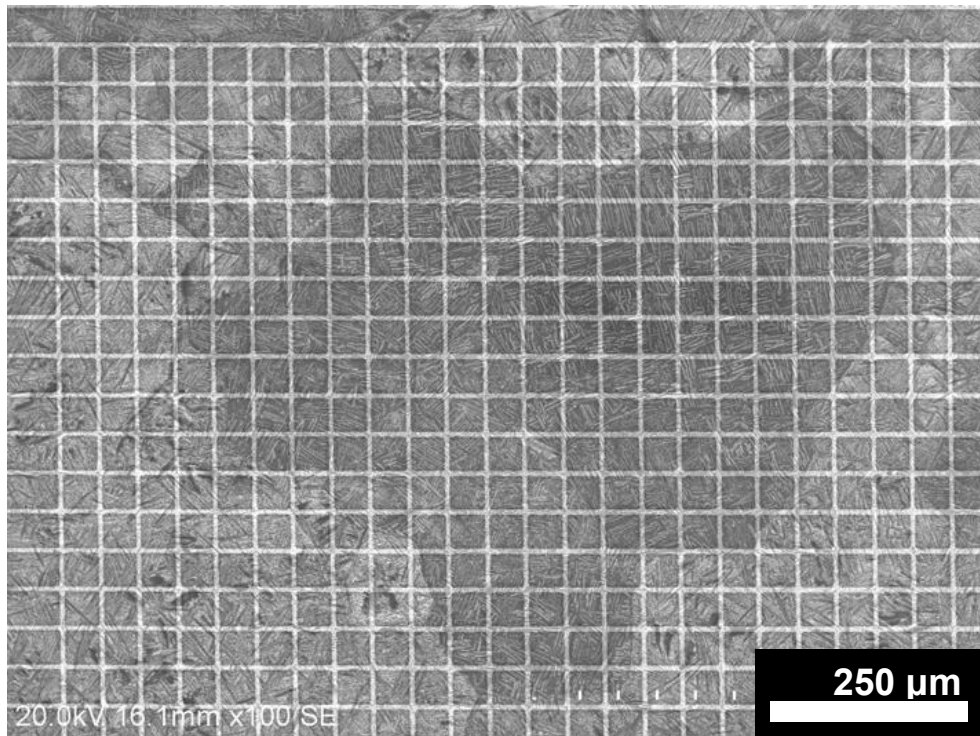


Figure 6.1. SEM micrograph of $\alpha + \beta$ Ti-8.1V with Widmanstätten microstructure before testing; showing fiducial grid used in these investigations.

6.2. Results

6.2.1 Single-phase α and β alloys

The single-phase α and β alloys have been creep tested at 95% of their respective yield stresses in several previous studies. The creep strain of the single-phase α alloys depended on grain size of the material and the creep strain of the single-phase β alloys depended on the stability of the β phase. All of the single-phase alloys showed creep exhaustion behavior during the test periods.

The single-phase α alloy Ti-1.6V with a grain size of 38 μm crept to a strain (instantaneous plastic plus creep) of 1.92% and deformed by fine slip, instantaneous twinning and time-dependent twinning [15]. The single-phase β alloy Ti-14.8V with a large grain size (350 μm) crept to a strain of 0.101% and deformed by slip, instantaneous twinning and time dependent twinning [152]. The single-phase small grained Ti-14.8V alloys (18 – 25 μm) crept to 0.021% strain and deformed primarily by slip, with no significant twinning [25].

6.2.2 Two-phase $\alpha + \beta$ Ti-4.3V alloy

The tensile true stress/true strain curves for the fine-grained equiaxed and Widmanstätten microstructure alloys are shown in Figure 6.2. The fine-grained alloy exhibits a slightly higher ultimate tensile strength, while the elastic modulus and yield strength of each alloy is approximately equal. The Widmanstätten microstructure exhibits a 95% YS of approximately 380 MPa. The fine-equiaxed microstructure exhibits a 95% YS of approximately 390 MPa. Both alloys exhibit a slight amount of strain hardening.

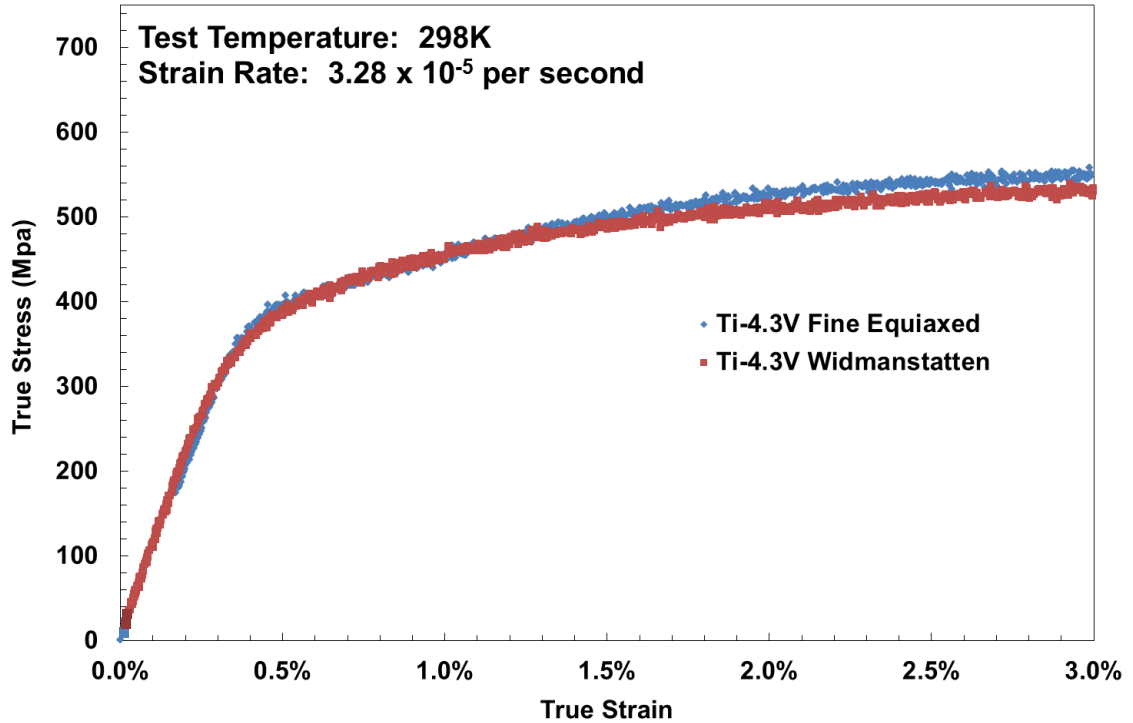


Figure 6.2. Tensile curves of Ti-4.3wt% V, tested at a strain rate of 3.28×10^{-5} /s to a 3% total strain.

The creep curves for the Ti-4.3V fine-grained equiaxed and Widmanstätten microstructure alloys are shown in Figure 6.3. The alloys were tested at 95% of their respective yield stress. A clip on extensometer was used to record strain. SEM micrographs were taken prior to and during testing in the same area of each specimen to record deformation mechanisms. It has been shown that interrupt creep tests and continuous creep tests result in the same amount of creep strain for a given time [145]. The Ti-4.3V alloy with a Widmanstätten microstructure exhibits a slightly greater creep strain ($\sim 0.8\%$) than does the fine-equiaxed microstructure ($\sim 0.77\%$). The creep strain for the Widmanstätten microstructure is 4% greater than the equiaxed microstructure when the instantaneous plastic deformation of $\sim 0.10\%$ is subtracted from the total strain of each

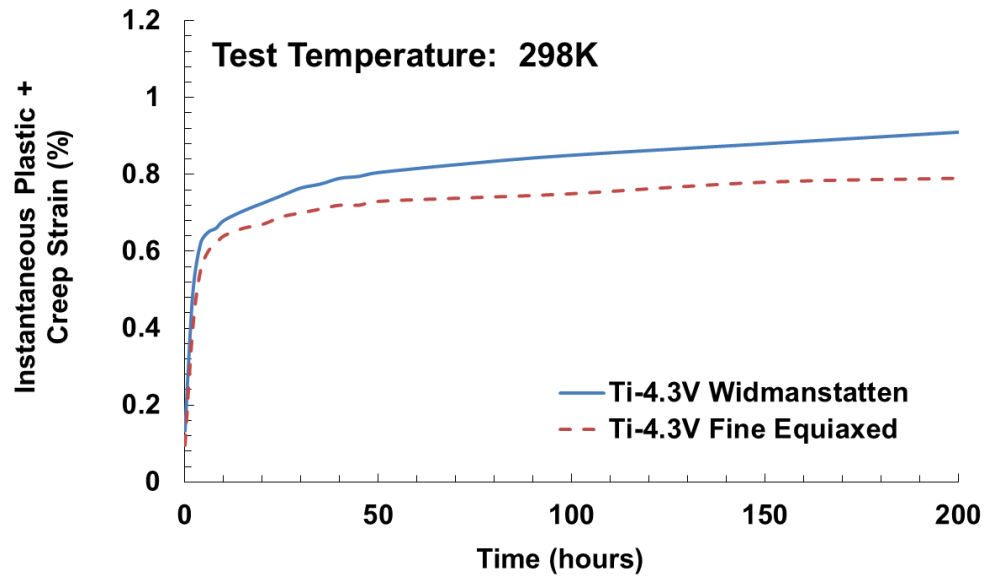


Figure 6.3. Creep curves of Ti-4.3V alloys, creep tested at ambient temperature at 95% of their respective YS.

alloy. Even though the lamellar thickness of the Widmanstätten plates is approximately equal to the grain size of the equiaxed microstructure, there is a difference in the creep strain. This difference is attributed to the difference in creep deformation mechanisms. The following analysis of creep deformation mechanisms was performed on the specimens.

6.2.2.1. Creep deformation mechanisms

Creep deformation in Ti-4.3V with a fine equiaxed microstructure is primarily due to fine slip in the α phase, which is evidenced by a widening of the gold fiducial grid, as measured from before and after SEM micrographs, and TEM analysis. No twinning or stress induced martensite was observed in either phase by TEM, although it is possible, but unlikely, that some very small twins may be present in the α phase in a region of the specimen not investigated. The lack of coarse deformation products can be attributed to

the α phase grain size present in the two-phase alloy being much smaller than the grain size of the single-phase alloy with deformation twinning (226 μm vs. 25 μm) and the total strain of the creep tested specimen is also much less (6.67% vs. 0.9%). However, the results are consistent with the fine grained Ti-1.6V. Figure 6.4 shows SEM micrographs taken of the surface of Ti-4.3V prior to and following creep testing at 95% YS. TEM investigations showed extensive $\langle a \rangle$ type slip on the prism plane of the α phase which is shown in Figure 6.5. These dislocations are $\langle a \rangle$ type screw with $\mathbf{b} = 1/3\langle 11\bar{2}0 \rangle$. No slip, twinning, or stress induced martensite (SIM) was observed in the β phase of this alloy, which is not surprising considering the limited creep deformation of the single-phase β -Ti-14.8V.

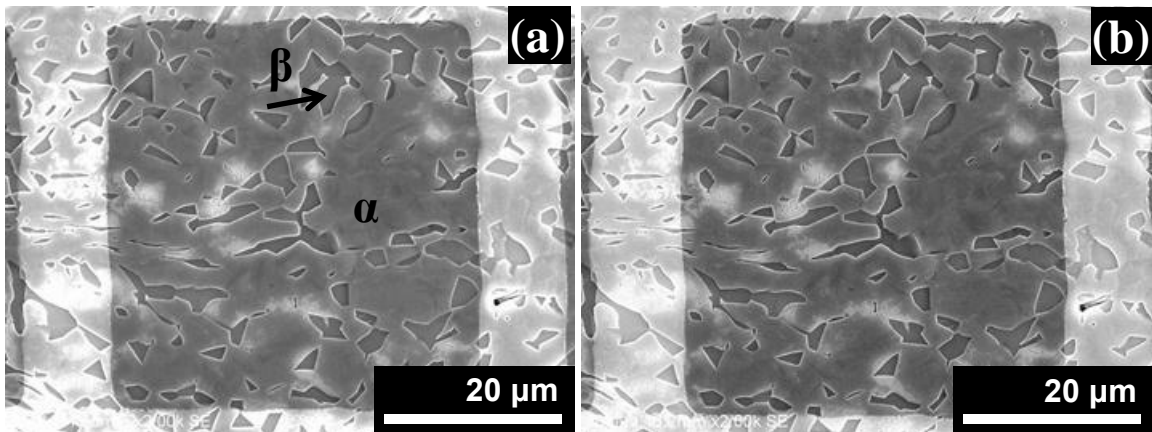


Figure 6.4. SEM micrographs of $\alpha + \beta$ Ti-4.3V (a) before and (b) after creep deformation at 95% YS for 200 hours to 0.86% total plastic strain. There are no coarse deformation features visible on the polished and etched surface, although fine slip in the α phase (light) was noted due to an increase of the fiducial line spacing during testing.

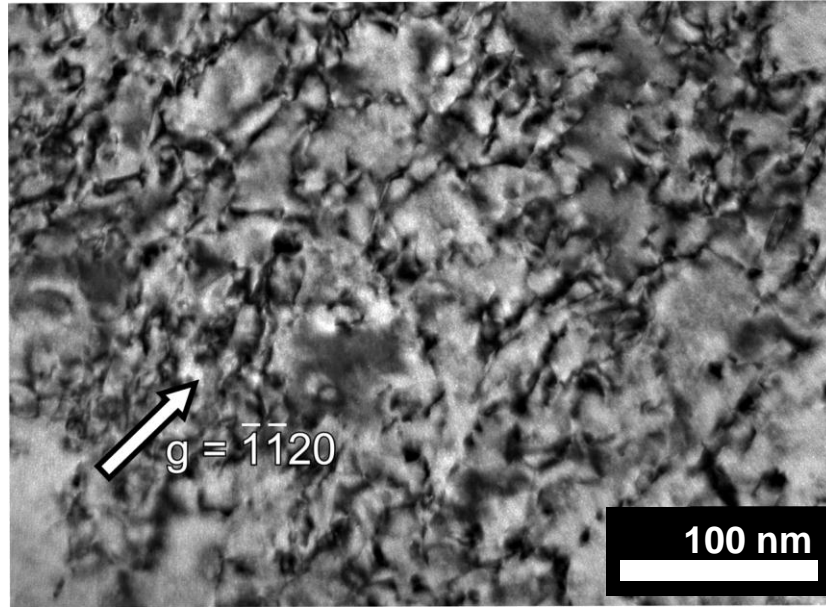


Figure 6.5. Bright field TEM micrograph of fine slip lines in the α -phase of Ti-4.3V. Slip is $\langle a \rangle$ type dislocations on prism planes. The dislocations are of the type $\mathbf{b} = 1/3\langle 11\bar{2}0 \rangle$.

In contrast to the creep deformation mechanisms of the fine equiaxed microstructure, coarse deformation features were present in creep tested samples of Ti-4.3V with Widmanstätten microstructure. Figure 6.6 shows SEM micrographs taken prior to and following creep deformation of Ti-4.3V with a Widmanstätten microstructure. Notice the coarse deformation products that traverse over the phase boundaries of the α and β phases. TEM analysis of these deformation products reveals them to be twins or coarse slip in the α phase, and SIM (α') in the β phase. In addition, the linking of SIM and twins obviously is a result of the Burgers orientation relationship between the two phases of the Widmanstätten microstructure; as the platelet thickness is similar to the equiaxed microstructure tested. This orientation relationship and additional deformation mechanism are responsible for the increased creep strain in the Widmanstätten alloy.

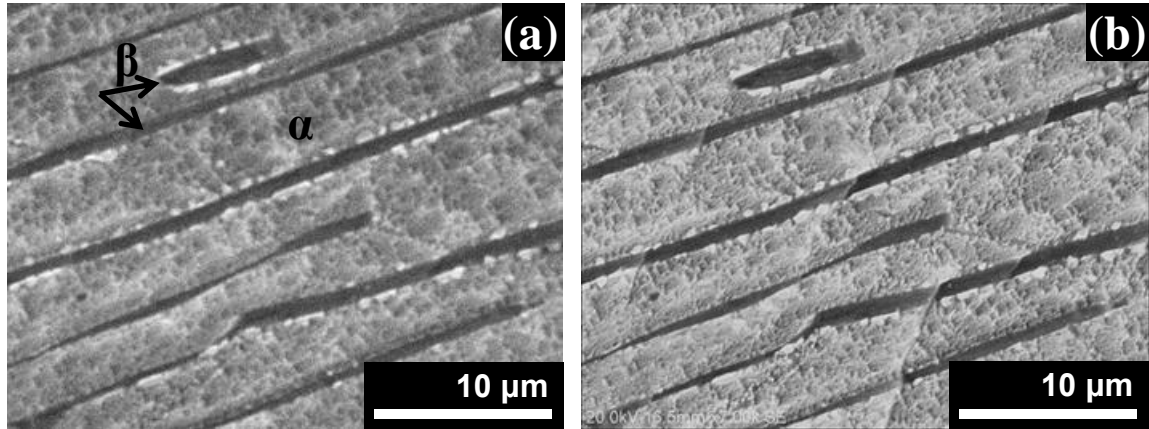


Figure 6.6. SEM micrographs of $\alpha + \beta$ Ti-4.3V with Widmanstätten microstructure (a) before and (b) after creep testing at 95% YS for 200 hours to 0.90% total plastic strain. Note the coarse deformation features spanning multiple α (light) and β (dark) grains. These were identified during this study as stress induced martensite in the β phase and coarse slip or twinning in the α phase.

Figure 6.7 is an SEM micrograph of coarse deformation products spanning many grains in the Ti-4.3V alloy. Due to the Burgers orientation relationship between the α and β phases, the coarse slip planes of one phase are closely aligned with the coarse slip planes of the other phase. This will be discussed later. Figure 6.8 shows a TEM image of the coarse slip bands in α which appeared to be twins in earlier SEM investigations. These slip bands can also occur in tandem with stress induced martensite plates in the β phase. Figure 6.9 shows a TEM image of an example of the stress induced martensite in β linked with twinning in α present in the creep tested Ti-4.3 V. The common zone axis for the diffraction patterns was $[1\bar{2}10]_{\alpha} // [1\bar{1}1]_{\beta}$. The martensite plate was in a plane such that specific identification was not possible; however, it is known that there is a Burgers orientation relationship between the β and α' , namely $[111](11\bar{2})_{\beta} // [2\bar{1}\bar{1}3](\bar{2}112)_{\alpha'}$ or $[111](101)_{\beta} // [2\bar{1}\bar{1}3](1011)_{\alpha'}$ and the specific orientation with respect to the grain will be dependent upon both the grain orientation as well as the loading axis. The twin has been

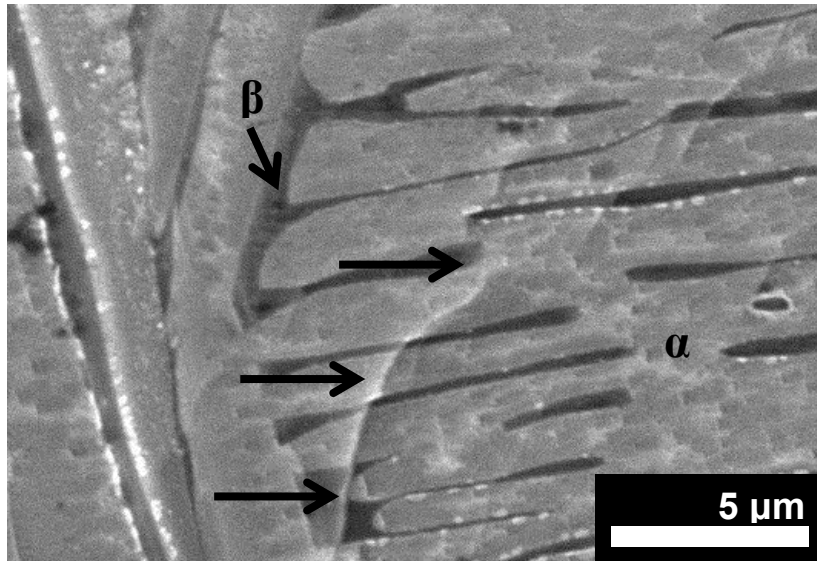


Figure 6.7. SEM micrograph of $\alpha + \beta$ Ti-4.3V with Widmanstätten microstructure creep tested to 0.90% total plastic strain. Note the coarse deformation features spanning the α (light) and β (dark) phases. These features were identified as coarse slip and twinning in the α phase and stress induced martensite (α') in the β phase.

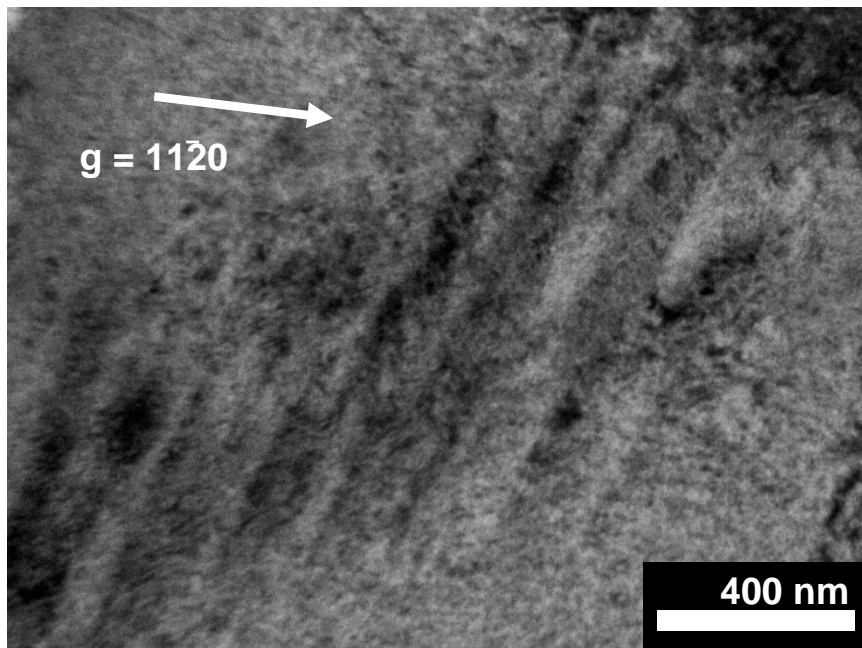


Figure 6.8. TEM bright field micrograph of slip bands in the β phase of $\alpha + \beta$ Ti-4.3V with Widmanstätten microstructure.

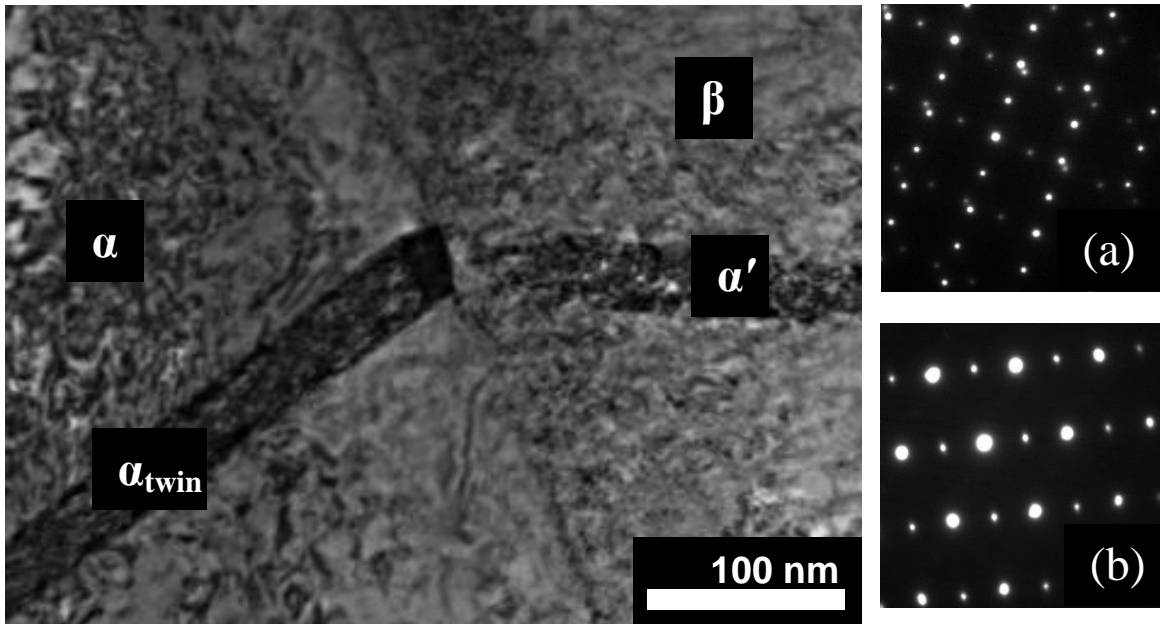


Figure 6.9. TEM bright field micrograph showing a hexagonal martensite plate (α') in the β phase connected to a $\{10\bar{1}2\}$ type twin in the α phase in creep tested Ti-4.3V with Widmanstätten microstructure. The twin was classified specifically as $(\bar{1}012)[10\bar{1}1]$. Accompanying diffraction patterns are from the (a) α /twin interface and (b) the α'/β interface. Zone axis is $[1\bar{2}10]_{\alpha} // [1\bar{1}1]_{\beta}$.

characterized as a $\{10\bar{1}2\}\langle\bar{1}011\rangle$ type twin. Figure 6.10 shows a TEM image of three martensite plates forming in two different orientations within a single β grain. Each martensite plate obeys the Burgers orientation relationship with the β phase as demonstrated by the diffraction patterns. Even though there wasn't a twin present in the α phase to add additional stresses, the interphase interfacial stresses were enough to form α' in the β phase. This will be addressed later. The interface of the α phase and the stress induced hexagonal martensite plates should be coherent with a twin-like interface, specifically a $\{10\bar{1}1\}$ near-twin relationship. The coherency of this interface has been confirmed by Jaworski and Ankem [22].

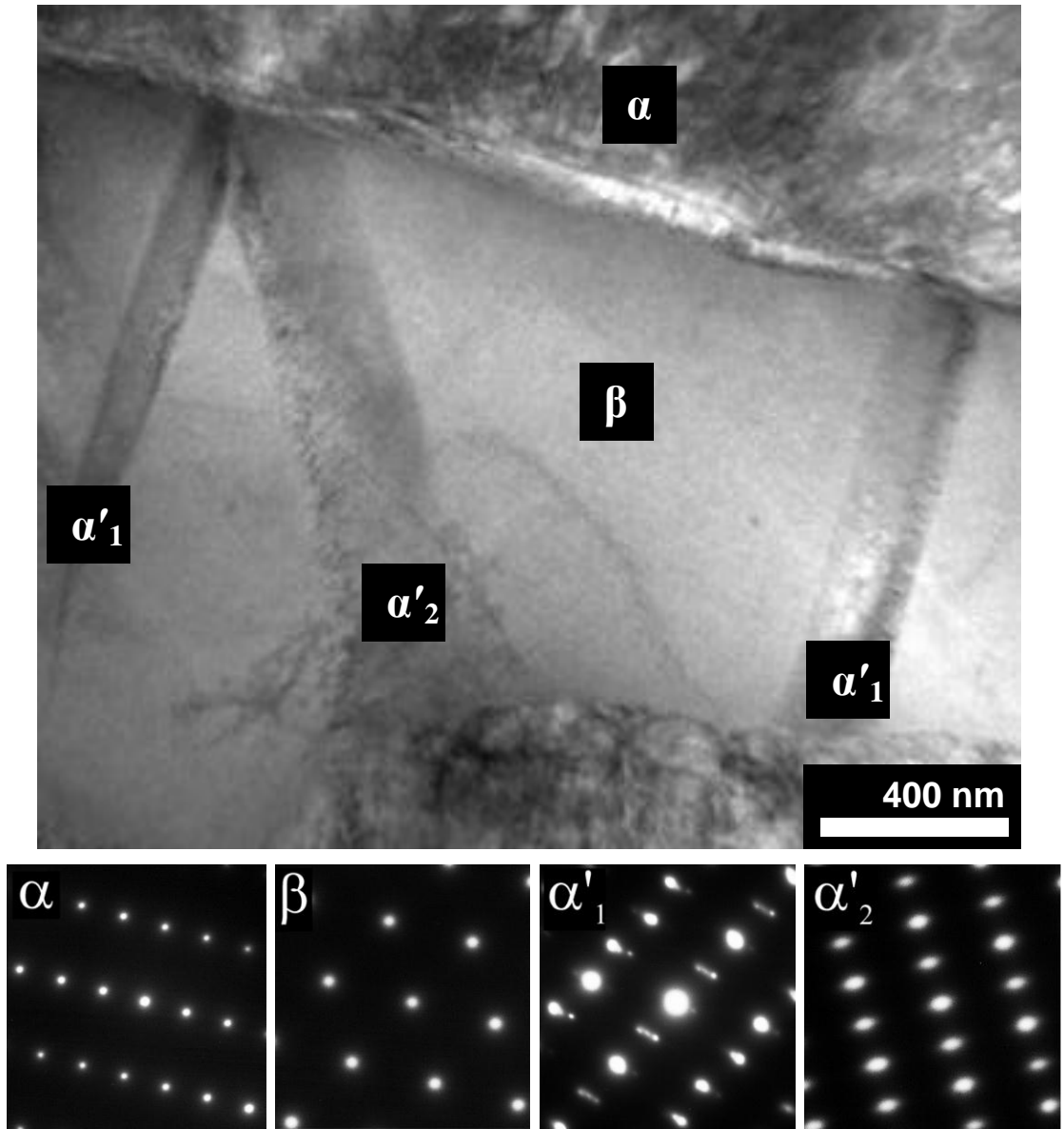


Figure 6.10. Bright field TEM micrograph showing the stress induced hexagonal martensite plates (α') within the β phase of Ti-4.3V creep tested at 95% YS for 200 hours. Accompanying diffraction patterns show that both planes have a near $\{10\bar{1}1\}$ twin relationship to the α phase. The zone axis is $[1\bar{1}1]_{\beta} // [1\bar{2}10]_{\alpha'}$.

6.2.3. Two-phase $\alpha + \beta$ Ti-8.1V alloy

The tensile true stress/true strain curves for the fine-grained equiaxed and Widmanstätten microstructure alloys are shown in Figure 6.11. The fine-grained alloy exhibits a slightly higher ultimate tensile strength, as well as a higher elastic modulus and yield strength. The Widmanstätten alloy exhibits a 95% YS of approximately 599 MPa. The fine-equiaxed alloy exhibits a 95% YS of approximately 684 MPa. Both alloys exhibit no strain hardening. These characteristics are due to the added β phase present in these alloys (50% vs. 20% in Ti-4.3V).

The creep curves for the Ti-8.1V fine grained and Widmanstätten alloys are shown in Figure 6.12. The alloys were tested at 95% of their respective YS. A clip on extensometer was used to record strain. SEM micrographs were taken prior to and during

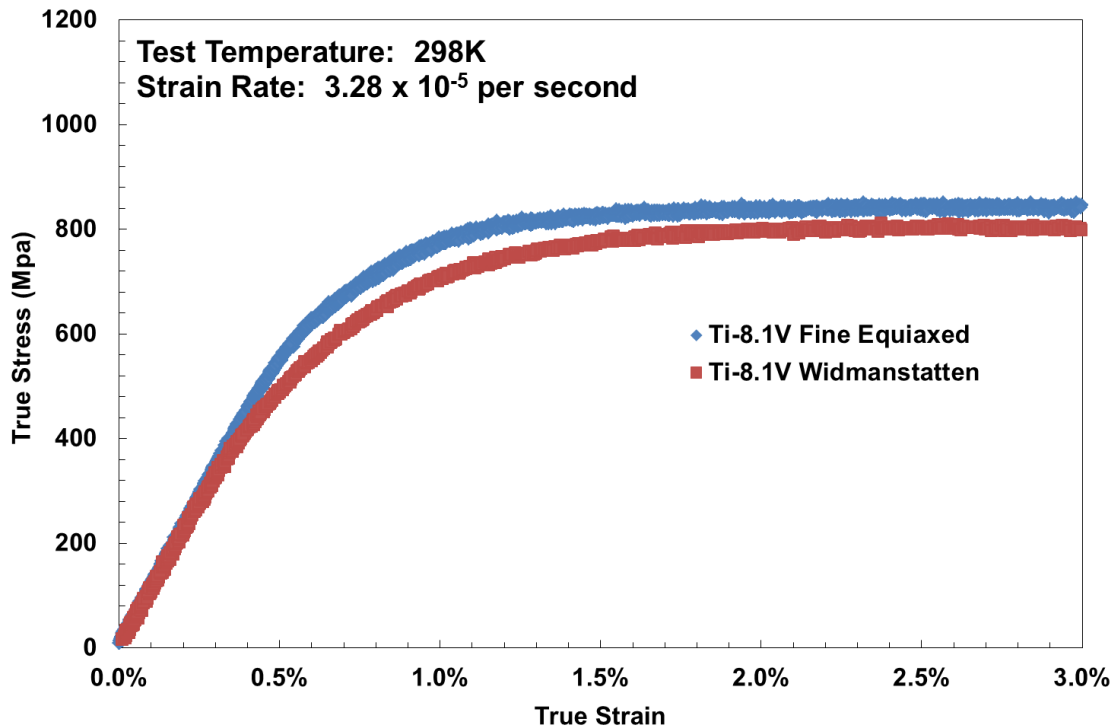


Figure 6.11. Tensile curves of Ti-8.1wt% V, tested at a strain rate of 3.28×10^{-5} /s to a 3% total strain.

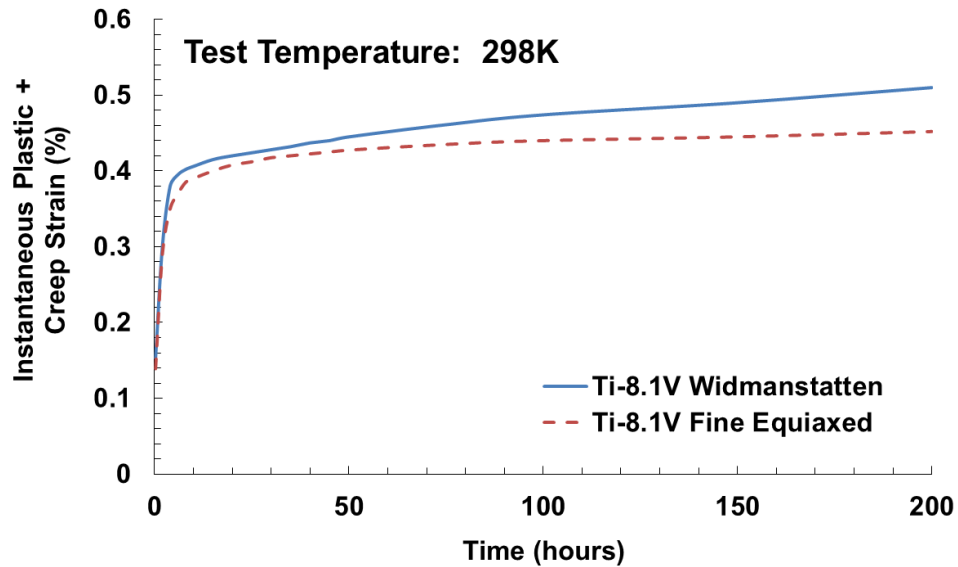


Figure 6.12. Creep curves of Ti-8.1V alloys, creep tested at ambient temperature at 95% of their respective YS.

testing in the same area of each specimen to record deformation mechanism. The Ti-8.1V alloy with a Widmanstätten microstructure exhibits a greater creep strain (~0.27%) than does the fine equiaxed microstructure (~0.22%). The creep strain for the Widmanstätten microstructure is approximately 13% greater than the equiaxed microstructure when the instantaneous plastic deformation of ~0.25% (Widmanstätten) and 0.18% (fine equiaxed) is subtracted from the total strain of each alloy. Additionally, from the creep curves it is apparent that the fine equiaxed alloy experiences creep exhaustion where the Widmanstätten alloy continues to strain. The lack of creep exhaustion suggests that the creep deformation mechanisms operating are increasing the internal stresses on other slip systems, resulting in further deformation. This will be addressed in the next section. The difference in creep deformation between the two microstructures is quite large and this difference is attributed to the difference in operating creep deformation mechanisms.

6.2.3.1. Creep deformation mechanisms

There were many deformation mechanisms observed during creep deformation of Ti-8.1V with a fine equiaxed microstructure. There was fine slip, coarse slip, and rare twinning in the α phase, as well as coarse slip and stress induced martensite in the β phase. Figure 6.13 shows SEM micrographs taken before and after creep deformation of Ti-8.1V with a fine equiaxed microstructure. Note the coarse deformation products in the β phase which were not present in the Ti-4.3V alloy. Figure 6.14 shows SEM micrographs taken from a different area which show stress induced martensite as well as coarse slip in the β phase. Also note that unlike Widmanstätten microstructures, the features do not cross phase boundaries. TEM investigations were unable to locate coarse any coarse slip in the β phase of this alloy; however, both twinning and stress induced martensite can be ruled out as possible features because of the wavy behavior of the features. Previous investigations determined that the β phase slips by edge dislocations along $\mathbf{b} = 1/2\langle 111 \rangle$. TEM investigations also demonstrated that stress induced martensite could occur in a non-Widmanstätten microstructured alloy, as shown in Figure 6.15, suggesting that additional factors come into play other than the templating effect. Even though the Ti-8.1V alloy with equiaxed microstructure experienced less total creep strain than the Ti-4.3V alloy with equiaxed microstructure, there is still coarse deformation features in the β phase suggesting that interaction stresses are responsible for the coarse features rather than the amount of strain, and partly due to the fact that the β phase is now the primary phase in Ti-8.1V. Even at very low strains, the single phase β alloy exhibited coarse deformation features during creep; suggesting that the coarse deformation features seen here are not as surprising as one first thinks.

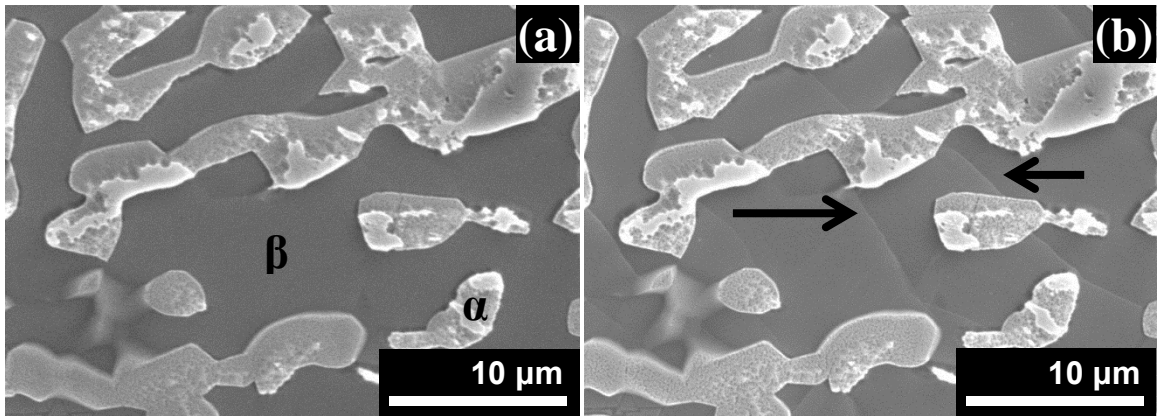


Figure 6.13. SEM micrographs of $\alpha + \beta$ Ti-8.1V (a) before and (b) after creep deformation at 95% YS for 200 hours to 0.41% total plastic strain. Note the coarse deformation features in the β phase (dark). These features were identified to be coarse slip and stress induced martensite. Fine slip has been noted in the α phase (light) due to an increase in the fiducial line spacing during testing. Note that deformation features do not cross phase boundaries.

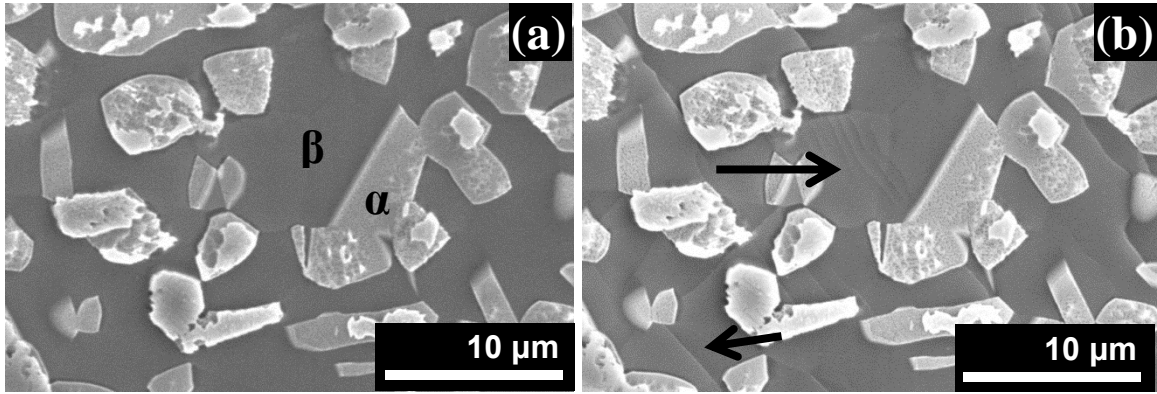


Figure 6.14. SEM micrographs of $\alpha + \beta$ Ti-8.1V (a) before and (b) after creep deformation at 95% YS for 200 hours to 0.41% total plastic strain. Note the coarse deformation features in the β phase (dark). These features were identified to be coarse slip and stress induced martensite. Fine slip has been noted in the α phase (light) due to an increase in the fiducial line spacing during testing. Twinning in the α phase was also noted, but was rare.

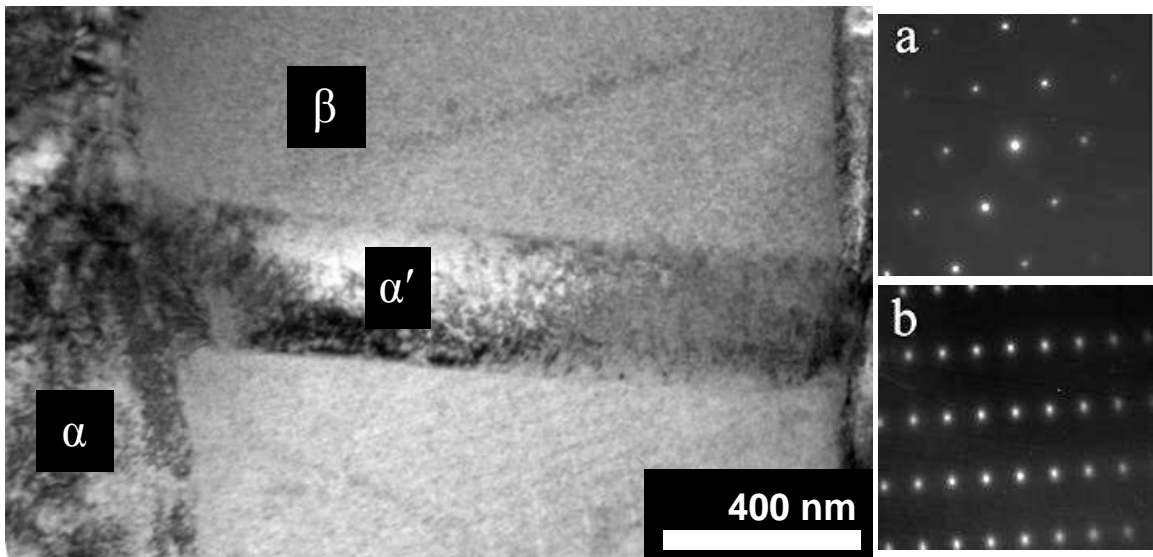


Figure 6.15. Bright field TEM micrograph of stress induced hexagonal martensite (α') plate in the β phase of Ti-8.1V with equiaxed microstructure. To the right are selected area diffraction patterns taken from the (a) β phase and (b) α' plate. The zone axis is $[1\bar{1}1]_{\beta} // [1\bar{2}10]_{\alpha}$.

In contrast to the creep deformation mechanisms of the fine equiaxed microstructure, the coarse deformation features in the Widmanstätten microstructure were much more plentiful and crossed many grains as seen before in the Ti-4.3V alloy. Figure 6.16 shows the before and after SEM micrographs of a Ti-8.1V alloy with Widmanstätten microstructure creep tested at 95% YS for 200 hours. Note the coarse deformation features spanning many grains. TEM analysis of these features reveals them to be twins or coarse slip in the α phase and stress induced martensite (α') in the β phase. These results are consistent with previous research [21, 22]. It should be noted that this linking of α' and twins is due to the Burgers orientation relationship which exists in Widmanstätten microstructured alloys. This resulting additional deformation is responsible for the increase in creep strain experienced by this alloy.

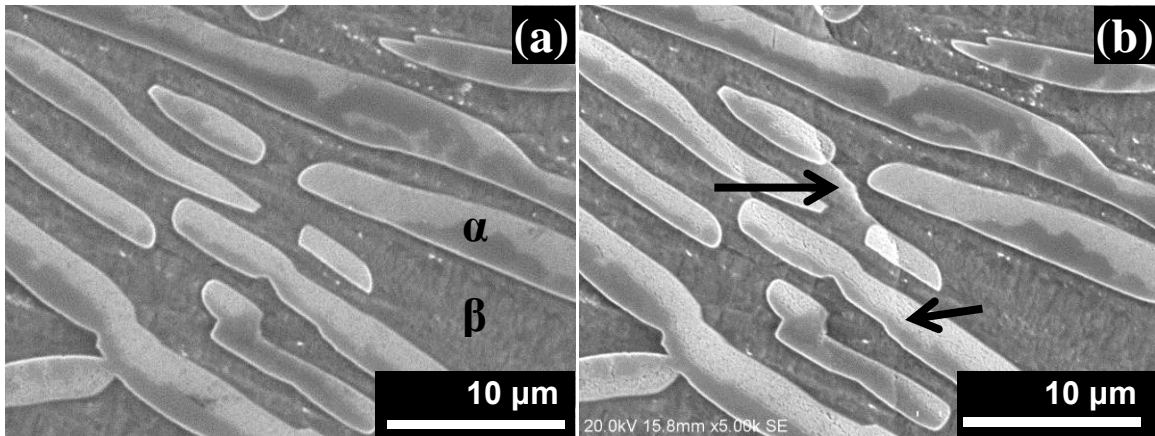


Figure 6.16. SEM micrographs of $\alpha + \beta$ Ti-8.1V with Widmanstätten microstructure (a) before and (b) after creep testing at 95% YS for 200 hours to 0.52% total plastic strain. Note the coarse deformation features spanning many grains. These features were identified to be twinning or coarse slip in the α phase (light) and stress induced martensite in the β phase (dark).

Figure 6.17 is a TEM micrograph from Jaworski and Ankem showing the relationship between twinning and stress induced martensite over the span of many grains in a Widmanstätten Ti8.1V alloy creep tested at 95% YS [22]. The same alloy and microstructure was also tested during this investigation to verify previous results as well as verify the methodologies for testing, SEM characterization, and TEM characterization used here. The results were perfectly replicated.

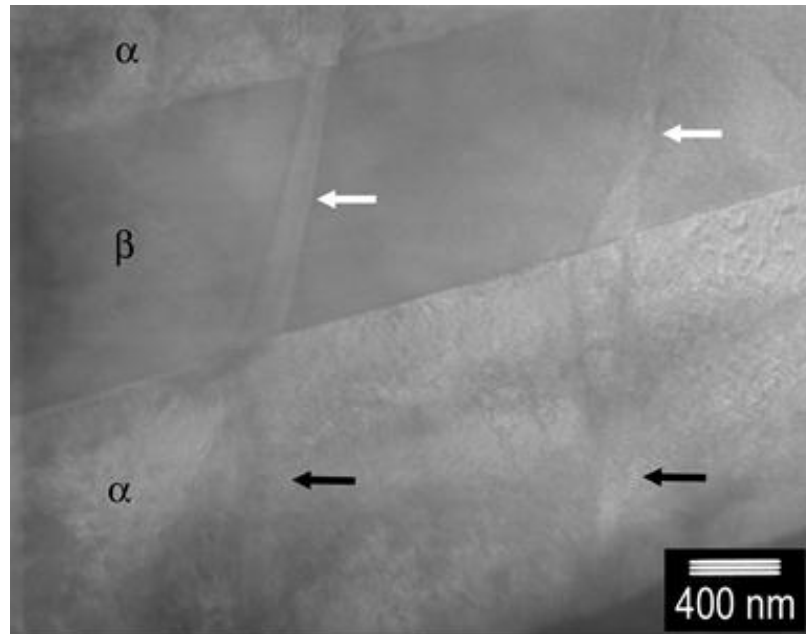


Figure 6.17. Bright field TEM micrograph showing stress induced martensite plates in the β phase and twins in the α phase of Ti-8.1V with Widmanstätten microstructure. The martensite plates and twins alternate across the width of the β and α grains [22].

6.2.4. Two-phase $\alpha + \beta$ Ti-12.6V alloy

The tensile true stress/true strain curves for the fine equiaxed grained and Widmanstätten microstructure alloys are shown in Figure 6.18. The two alloys exhibit almost exactly the same tensile behavior. The 95% YS for both alloys is approximately 760 MPa. The ultimate tensile strength at 3% elongation for the fine-equiaxed microstructure is only 5% greater than the Widmanstätten alloy. Neither alloy shows strain hardening behavior. It should be noted that even though the UTS of the Ti-12.6V alloy is approximately equal to the Ti-8.1V alloy, the 95% YS of the higher β phase content alloys is significantly higher. Conceptually, this makes sense because both of these alloys have the β phase as the primary phase so the tensile behavior should be strongly dictated by that phase.

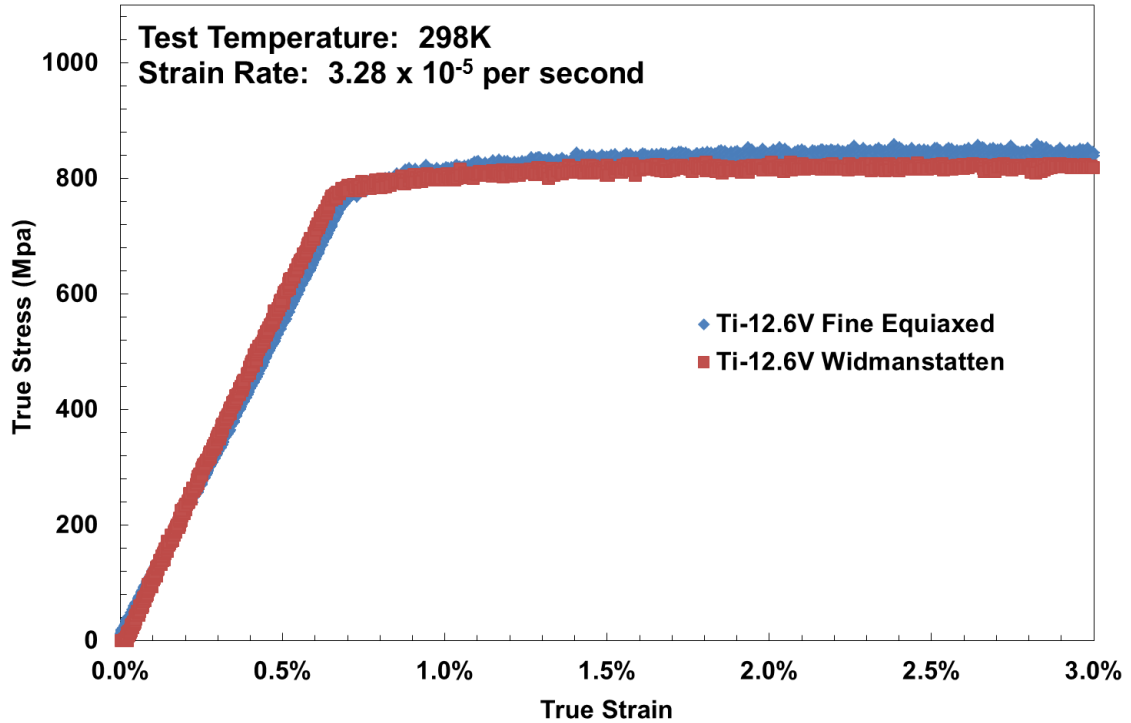


Figure 6.18. Tensile curves of Ti-12.6wt% V, tested at a strain rate of 3.28×10^{-5} /s to a 3% total strain.

The creep curves for the Ti-12.6V alloys are shown in Figure 6.19. The alloys were tested for 200 hours at 95% of their respective YS. A clip on extensometer was used to record strain. SEM micrographs were used to record the same area of the specimen before, during, and after testing. Both alloys demonstrate almost identical creep deformation behavior. The alloys creep strain was about 0.10% 0.12% respectively, after 200 hours of testing. For reference, the single-phase β -Ti-14.8V alloy of a similar grain size crept to $\sim 0.02\%$ strain. The difference in creep strain after $\sim 0.055\%$ (instantaneous plastic strain) is subtracted from the total strain is about 16%. This demonstrates that even though both alloys appear to exhibit creep exhaustion and have very similar creep curves the difference between the two is still on par with the difference seen at the other compositions.

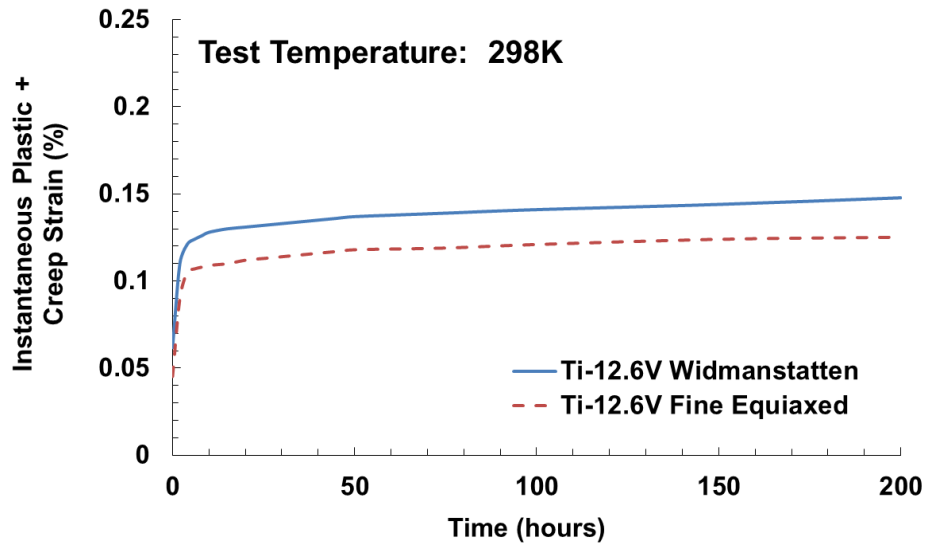


Figure 6.19. Creep curves of Ti-12.6V alloys, creep tested at ambient temperature at 95% of their respective YS.

6.2.4.1. Creep deformation mechanisms

Creep deformation in Ti-12.6V with fine equiaxed microstructure is primarily due to fine slip in the α phase and $\{332\}\langle 113\rangle$ twinning with $\mathbf{b} = 1/2\langle 111\rangle$ slip in the β phase. Figure 6.20 shows SEM micrographs taken before and after creep testing at 95% YS. Note the stress induced plates similar to the previous investigations; however, TEM analysis revealed these plates to be $\{332\}\langle 113\rangle$ twinning rather than stress induced martensite (SIM) as shown in Figure 6.21. The zone axis is $(110)_{\beta}$. It should also be noted that with the fine equiaxed microstructure, coarse deformation features do not cross phase boundaries. This is demonstrated quite drastically by Figure 6.22. In Figure 6.22, there is a very large twin as well as extensive slip in the β phase around an α phase particle, yet the α particle shows no signs of twinning or coarse slip, suggesting that the interaction stresses from α on to β act more strongly than those from β onto α .

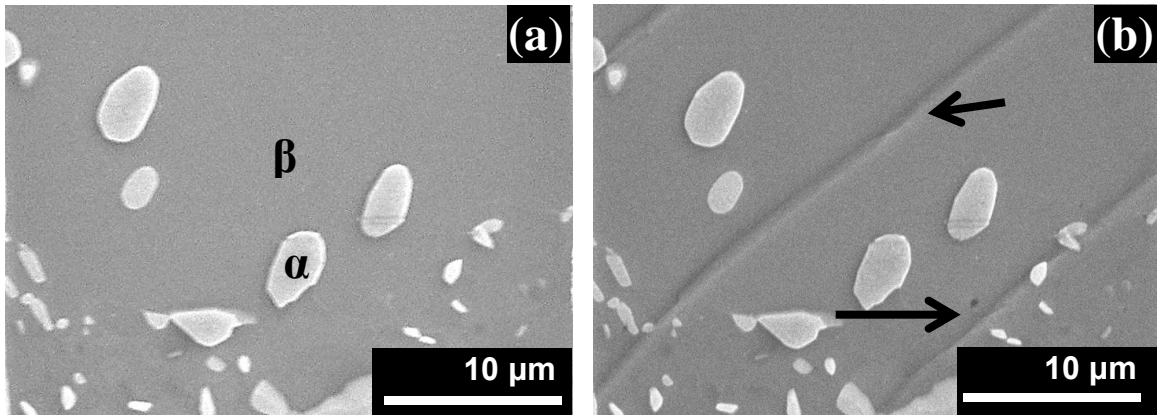


Figure 6.20. SEM micrographs of $\alpha + \beta$ Ti-12.6V (a) before and (b) after creep deformation at 95% YS for 200 hours to 0.11% total plastic strain. Note the stress induced plates (SIP) in the β phase (dark) and lack of coarse deformation features in the α phase (light).

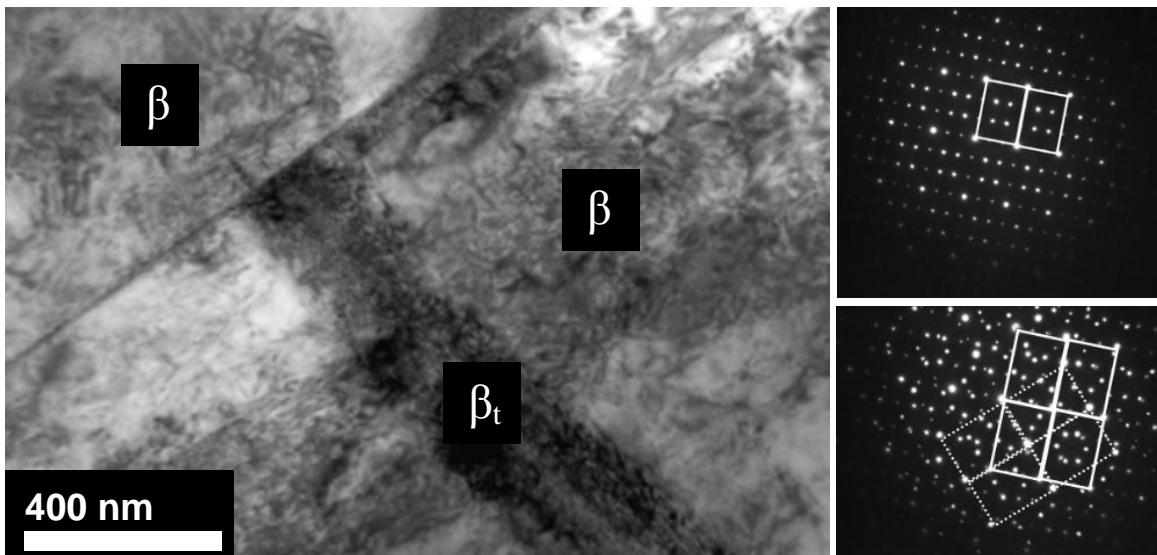


Figure 6.21. TEM micrograph and diffraction pattern of $\alpha + \beta$ Ti-12.6V showing stress induced plate which is $\{323\}[131]$ twin. The additional spots are from the ω phase and double diffraction.

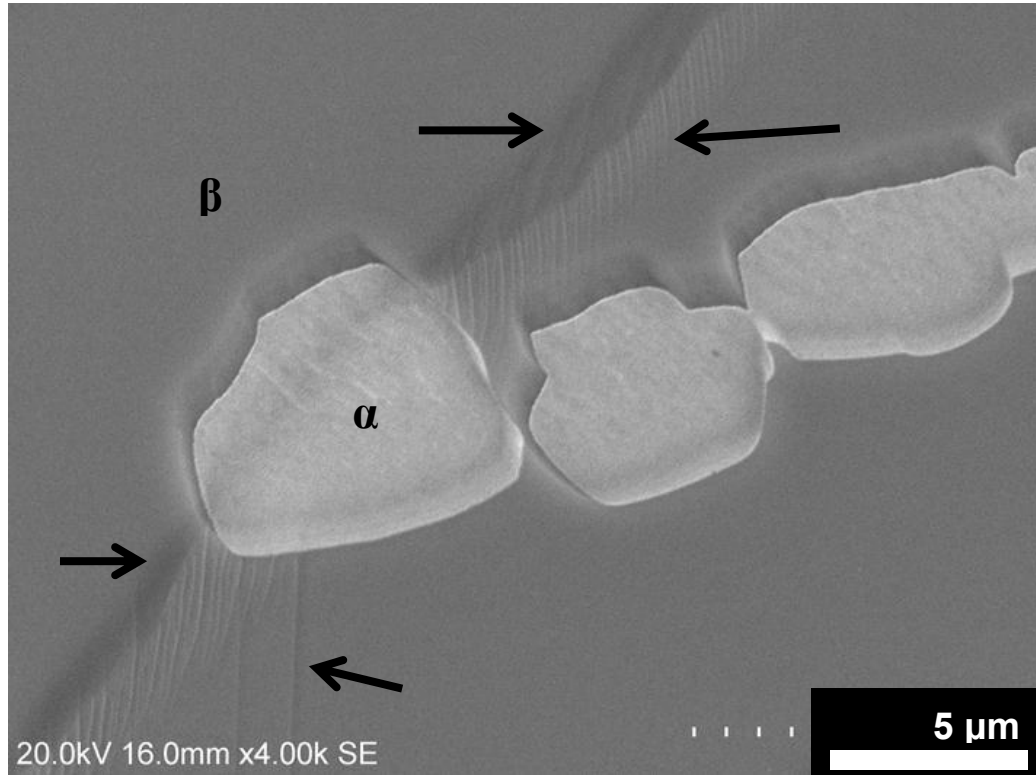


Figure 6.22. SEM micrograph of $\alpha + \beta$ Ti-12.6V after creep deformation at 95% YS for 200 hours to 0.11% total plastic strain. Note the stress induced plates (SIP) and coarse slip in the β phase (dark) and lack of coarse deformation features in the α phase (light). The SIP are $\{332\}\langle 113\rangle$ twins.

The creep deformation mechanisms of the Widmanstätten microstructured Ti-12.6V alloy included fine slip and twinning in the α phase as well as twinning in the β phase. Figure 6.23 shows SEM micrographs taken before and after creep deformation. With the presence of a Burgers relationship between the two phases, coarse deformation products can traverse phase boundaries. It is expected that the Burgers orientation relationship will also act as a template for stress induced martensite in the β phase; however, Figure 6.24 shows that the coarse features observed are twins just as with the equiaxed microstructure. The slight difference in creep strain observed between these two alloys is attributed to the deformation twinning observed in the α phase.

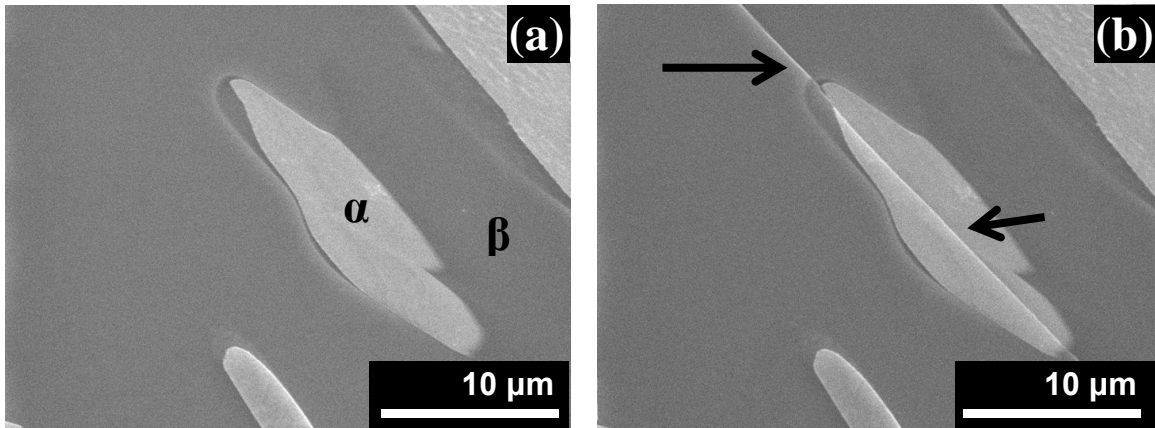


Figure 6.23. SEM micrographs of $\alpha + \beta$ Ti-12.6V (a) before and (b) after creep deformation at 95% YS for 200 hours to 0.12% total plastic strain. Note the stress induced plates (SIP) in the β phase (dark) connected to deformation twinning in the α phase (light).

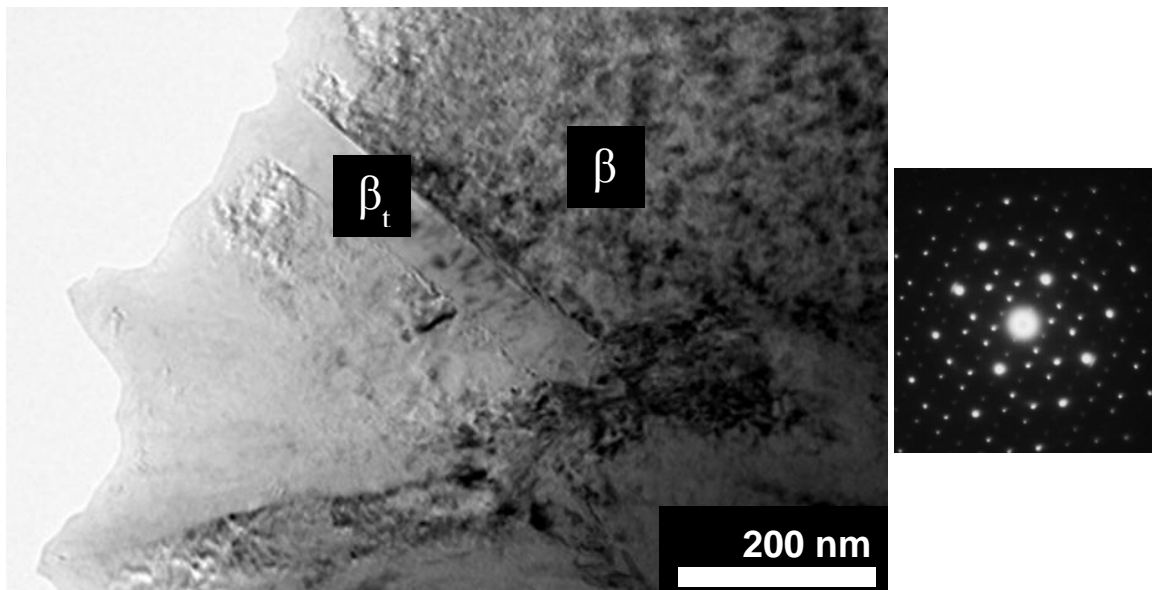


Figure 6.24. TEM micrograph of $\alpha + \beta$ Ti-12.6V alloy with Widmanstätten microstructure with $\{332\}\langle 113\rangle$ twinning. Alloy was creep tested at 95% YS for 200 hours. Diffraction pattern was taken from inside the twin. Zone axis is $\langle 110\rangle$.

Figure 6.25 shows another area of the Ti-12.6V alloy with Widmanstätten microstructure after creep testing. In this case, even with the Burgers orientation relationship, only one of the two coarse deformation products were able to cross the phase boundary. The reasons for this are discussed in the next section. As mentioned before because twinning is the operating deformation mechanism in the β phase, the aligned slip systems between α and β may not favor easy cross-slip as if the β phase had transformed to martensite. As such, the direction of a twin may be more important for it to resolve shear stresses onto the appropriate twinning planes in α .

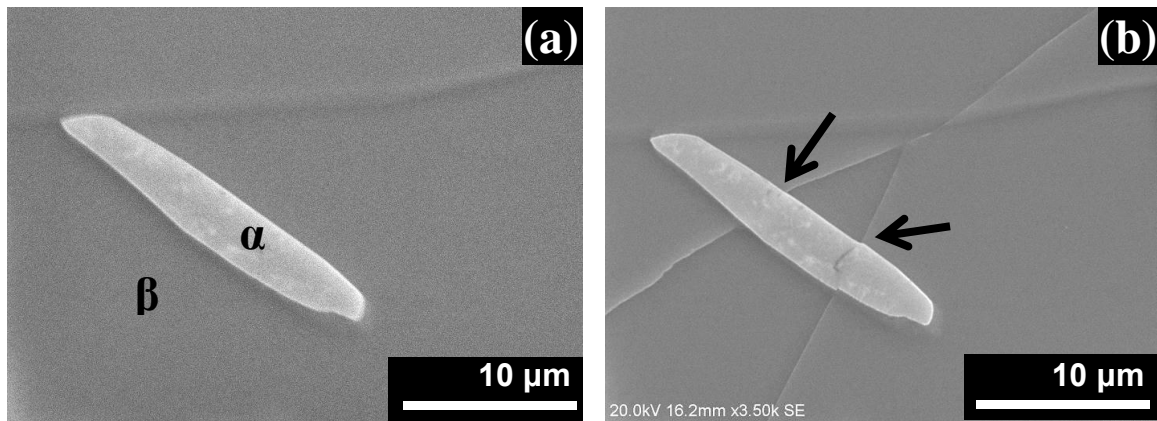


Figure 6.25. SEM micrographs of $\alpha + \beta$ Ti-12.6V (a) before and (b) after creep deformation at 95% YS for 200 hours to 0.12% total plastic strain. Note the stress induced plates (SIP) in the β phase (dark) connected to deformation twinning in the α phase (light) and no visible deformation in the α phase.

6.3. Discussion

6.3.1. Contribution of deformation mechanisms to creep strain

For an equivalent lath thickness the Widmanstätten microstructure had a higher creep strain for all alloys tested over the same time period. Figures 6.26, 6.27, and 6.28 show the relationships between creep deformation behavior and microstructure. As evidenced, these relationships follow general self-consistent trends. This additional creep strain can be explained by a difference in deformation mechanisms, namely coarse deformation products in the β phase such as stress induced martensite and twinning and the ability of these deformation products to trigger additional coarse deformation products in adjacent phases due to the Burgers orientation relationship that exists in a Widmanstätten microstructured alloy. An understanding of these creep deformation mechanisms is essential in order to design and process alloys for reduced creep strain.

6.3.2. The special importance of interaction stresses during creep deformation

Interaction stresses between the α and β phases are responsible for the deformation mechanisms of the two-phase alloys, which differ from those of the single-phase alloys that constitute the individual phases. Specimens examined in this study were creep tested at a constant 95% of their respective YS values. Any additional stresses required to initiate creep processes must be from internal sources. Therefore, internal stresses due to interactions between the α and β phases are even more important during creep deformation at low stresses compared to tensile deformation. There are several interaction stresses between the α and β phases that must be considered. These interactions are discussed, along with their consequences, below.

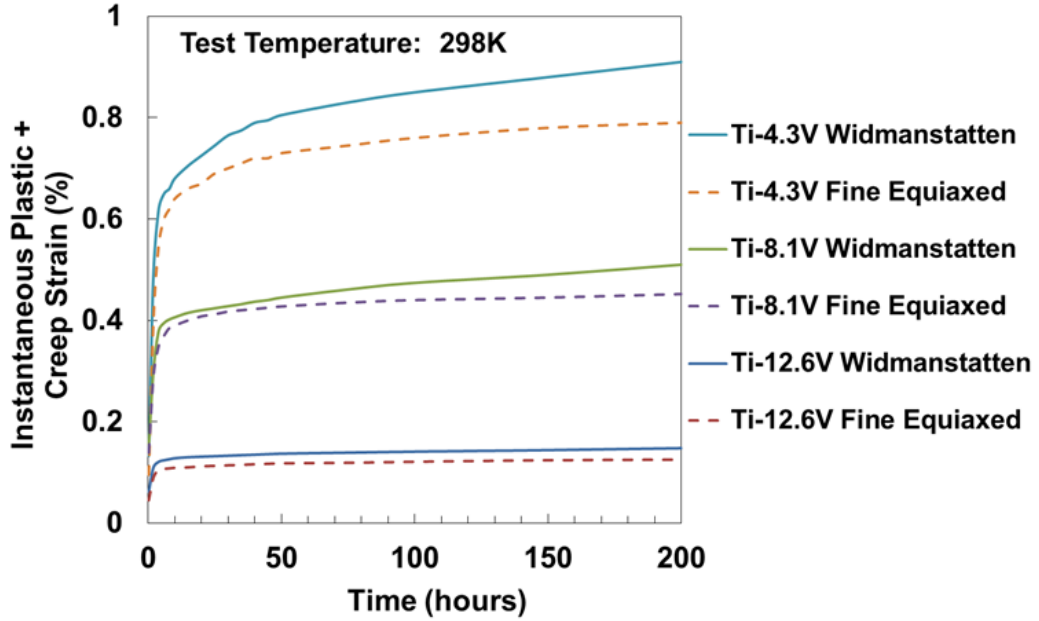


Figure 6.26. Composite graph of the creep curves of the two different microstructures for the three different alloys. As shown, the effect of microstructure decreases with increasing volume fraction of β phase.

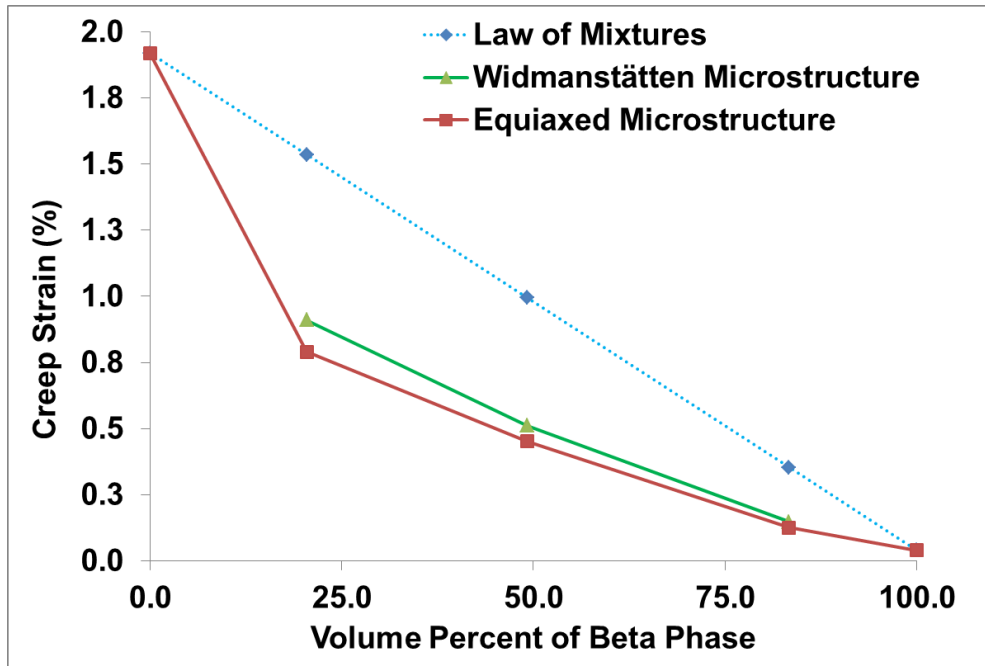


Figure 6.27. Graph showing the relationship between creep strain of the alloys compared with what the law of mixtures would predict. As shown, the β phase exerts a much stronger influence on alloy behavior than predicted.

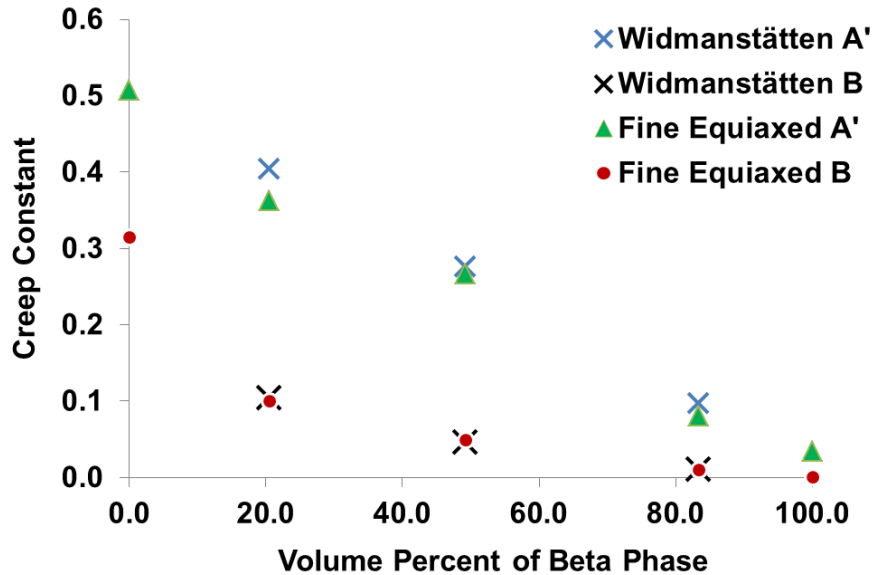


Figure 6.28. A graph of the creep constants from the equation $\epsilon = A' + B \ln(t)$ for each of the tests during this investigation. As shown, the constants do follow general self-consistent trends.

6.3.2.1. Elastic interaction stresses

As the creep specimens are loaded to 95% of their respective yield stresses, there is an instantaneous elastic strain. These stresses initially increase stress in the α phase, contributing to the formation of twins and high dislocation densities in narrow grains, even at the relatively low applied creep stress. After significant α phase deformation, elasto-plastic interaction stresses can act on the β phase, contributing to stress induced martensite nucleation or twinning. Widmanstätten platelets occur in colonies of similarly oriented grains. As soon as twin or SIM plate forms, the cascading effect can travel the entire width of the colony. In the case of equiaxed microstructures, there can still exist a Burgers orientation relationship between the phases; however, it is very unlikely that the neighboring grain will be able to accommodate the deformation along the original plane. It is suggested that this is the primary reason behind the increased creep strain of the Widmanstätten microstructure.

6.3.2.2. α phase as a template for stress induced hexagonal martensite

It is proposed that the presence of the α phase is responsible for the formation of hexagonal SIM instead of twins in the β phase of Ti-4.3V and Ti-8.1V. TEM analysis revealed a $\{10\bar{1}1\}$ twin relationship between martensite plates in the β phase and the adjacent α phase of creep deformed specimens. The identical crystal structure and the observed twin relationship between the α and α' makes the α phase an exceptional template for the nucleation of stress induced hexagonal martensite in the β phase in alloys with a Widmanstätten microstructure. There is no such orientation relationship or crystallographic similarity between the α phase and $\{332\}\langle 113\rangle$ twins in the β phase. Therefore the interface created between the α phase and the stress induced martensite plate is expected to be coherent, whereas the interface between $\{332\}\langle 113\rangle$ twins in β and the α phase would not be. SIM formation would be favored over twinning in β due to a lower misfit strain and decreased surface free energy for martensite formation.

6.3.2.3. $\{332\}\langle 113\rangle$ twinning in Ti-12.6V instead of SIM

In order for extensive twin nucleation and growth in the α phase, the β phase must strain to accommodate steadily increasing α phase strain. If the β phase constrains the α phase sufficiently, the formation and growth of twins will be retarded. This is evidenced in the current study. Widespread twinning occurs in the α phase of Ti-4.3V and Ti-8.1V, but rarely in Ti-12.6V. Because the volume fraction of the higher strength β phase is significantly more in Ti-12.6V, the β phase will accommodate more strain than for the other two alloys. If the α phase twinning is retarded enough, the chances that a specific α twin will be in the correct orientation to help nucleate SIM in an adjacent grain goes

down. In addition, the interfacial stresses decay quite rapidly away from the α/β interface. With less interfacial area, the probability for aligned shear systems goes down as well. Because formation of SIM becomes harder, the strain in the β phase will be accommodated by twinning. Additionally, the interaction stresses caused in the β phase by the α phase decay rapidly away from the phase interface. With a higher volume fraction of β phase present, the stresses exerted on the β phase would be less significant to overall resolved stresses.

6.4. Summary of creep deformation processes

The following sequence of events results in the creep deformation of the alloys in this investigation. When the specimens are first loaded to a stress equivalent to 95% of their yield stress, there is an instantaneous elastic deformation. Elastic interaction stresses are placed on the α phase. The combination of the applied stress and the elastic interaction stress causes slip and/or twinning in the α phase. Dislocations move slowly with time due to the relatively low applied stress, and begin to pile-up at the α/β interface. Time dependent twins can also form and grow, adding to the creep strain. As the α phase deforms plastically, interaction stresses are reduced on the α phase, and the β phase must deform or there must be interphase interface sliding in order to accommodate further α phase deformation.

After sufficient time, the shear stress from the dislocation pileup or twinning is sufficient to nucleate stress-induced martensite in the β phase of Ti-8.1V because of aligned shear systems in the α and β phases due to the Burgers orientation relationship. If the α phase was constrained enough that twinning could not occur, then time-dependent

twinning begins to occur in the β phase. When the martensite or twin spans the β phase, twinning or coarse slip in the adjacent α phase can be triggered. This is once again due to aligned shear systems in the α and β phases. This process can continue across many α and β grains due to the Burgers orientation relationship of α and β . Twinning in the α phase may be time dependent or instantaneous. The growth rate of martensite may also be may be instantaneous, controlled by the growth rate of twins or slip rate in the α phase, or the martensite may have an inherent time-dependent mechanism. Further study is warranted to explore these possibilities.

6.5. Conclusions

1. The creep strain of Ti-4.3wt% V, Ti-8.1wt% V, and Ti-12.6wt% V decreases with increasing volume fraction of the β phase when all alloys are tested at 95% of their respective yield stress. This is attributed to a difference in deformation mechanisms.
2. The amount of creep strain exhibited by each alloy does not obey the Law of Mixtures. The law of mixtures does not take into account interaction stresses. In the case of the alloys studied during this investigation, interaction stresses are very significant to creep deformation and creep deformation mechanisms.
3. The results seen during this investigation were contrary to the results seen during high temperature creep. Widmanstätten structured $\alpha + \beta$ alloys demonstrate excellent high temperature creep resistance due to the colonies of Burgers oriented plates which resist interface sliding. However, at low temperatures, these

same colonies transmit deformation mechanisms easily and contribute to increased creep strain.

4. Deformation mechanisms in equiaxed microstructures very rarely cross phase boundaries. This is attributed to the lack of a burgers orientation relationship which would otherwise align significant slip planes.
5. Formation of hexagonal SIM plates during creep deformation in the β phase of binary Ti-V alloys only occurs in the presence of α platelets. However, twinning occurs in the Ti-12.6V alloy, which has the same chemistry as the β phase of Ti-4.3V and Ti-8.1V. This is attributed to the greater constraints that the increase in volume fraction of β phase exerts on the α phase.
6. Twins in the α phase occurred in response to stress induced martensite in the β phase and vice versa. This is evidenced by TEM observations of twin-martensite pairings in Ti-4.3V and Ti-8.1V.
7. Interactions between phases are an extremely important consideration in creep deformation because they can be responsible for additional deformation mechanisms, resulting in increased creep strain. Understanding these interactions is important in the design and processing of two-phase alloys for improved creep resistance.

Chapter 7

Finite Element Studies of the Interactions Between α and β Phases in Two-Phase Ti Alloys

When materials consisting of two or more phases are deformed, where the phases have different elastic properties, elastic interaction stresses will develop to maintain compatibility at the interfaces [26, 157, 158]. These interaction stresses can occur during all types of deformation including tensile, creep, and fatigue. These elastic interaction stresses are significant because, depending on the morphology of the multi-phase material, they can assist applied loads in initiating plastic deformation mechanisms even when the applied load resolved onto a slip system is below the critical value [26]. In a similar sense, they can also hinder applied loads. Ankem et al. [157, 159] have shown the role elastic interaction stresses play on the initiation of slip in two-phase materials. It has not been shown however how these interactions decay away from the interfaces, as well as the effect of morphology of phases on these interaction stresses.

Finite element modeling (FEM) can be a very powerful tool for analyzing material behavior and interaction stresses. FEM provides the ability to directly control material characteristics and geometry as well as the ability to read out simulation results from nearly any point in the model. In these investigations, 3D finite element modeling has been used to study the behavior of two-phase alloys. It is the goal of this work to understand the interfacial stresses, in particular the resolved shear stress on a various slip planes, as a function of applied stress. In particular, it will be the focus of this investigation to analyze the relationships between twin systems in α -Ti and

twin/martensite systems in β -Ti. A systematic study was undertaken to develop the methodology and process for using 3D finite element modeling to analyze elastic interaction stresses in two-phase materials. This was accomplished with the sequential modeling of a two-phase bi-crystal of $\alpha + \beta$ Ti to simulate the possible interactions between the two phases of a $\alpha + \beta$ Ti-V alloy. This simulation will incorporate the elements of 3D modeling, and material anisotropy; all important characteristics which will help to further the knowledge of this science. To achieve this simulation, the FEM tool ANSYS [160] will be used. Two-phase titanium alloys will be used as the model system in this investigation due to their current technological relevance; however, the findings of this investigation can be extended to many other two-phase systems.

7.1. Input properties and model development

The overall approach of this investigation will follow several sequential steps for various phase interaction scenarios and then compare those results to manually calculated techniques and also compare the results with the experimental results obtained in Chapter 6. The sequence for each model can be more simply broken down as: 1) determine geometry and orientation of the two-phase materials, 2) generate an FEM mesh, 3) perform the FEM calculations, and 4) graph and plot the results.

While using isotropic values of material properties can yield satisfactory results for certain simulations, the desire to understand interaction stresses between two phases, while including the effects of orientation, demands that anisotropic material properties are used. In particular, the stiffness or compliance matrix for each Ti phase must be used, rather than an aggregate Young's Modulus. Alpha titanium is a hexagonal close-packed

crystal structure with five independent elastic constants whereas β titanium is a cubic crystal structure with three independent elastic constants. The five elastic compliances for single crystals of pure α -Ti are $s_{11} = 0.9581$, $s_{12} = -0.4623$, $s_{13} = -0.1893$, $s_{33} = 0.6980$, and $s_{44} = 2.1410$ in units of 10^{-11} Pa^{-1} [161-163]. The three elastic compliances for single crystals of β -Ti (Ti-10wt% Cr) are $s_{11} = 1.8570$, $s_{12} = -0.7741$, and $s_{44} = 2.3420$ in units of 10^{-11} Pa^{-1} [157, 163]. These compliances refer to the principal crystallographic axes indicated by x_o , y_o , and z_o in the stereographic projection in Figure 7.1. Due to symmetry, the other components of the elastic constant tensor matrix may be found based on these values. The complete standard compliance tensors may be found in Appendix J. The relative orientation between the α and β phases is not arbitrary. In the case of a two-phase alloy with Widmanstätten microstructure, there is a Burgers orientation relationship between the two phases. Figure 7.1 also indicates this Burgers orientation relationship: $\langle 1\bar{2}10 \rangle (0001)_\alpha // \langle 1\bar{1}1 \rangle (110)_\beta$, as well as the interface plane $\{ \bar{5}140 \}_\alpha // \{ \bar{3}34 \}_\beta$ between α and β phases. The elastic constants in the standard orientations for the two phases must be transformed to the new primed coordinate system corresponding to the desired morphology while maintaining the Burgers orientation relationship and interface plane.

7.2. Coordinate system development

When considering an anisotropic material, the biggest deciding factor of material behavior is obviously orientation of that material. The α/β interface of titanium alloys has a very specific relationship and it is important to accurately portray this relationship during model development and execution. Hence, for the purpose of modeling, each

crystal structure or phase must be oriented such that the crystal directions and planes are aligned with not only each other (the relationship between phases) but also with the inherent Cartesian coordinate system used by ANSYS. For the purpose of modeling, the crystal structure's compliance tensor must be rotated such that it matches the chosen modeling coordinate system. This involves some work because α -titanium uses a 4 index hexagonal coordinate system and β -titanium uses a standard Cartesian coordinate system.

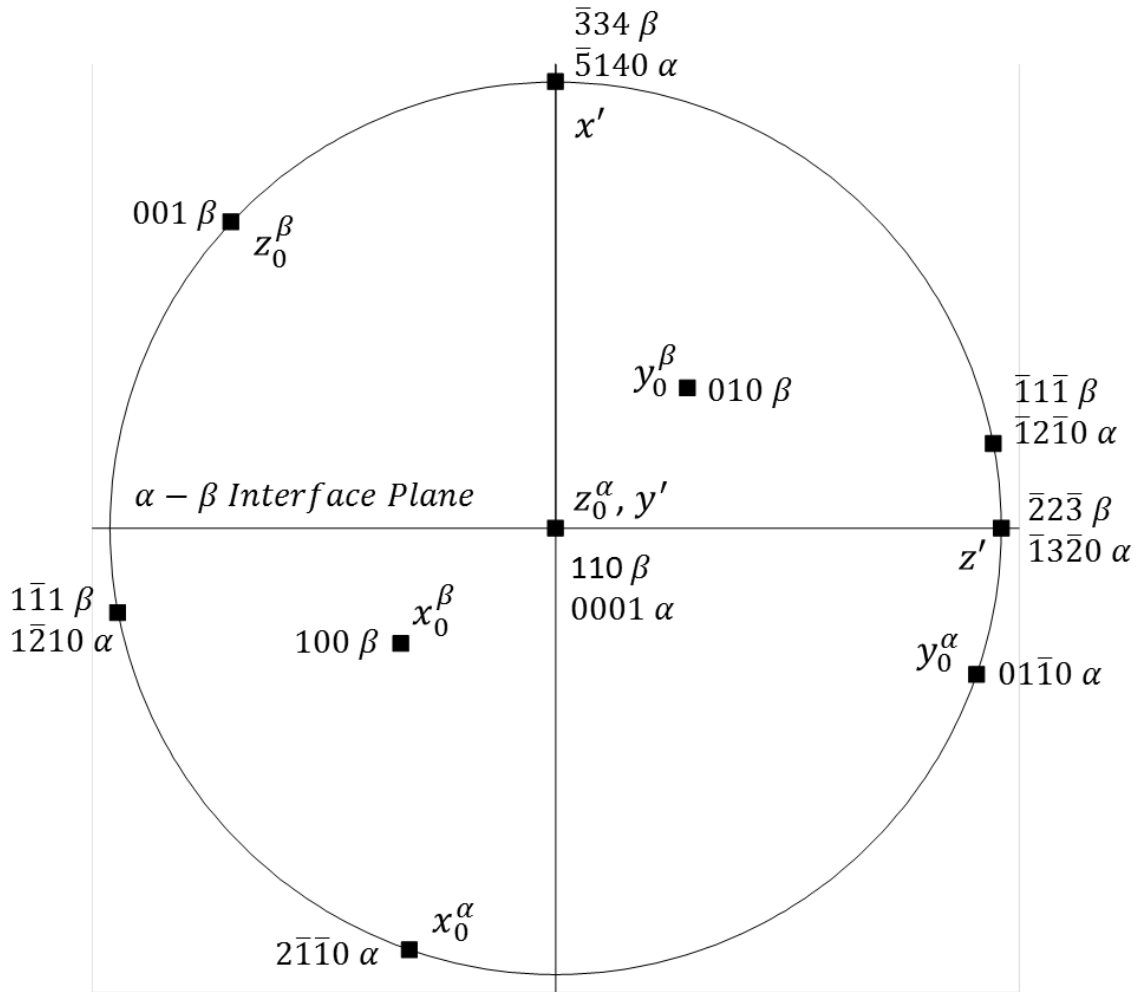


Figure 7.1. A stereographic projection showing the interface plane $(\bar{5}140)_{\beta} // (\bar{3}34)_{\alpha}$, Burgers orientation relationships $\langle 1\bar{2}10 \rangle (0001) // \langle 1\bar{1}1 \rangle (110)$, the standard crystallographic orientations and the prime coordinates (Widmanstätten orientation) for the FEM models in this investigation.

To rotate a tensor, one must first determine the direction cosines between the original coordinate system and the proposed coordinate system. The first goal of this project was to convert α -titanium's tensor (which is based on a hexagonal coordinate system of axes a_1 , a_2 , a_3 , and c) to a 90° Cartesian coordinate system with x , y , and z axes. To transfer the $\{hkil\}$ indices to a Cartesian coordinate system which is aligned with β -titanium, the following equations are used:

$$x = h - k * \sin(30^\circ) - i * \sin(30^\circ) \quad (7.1)$$

$$y = k * \cos(30^\circ) - i * \cos(30^\circ) \quad (7.2)$$

$$z = \sqrt{x^2 + y^2} * \frac{c}{a} * l \quad (7.3)$$

Other texts refer to the 90° hexagonal coordinate system as orthohexagonal with indices $\langle U^\circ V^\circ W^\circ \rangle \{H^\circ K^\circ L^\circ\}$. To convert from $\langle uvw \rangle \{hkil\}$ to this system, the following relationships have been established:

$$U^0 = \frac{3u}{2} \quad V^0 = \frac{u}{2} + v \quad W^0 = w$$

$$H^0 = h \quad K^0 = 2k + h \quad L^0 = l$$

Both methods yields the same results for indexing directions; however, when a 4 index coordinate system is converted to only 3 index the direction $[uvw]$ is no longer necessarily perpendicular to the plane (uvw) . For this reason if you are calculating the relationships between directions on a stereographic projection you must be sure to restrict yourself to Miller-Bravais indices.

From here, the rotation of the α or the β phase to line up with the other phase is accomplished by using a stereographic projection of the individual crystals from the appropriate perspective. A stereographic projection can be constructed which shows the relative positions of various planes. In Figure 7.1, the interface plane, original

coordinates, prime coordinates for the first FEM model, and Burgers orientation relationships are all shown. Using a Wulff net and techniques described by Greene & Ankem and Edington [54, 159], it is then possible to determine all of the direction cosines for the rotation of the two crystal structures to a common orientation. In addition, the direction of the applied load must also be considered such that the orientation maximizes resolved shear stresses on certain slip systems. The equations relating the original compliance tensors and the direction cosines are detailed in Appendix K [164]. The result will be a 6x6 symmetrical compliance tensor which is used in the succeeding sections to uniquely specify the anisotropic nature and orientation of the material property for each element of interest.

For the bi-crystal model, nodal solutions will be provided by ANSYS in terms of X, Y, and Z normal stresses as well as XY, YZ, and XZ shear stresses. Unfortunately, the stresses of interest are the shear stresses on various slip systems. To calculate these stresses, the resulting stress state of individual nodes will be rotated to other coordinates on the stereographic projection which correspond to a particular slip system. For this study, two tensor operations are necessary: rotating the original compliance matrices to match the test scenario orientation, and rotating the resulting normal stress and shear stress tensors to evaluate resolved shear stress on a specific slip plane. These tensor rotations can be accomplished using the relationship $T_{ij}' = a_{ik}a_{jl}T_{kl}$ where T' is the component of the rotated tensor, a is the respective component of the direction cosine matrix, and T is the component of the original tensor. This equation is written in the conventional dummy suffix notation and can be expanded accordingly [165].

7.3. Geometry of the two-phase system

To study the elastic interaction stresses between the α and β phases of a two-phase titanium alloy, the geometry of the systems to be investigated were carefully designed such that boundary conditions could be easily applied and the coordinate system would match the coordinates shown in the stereographic projection. The ANSYS procedure for constructing the bi-crystal model is shown in Appendix L and the constraints refer to Figure 7.2. The constraints used for this model are as follows:

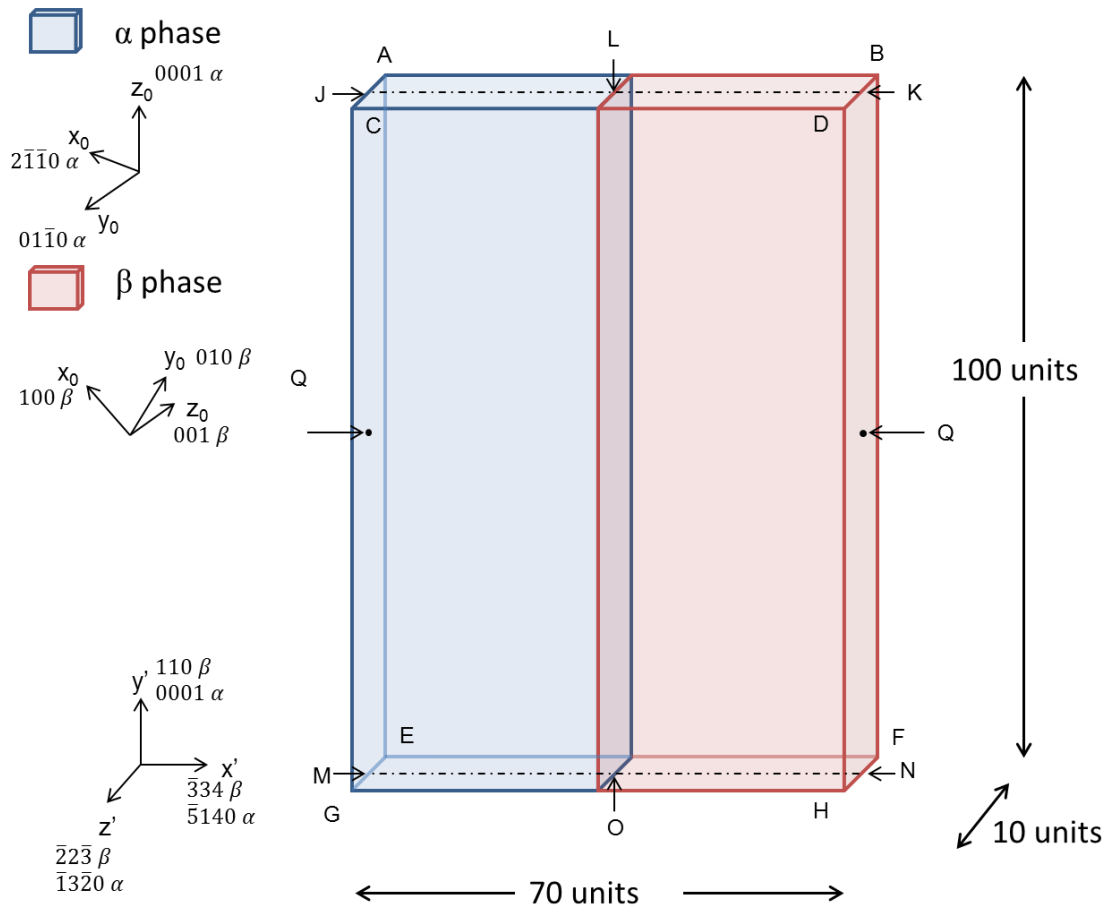


Figure 7.2. Test scenario schematic showing coordinate system orientation and reference points A-N for the bicrystal model base used in this investigation.

1) all nodes on plane EFGH are constrained in the y' direction, 2) all nodes along lines JK and MN are constrained in the z' direction, 3) the node at point L is constrained in the x' and z' directions, 4) the node at point O is constrained in all directions, and 5) the nodes on plane ABCD are constrained to displace the same distance in the y' direction. The model can simulate an actual test specimen; however, due to the nature of FEM the units could be any dimension from microns to miles, as long as applied stresses are consistent with the compliance matrices.

7.4. Mesh generation

The elements chosen for this investigation were solid brick elements with 8 nodes per element. The models used during this study were comprised of 20,000 – 70,000 individual elements. The specific element name as designated by ANSYS is SOLID 185. Each element is assigned a material property and then the elements are “glued” together so that two adjacent elements would share nodes on their common face rather than each have their own set. An applied displacement or load was then directed onto all of the nodes on plane ABCD. It was found that displacing plane ABCD by an amount “ x ” was the stress equivalent of displacing planes ABCD and EFGH an amount “ $1/2x$ ”. In this way, half of a specimen can be modeled where the non-modeled half would mirror the modeled half.

As mentioned before, the units of a FEM model do not necessarily mean anything, it is just the consistency among units and calculations that matters. However, the mesh size for FEM models has a significant effect on model accuracy and computational time. The model in this investigation has been chosen to be 70 units wide

(x direction), 10 units thick (z direction), and 100 units high (y direction). Mesh sizes of 1, 1.25, 2.5, and 5 units were all tested. A mesh size of 1.25 units was decided upon as a good compromise between computational time and accuracy of results. The simulation with a mesh size = 1, took much longer but didn't have any effect on model accuracy. Figure 7.3 is an image of the meshed model for a simple bicrystal as modeled in the ANSYS program.

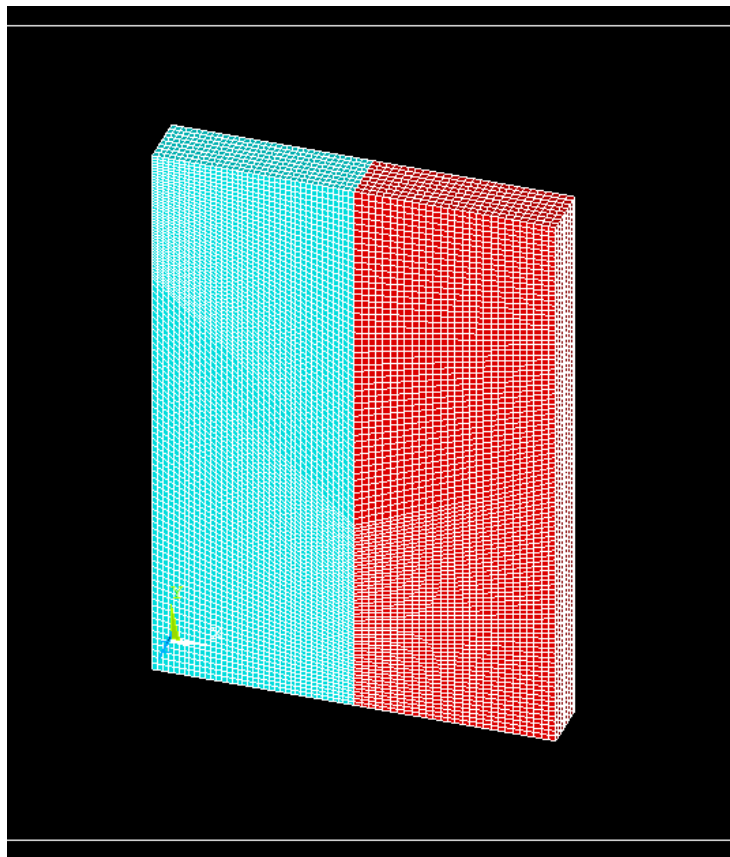


Figure 7.3. ANSYS bicrystal meshed for the study of elastic interactions between α (blue) and β (red) phases of titanium alloys.

7.5. Mesh generation incorporating slip or twinning in α

The next model is also a bicrystal but also incorporates planes in the α phase upon which shear stresses can be directly applied. In this case, the crystallographic orientation of the phases is the same as for the bicrystal case; however, there is a new “phase” present in the alpha phase. The twinned structure of α can be represented by a rotated version of the primed coordinates. This relationship and necessary rotations are shown in the stereographic projection in Figure 7.4. The model can be represented by the test scenario shown in Figure 7.5. The model is meshed as before and the ANSYS simulation is shown in Figure 7.6.

7.6. Results

This investigation began with a check of the FEM calculation. The two phases in the mesh shown in Figure 7.3 were given the same material property and a displacement was applied. The results showed no interaction stresses at the interface and the stress divided by the strain exactly equaled the elastic modulus. It is therefore assumed that these results confirm the validity of the FEM calculation and model constraints. Additionally, the bicrystal model results were then compared with earlier similar work [164]. The results were also consistent in their behavior even if the actual calculated values were different. The specific planes and directions of the plane/direction families that were used to resolve the shear stresses in the following analysis were the maximum resolved values as determined from Appendix G. For example, to resolve YZ shear due to $\{10\bar{1}2\}\langle\bar{1}011\rangle$ twinning onto the $\{332\}\langle113\rangle$ twin plane, the $(33\bar{2})[113]$ system was chosen because that system resolves the most stress.

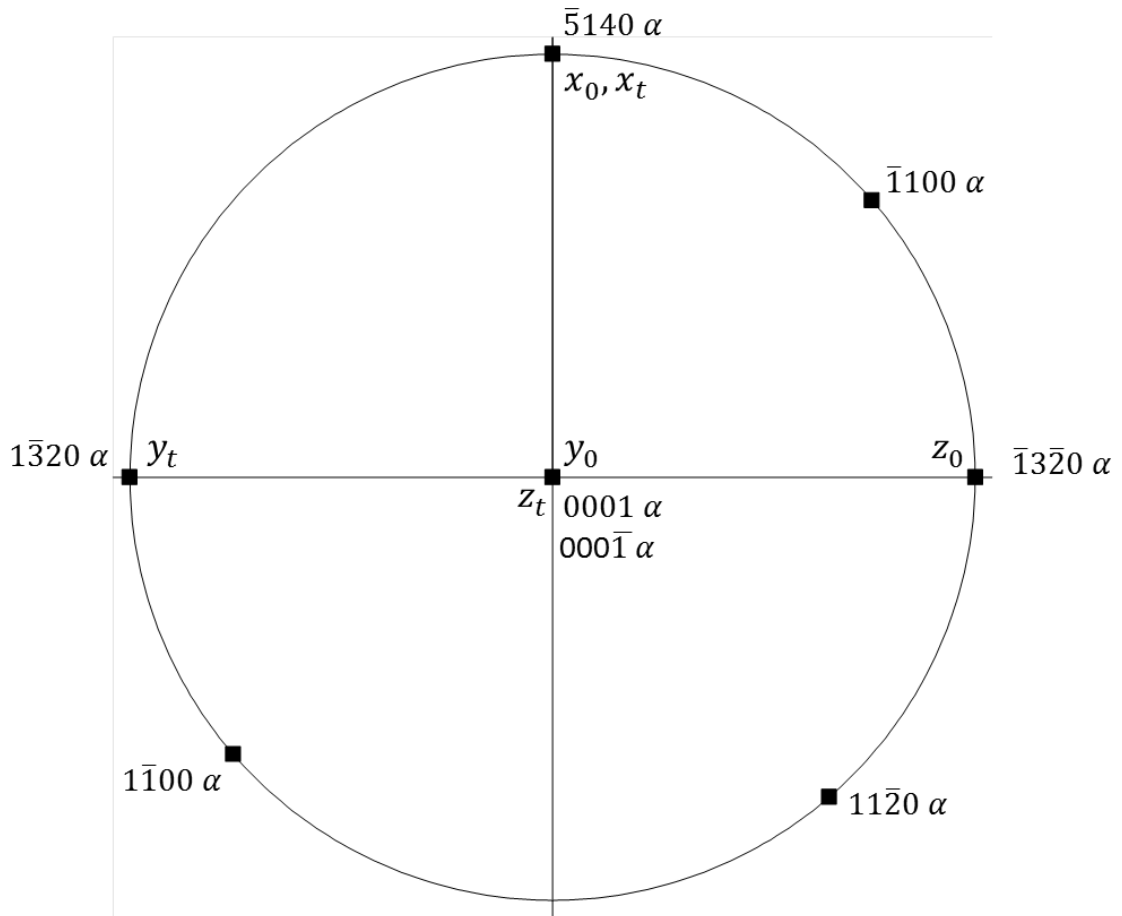


Figure 7.4. A stereographic projection showing the relationship between the orientation of the α phase in the ANSYS coordinate system, and the orientation of the twinned region in the ANSYS coordinate system.

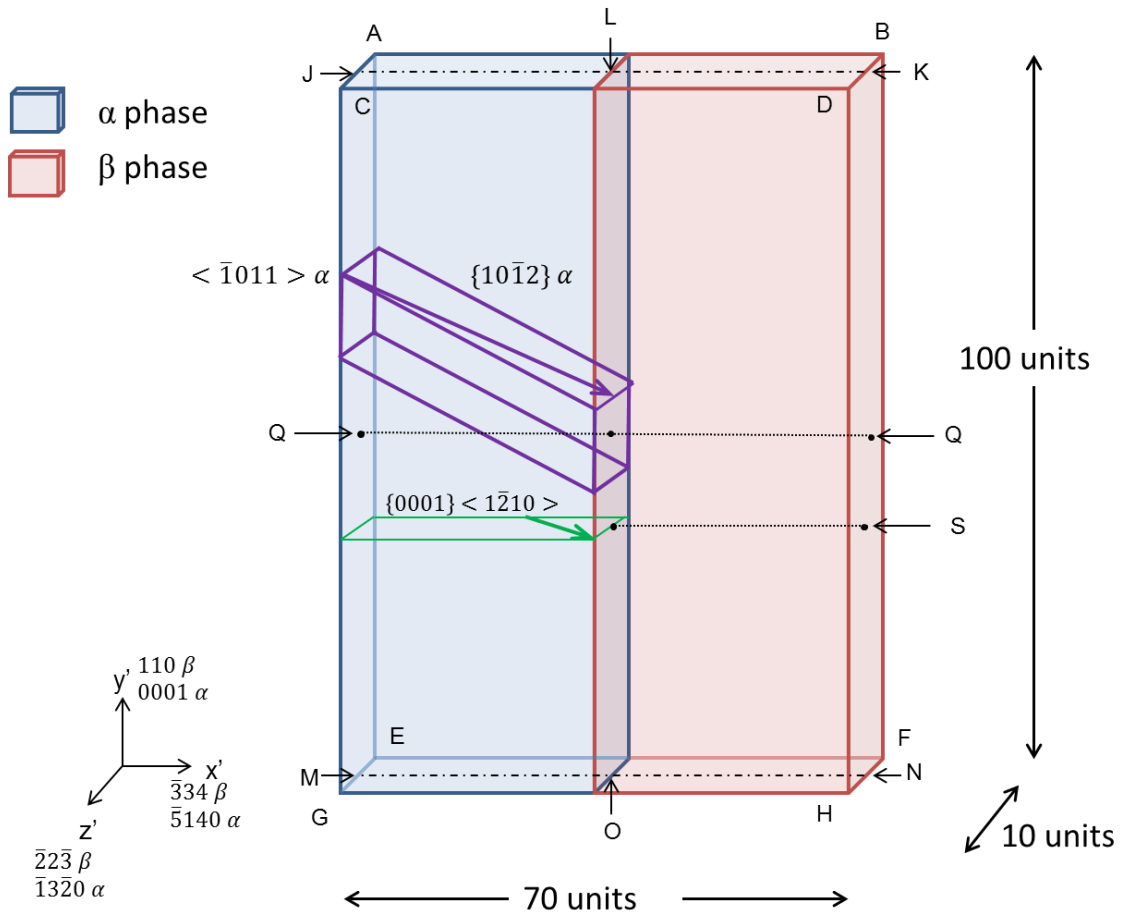


Figure 7.5. A schematic diagram showing the relationship between the twinning and basal slip systems to the oriented model in the ANSYS simulation.

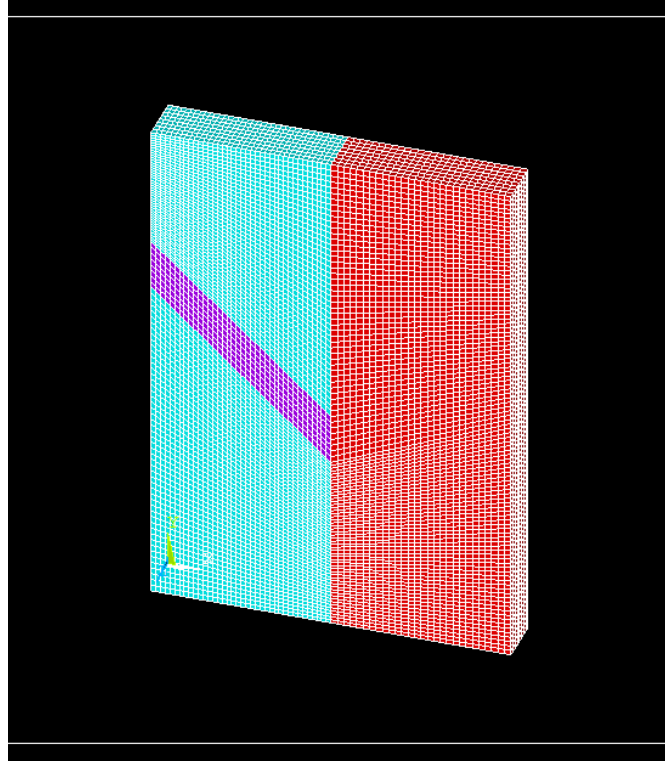


Figure 7.6. ANSYS bicrystal meshed for the study of elastic interactions between α (blue), α twin (purple), and β (red) phases of titanium alloys.

7.6.1. Bicrystal model of α/β interaction stresses

The results from ANSYS are the displacements for all of the nodes and the stresses for all of the elements as mentioned above. Figure 7.7 shows a color fringe plot of the displacements in the y' direction for all of the nodes in the $\alpha + \beta$ bicrystal. Each color represents a range of values. As expected, the nodes in the bottom plane of the model do not move in the y' direction. The normal stresses in the y' direction and YZ shear stresses are shown in Figures 7.8 and 7.9. The units are Pascal since the elastic constants were entered in units of Pascal. Note that the normal y' stresses are higher in the α phase than in the β phase and are also not constant, varying at the interface.

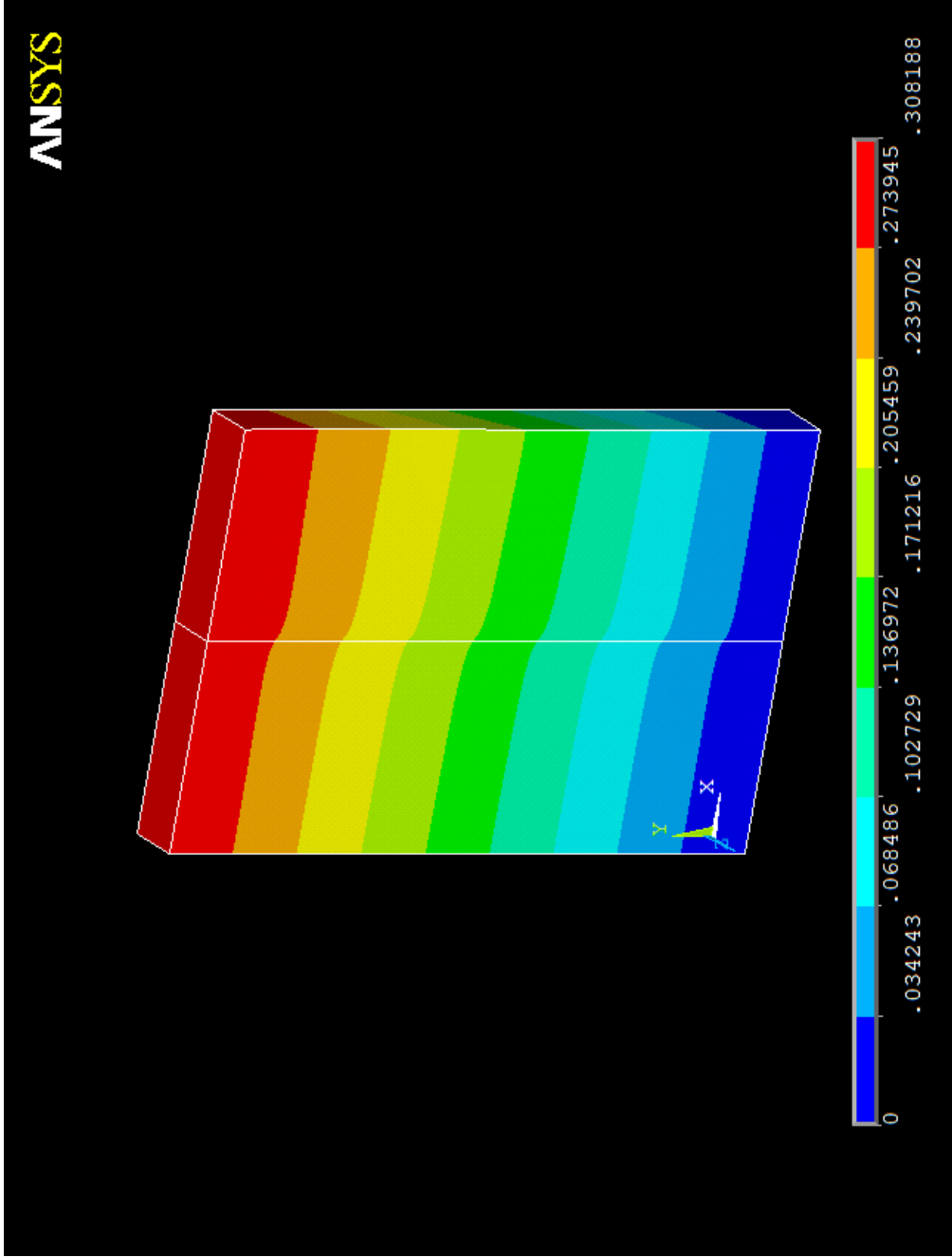


Figure 7.7. Displacements of the nodes in the Y' direction. Note that the displacement of the top nodes is appropriate for the elastic compliance values in the [0001] direction for an applied stress of 359 MPa.

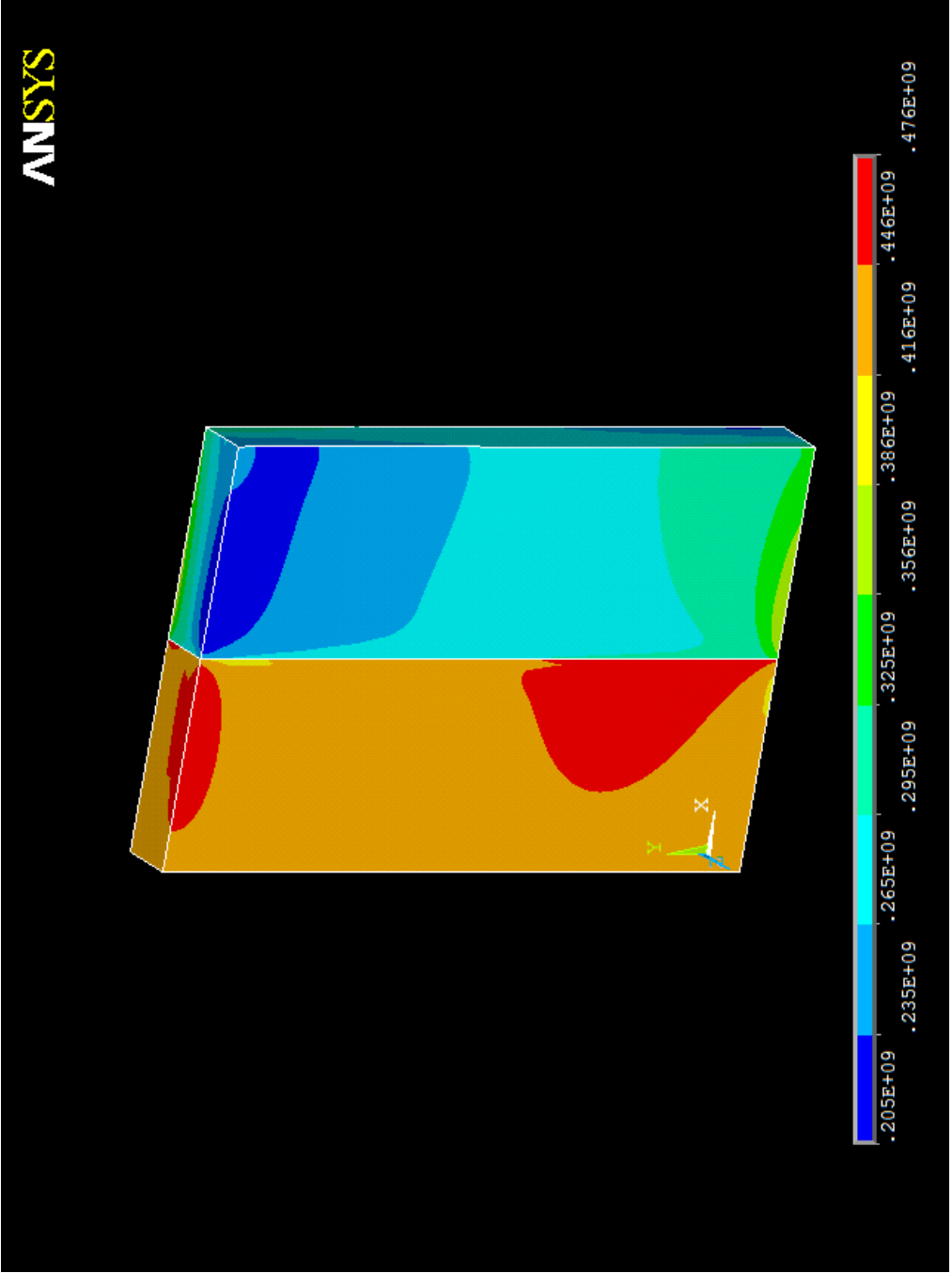


Figure 7.8. Normal stresses in the Y' direction. Note the higher stresses in the α phase as opposed to the β phase.

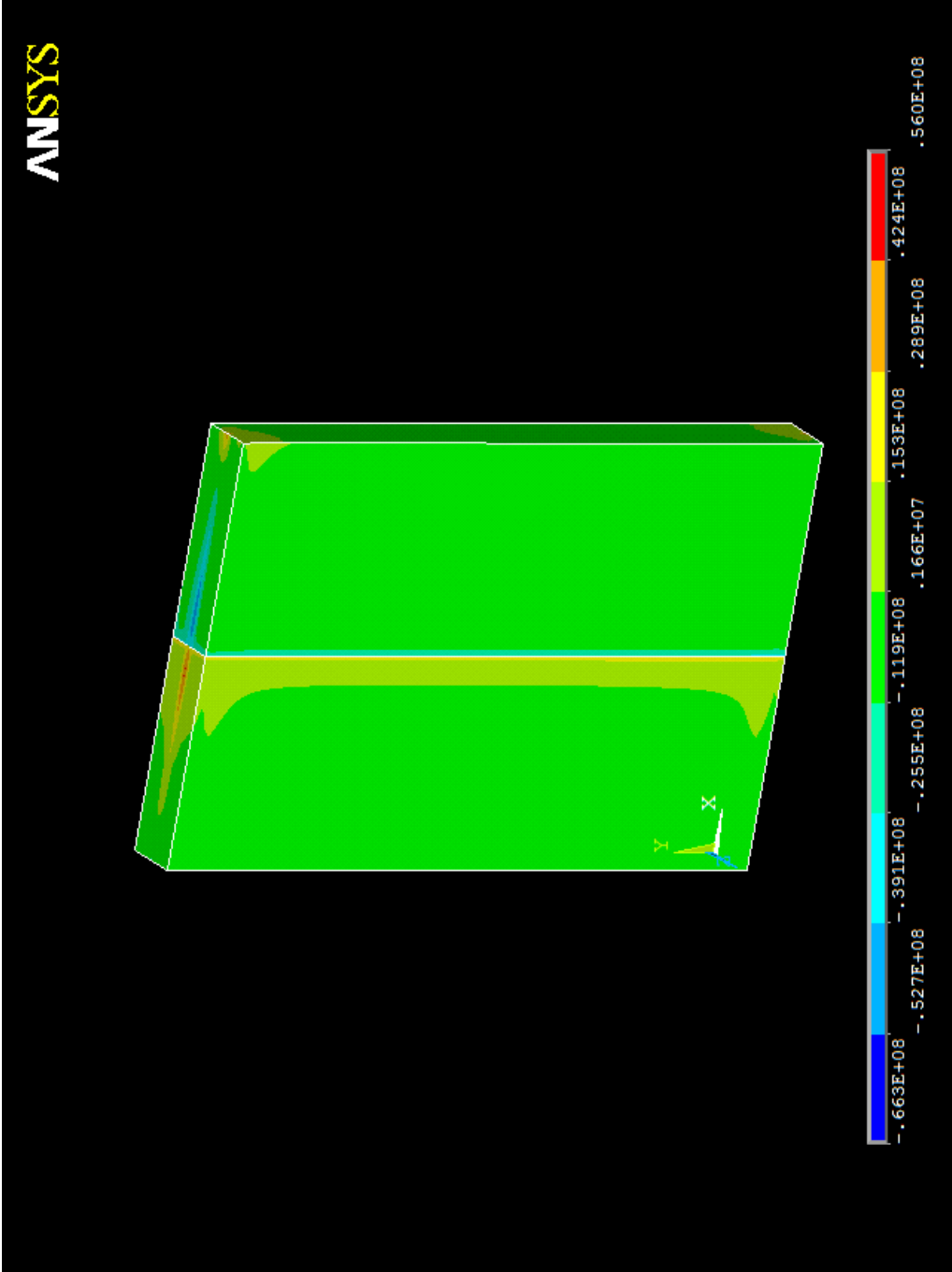


Figure 7.9. Resolved YZ shear stress for elements in the two-phase titanium bicrystal shown in Figure 7.6. Note the interaction stresses at the interface.

The YZ interfacial stress distribution is shown in Figure 7.10. As you can see, as the sample is elastically deformed the stress increases in α and decreases in β . This increase in stress in the α phase is responsible for the twinning that was not observed in the single phase alloy. The stresses of interest are the shear stresses in the β phase resolved onto the β twinning system, and two possible martensite systems. The result is plotted in Figure 7.11 for the horizontal row of elements between points “Q” in Figure 7.3.

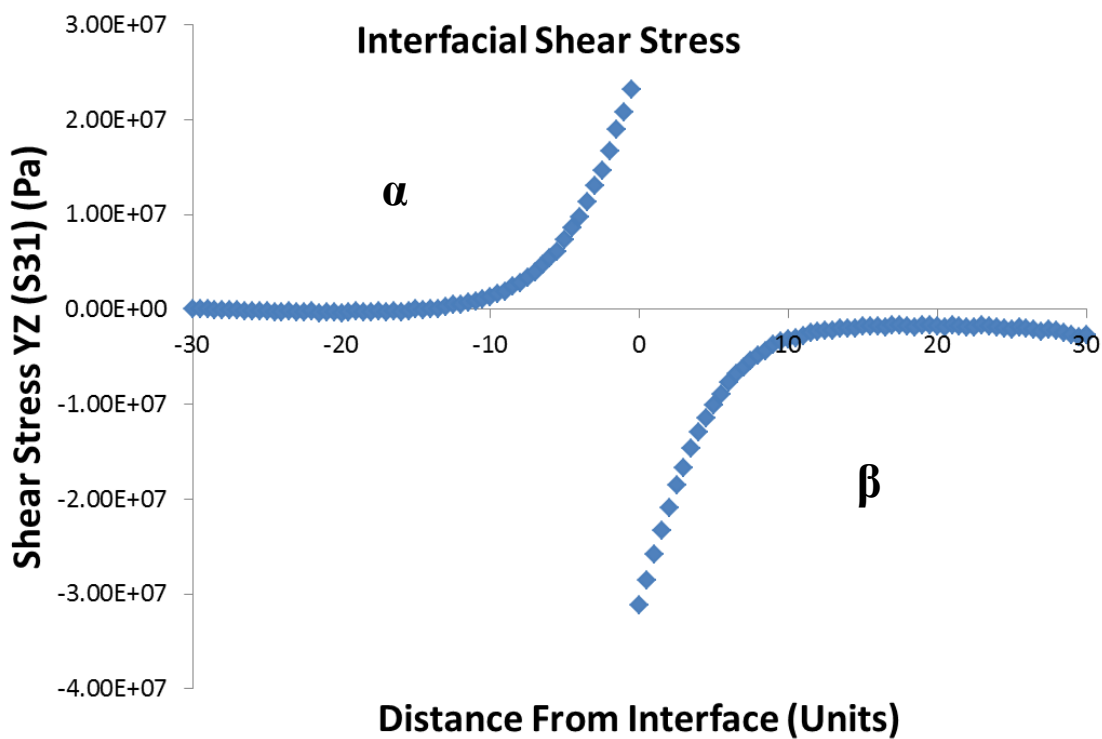


Figure 7.10. The resolved shear stress distribution for a horizontal row of elements in the mesh shown in Figure 7.3. α phase is on the left and β phase is on the right. Notice the very high interaction stresses at the interface.

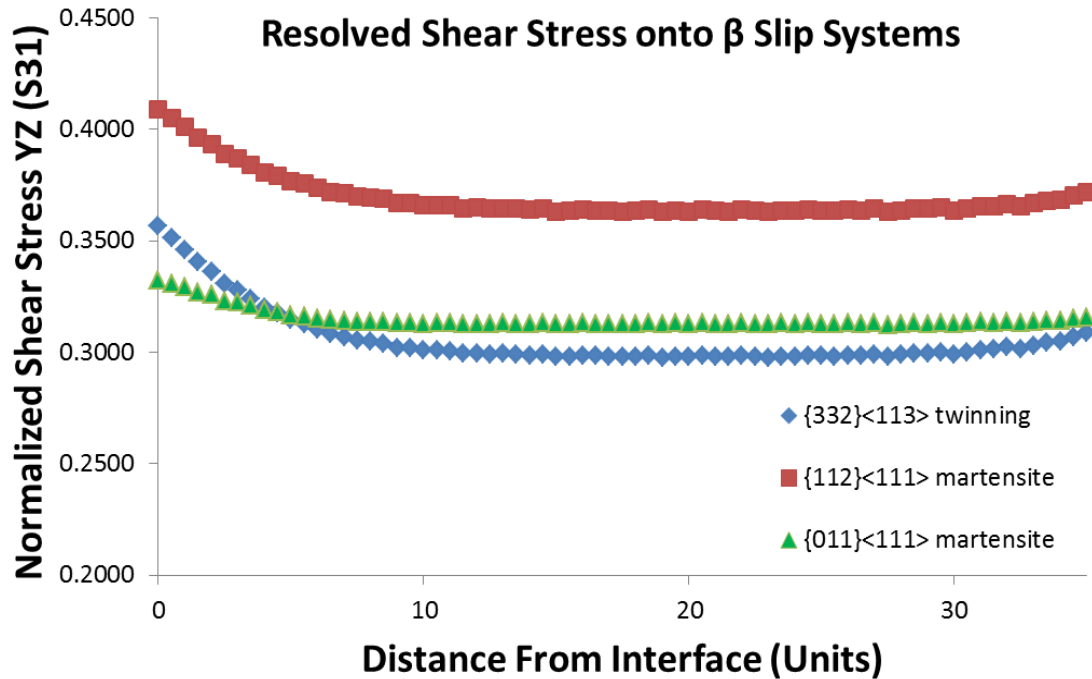


Figure 7.11. The resolved shear stress distribution for a horizontal row of elements in the mesh shown in Figure 7.3. Note that for this orientation of β phase, the resolved shear stress on the martensite system is higher than on the twinning system.

7.6.2. Bicrystal model of α/β interaction stresses due to twinning in α

Figure 7.12 shows a color fringe plot of the normal stresses in the y' direction for all of the nodes in the $\alpha + \beta$ bicrystal with a twin. The YZ shear stresses are shown in Figure 7.13. The units are Pascal since the elastic constants were entered in units of Pascal. Note that the normal y' stresses are higher in the α phase than in the β phase and are also not constant, varying at the interfaces. Also note that stress has been relieved in the twin. The stresses of interest are the shear stresses in the β phase resolved onto the twinning system, and two possible martensite systems. The result is plotted in Figure 7.15 for the horizontal row of elements between points “Q” in Figure 7.3.

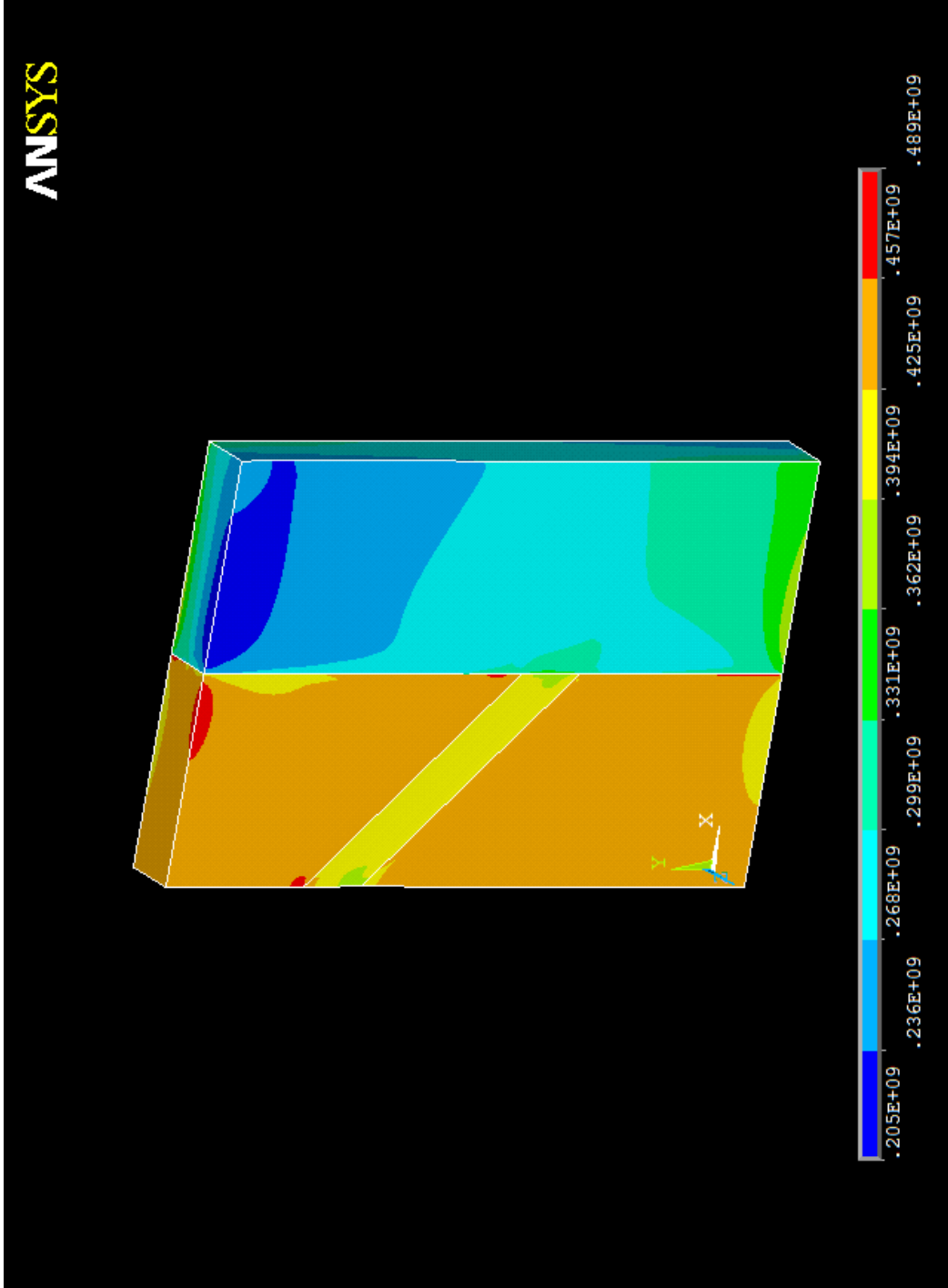


Figure 7.12. The ANSYS simulation results of stresses in the Y' direction. Note that the stresses have been relieved in the twin (as appropriate) and the α phase experiences higher stresses than the β phase.

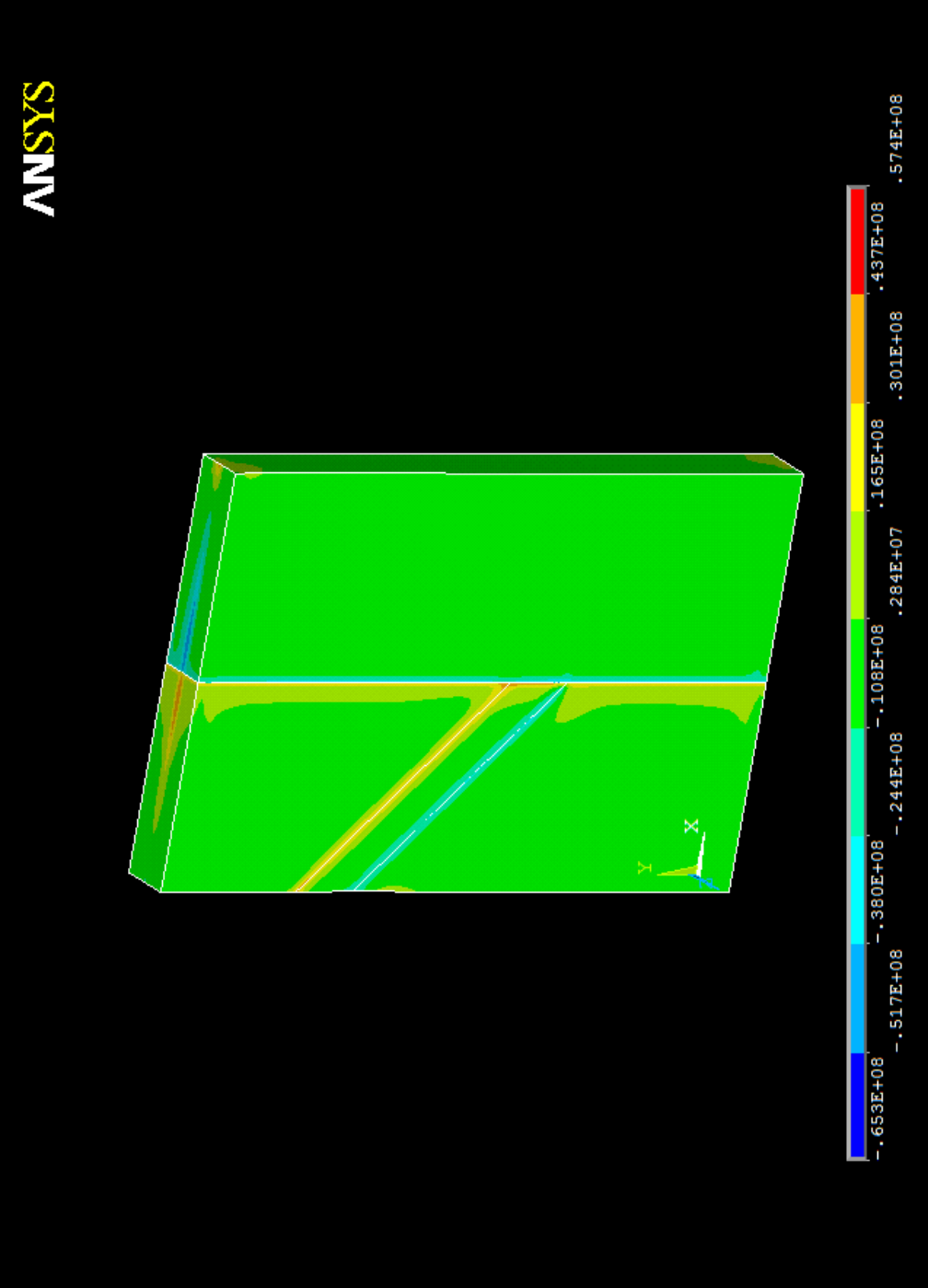


Figure 7.13. The resolved YZ shear stress nodal results as produced by the ANSYS simulation. Note increase in interfacial shear stresses as well as the stresses on the twinning planes.

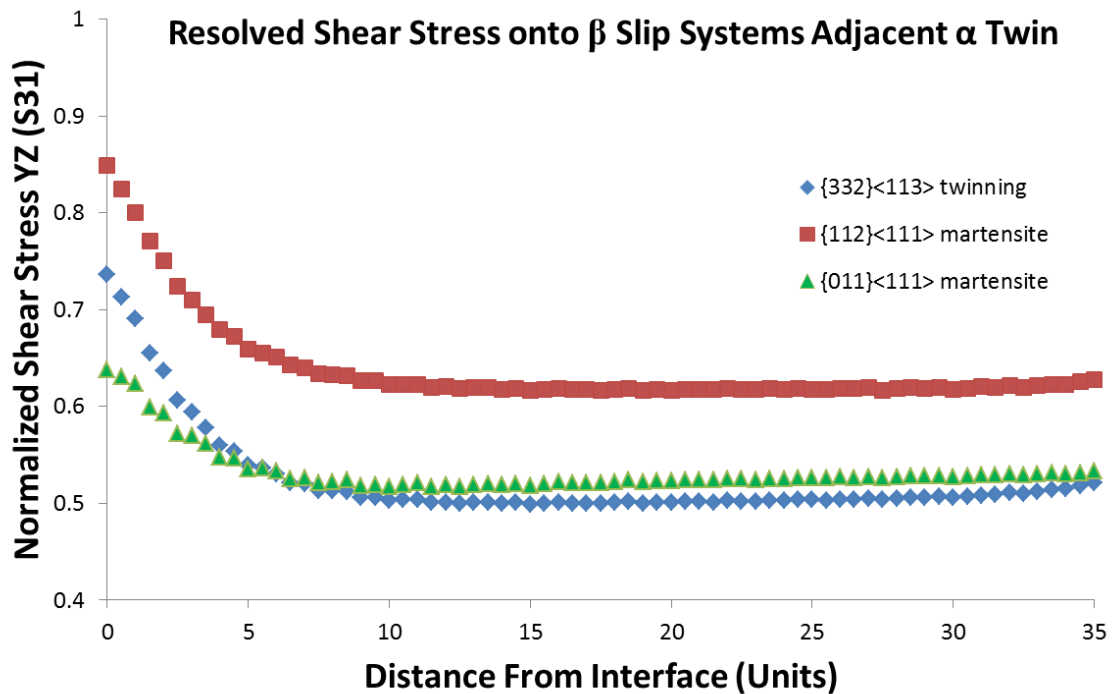


Figure 7.14. The resolved shear stress distribution for a horizontal row of elements between points “Q” in the schematic shown in Figure 7.5. Note that for this orientation of β phase, the resolved shear stress on the martensite system is higher than on the twinning system and the presence of a twin magnifies that effect.

7.6.3. Bicrystal model of α/β interaction stresses due to slip in α

To model slip in the α phase, a feature of ANSYS called the “working plane” must be used. This is a coordinate system that is defined with respect to the global coordinate system. Basal slip of the type $(0001)\langle 1210 \rangle$ will be used as the example for this investigation. This slip system is indicated in green in Figure 7.5. Using the relationships developed earlier, the angles between the global coordinate system (x' , y' , and z') and the working plane’s active coordinate system are found. For this coordinate system, x'' is the slip direction, y'' is the normal to the slip plane, and z'' is the vector perpendicular to the other two as previously defined.

A load can then be applied on the slip plane and in the slip direction in the working plane. This step is required because ANSYS can only apply normal stresses with respect to a defined coordinate system and the slip direction is not aligned with any of the global axis. This normal stress is then resolved into normal and shear stresses in the global coordinate system. The effect of the stresses due to basal slip in the α phase on the β phase are shown in Figure 7.15. Note, in this investigation the applied stress was directly applied to the slip plane. In the previous sections, the stress was applied to the model as a whole. Therefore, the stresses in Figure 7.15 are normalized with respect to the stress on the slip plane rather than normalized with respect to the stress applied to the model.

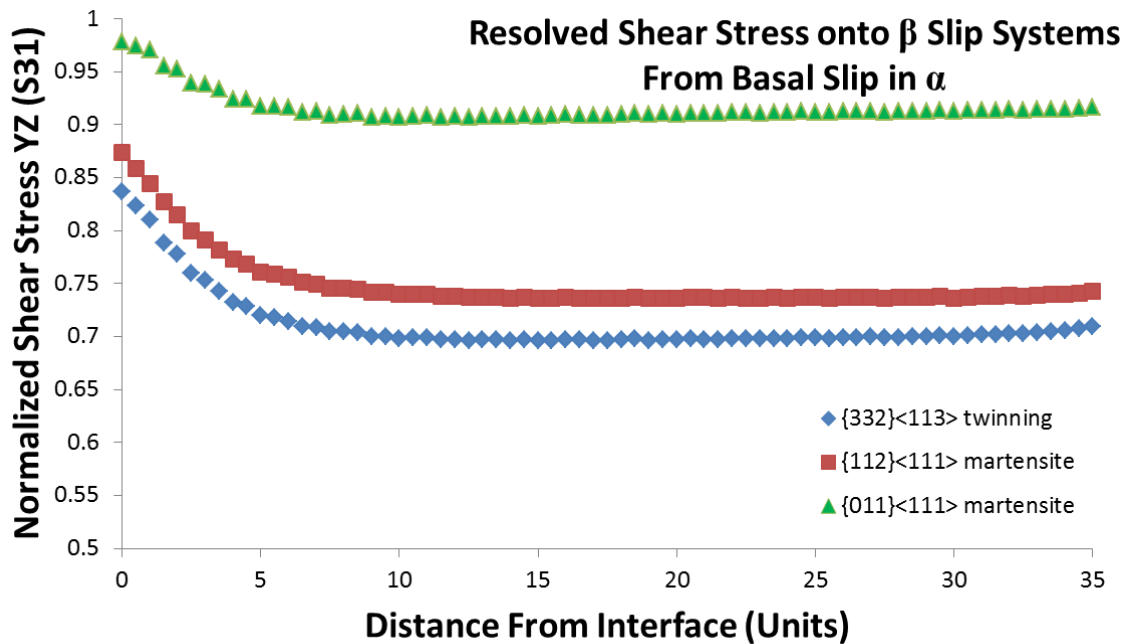


Figure 7.15. The resolved shear stress distribution for a horizontal row of elements along line “S” in the schematic shown in Figure 7.5.

7.7. Discussion

The most important observed data is organized into Table 7.1. In this table, you can see the relationship between the stresses observed by various systems during elastic deformation. In this table, the following should be noted: 1) due to the Burgers orientation relationship, stresses in α are always resolved higher in the martensite slip systems than in twin systems, 2) the FEM results are similar to direct manual calculations, and 3) the difference between the FEM results and the manual calculations can be attributed to interaction stresses. The manual calculations only take into account the geometrical relationship between the individual slip planes and directions. For this reason, these calculations can be a useful tool for predicting trends but as evidenced, FEM can be a very powerful tool to help show a more clear picture of the relationship between the two phases. One of the most important observations is how an interaction stress may decay away from the α/β interface. This information is crucial to the microstructure of the alloy. For example, the stresses in β due to an α twin can favor $\{332\}\langle 113\rangle$ near the interface, but long-range stresses favor $\{011\}\langle 111\rangle$ martensite.

Table 7.1. Maximum resolved shear stresses in β Ti, normalized to applied stress in α , on twinning and hexagonal martensite shear systems.

β Shear System	α Deformation Mechanism		
	Sole Interaction	Basal Slip	$\{10\bar{1}2\}$ Twin
Manual Calculation $\{332\}\langle 113\rangle$	0.385	0.814	0.672
Manual Calculation $\{112\}\langle 111\rangle$	0.472	0.866	0.793
Manual Calculation $\{011\}\langle 111\rangle$	0.408	1	0.849
FEM Result $\{332\}\langle 113\rangle$	0.357	0.837	0.737
FEM Result $\{112\}\langle 111\rangle$	0.409	0.874	0.849
FEM Result $\{011\}\langle 111\rangle$	0.332	0.979	0.638

7.8. Conclusions

1. A three-dimensional anisotropic Finite Element Model (FEM) has been successfully employed to predict the elastic interaction stresses in $\alpha + \beta$ titanium alloys due to phase interactions, twinning in the α phase, and basal slip in the α phase. This modeling can be applied to predict interaction stresses found in many types of deformation, i.e. creep, fatigue, or tensile deformation and to any multiphase material.
2. For a two-phase bicrystal where the interface plane is parallel to the stress axis, the shear stresses in the β martensite (α') system are higher than the $\{332\}\langle 113\rangle$ twinning system and the interaction stresses decayed away in about one-sixth of the plate thickness.
3. These interaction stresses suggest that yielding in the α phase near the α/β interface can occur even though the average applied shear stress is below the yield stress of the α phase.
4. These results agree with earlier studies of two phase $\alpha + \beta$ titanium alloys in which the β phase deformed by stress induced martensite but the single-phase β alloy of a similar composition deformed by twinning. It is suggested that the interaction stresses from due to the α phase so strongly affect the martensite slip systems that the τ_{crss} for martensite is lower becomes lower than the τ_{crss} for twinning.

Chapter 8

Conclusions

1. A crystallographic model was developed, including octahedral interstitial sites, to explain the time-dependent growth of twins in an α -Ti-1.6V alloy. This model for the movement of atoms in HCP titanium allowed for twinning to be a diffusion controlled deformation mechanism. The model specifically addresses how octahedral interstitial sites (which can be occupied by oxygen atoms in α -Ti) are annihilated during the shear and shuffle of atoms required for a $\{10\bar{1}2\}$ twin to form.
2. To test the theory of time-dependent twinning, α -Ti-1.6V with a coarse equiaxed microstructure was tested at strain rates from 10^{-6} to 10^{-1} /s. It was found that the twin size (lamellar thickness) decreases with an increase in strain rate. Classical theories of twinning state that because the energy required for twin growth is so much less than the activation energy required for nucleation, twin growth rates can approach the speed of sound in the material. Under the classical theory, twin sizes should either be independent of strain rate (as long as strain rate is less than speed of sound) or increase with strain rate due to the availability of higher nucleation stresses. However, the opposite was seen to be true. The behavior observed in this study has been attributed to a time-dependent growth process, namely the diffusion of oxygen. It was shown that there exists a strong relationship between twin growth rates and stress assisted diffusion of oxygen to support this conclusion.

3. The creep deformation mechanisms of Ti-4.3V, Ti-8.1V and Ti-12.6V were studied for both Widmanstätten and equiaxed microstructures. The creep deformation mechanisms included slip and twinning in the alpha phase as well as slip, stress induced martensite, and twinning in the β phase. These deformation mechanisms were different from those seen during creep of the respective single-phase α and β alloys with the same compositions. The difference in deformation mechanisms is attributed to interaction stresses between phases.
4. The percentage difference in creep strain between the two microstructures was about equal for the three different alloys studied. The Widmanstätten microstructured alloys exhibited greater creep strain than the equiaxed microstructure for all compositions. This was unexpected and the opposite of what occurs during high temperature creep. This was explained as a result of the Burgers orientation relationship which exists between the α and β phases. At high temperature creep this relationship prevents interface sliding and inhibits creep; however, at low temperatures this relationship provides a template for easy twin or martensite deformation transmission across phase boundaries.
5. Even though the equiaxed microstructure alloys can also have a Burgers orientation relationship between phases, they do not have colonies of aligned grains and so slip transmission is made more difficult, thus reducing creep strain.
6. The law of mixtures was not applicable to determine the creep strain of an intermediate alloy. This is attributed to the interaction stresses between phases which can initiate deformation mechanisms and increase internal stresses beyond what the individual phases would experience.

7. To study the interaction stresses that occur between the α and β phases of titanium, a 3D anisotropic model was developed. This model demonstrated that due to the Burgers orientation relationship between the α and β phases of titanium, the martensite slip systems are much more affected than the twinning systems by the interaction stresses due to phase interactions, slip in the α phase, and twinning in the α phase. These results support the observations of stress induced martensite (SIM) formation in creep deformed two-phase $\alpha + \beta$ alloys with a $\geq 50\%$ volume fraction of the α phase.

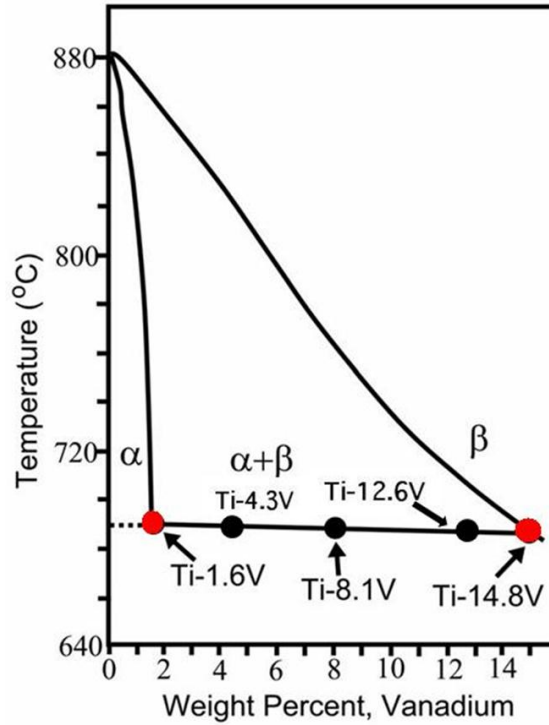
Chapter 9

Suggestions for Future Work

1. Tensile and creep testing of equiaxed and Widmanstätten microstructured Ti-4.3V, Ti-8.1V, and Ti-12.6V alloys at slightly elevated temperatures 358-458 K. These studies will be useful for studying the tensile and creep deformation mechanisms over a larger temperature range, but may also give clues to the extent of the alteration of the M_s temperature of the β phase due to interactions with the α phase. It is expected that as the testing temperature is raised that the β phase deformation mechanism will change from stress induced martensite to twinning. The activation energy can also be calculated for the creep deformation processes, and correlated with published values of activation energy for stress induced martensite and TEM observations.
2. Tensile tests should be conducted beyond 3% strain to fracture in order to study the effect of the newly discovered deformation mechanisms on fracture mechanics. In this regard, fatigue and creep-fatigue testing could also be performed.
3. Three dimensional FEM studies that incorporate crystal plasticity and phase transformation to more accurately model the effect of twin formation and stress induced martensite formation on the interaction stresses between phases.

Appendix A

Ti-V Phase Diagrams and Alloy Compositions

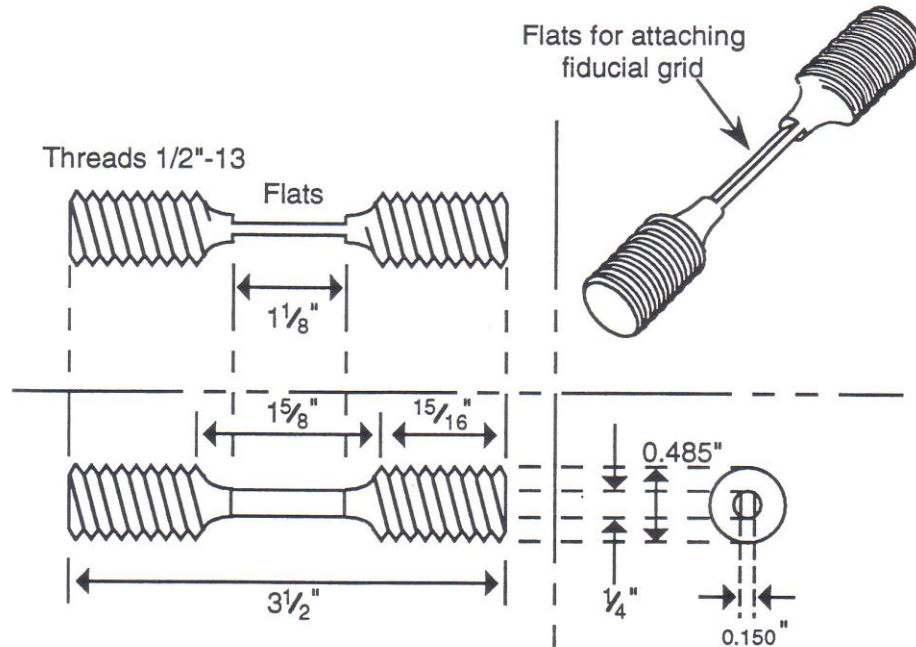


Alloy #	Alloy	Phase Vol. %	α Phase Comp.	β Phase Comp.
1	Ti-1.6wt% V	100% α	~Ti-1.6wt% V	N/A
2	Ti-4.3wt% V	~80% α , ~20% β	~Ti-1.6wt% V	~Ti-14.8wt% V
3	Ti-8.1wt% V	~51% α , ~49% β	~Ti-1.6wt% V	~Ti-14.8wt% V
4	Ti-12.6wt% V	~17% α , ~83% β	~Ti-1.6wt% V	~Ti-14.8wt% V
5	Ti-14.8wt% V	100% β	N/A	~Ti-14.8wt% V

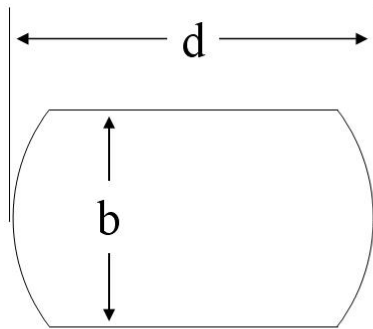
Appendix B

Tensile and Creep Specimen Specifications

Specimen with flats for tensile and creep testing (to be cut by electric discharge machining) for pre and post testing optical and SEM microscopy.



Method for calculating the cross sectional area of the gage length for specimens with the above geometry.



Cross section of tensile or creep specimen

$$Area = \frac{db}{2} \cos\left(\frac{\theta}{2}\right) + \frac{\theta}{180} \pi \left(\frac{d}{2}\right)^2$$

$$\theta = 2 \sin^{-1}\left(\frac{b}{d}\right)$$

Appendix C

Fischione Model 1010 Ion Mill Operation Manual

I. Before Start

1. Make sure the **Gas (Argon) Flow** is connected.
2. The valve of gas tank is opened; the number of pressure is at two divisions.
3. Power cord is connected.
4. The cooling water flow is connected and valve is opened.
5. The **Dewar Conductor Rod** is not engaged.

II. Start Up

1. Press the **Main Power Switch** on the lower rear instrument panel to on.
2. Press the power button on the computer to on. The desktop screen will appear with icons for four Model 1010 programs:
 - Dewar Bakeout
 - Log Viewer
 - Ion Mill
 - Laser Calibration

III. Dewar Bakeout (Option: Perform this step before using cooling stage)

1. Close all open programs.
2. Remove all specimens from the stage if there is any specimen inside. Heat from the bakeout could damage the specimen.

3. Double click the **Dewar Bakeout** icon on the desktop to initiate the Dewar flask heating program.
4. Click **Press to Enable Pumps** to turn on the pumps.
5. Engage the **Dewar Conductor Rod** until thermal contact is made with the specimen stage.
 - a. Rotate the **Dewar knob** clockwise, as viewed facing the instrument's rear panel.
 - b. Rotate the **Dewar knob** until its pin contacts the pin stop, preventing further rotation. When the specimen stage is heated to above setpoint (100 C) and the vacuum is less than 8×10^{-4} torr, the Dewar valve opens.
6. Click **Press to Enable Bakeout** to turn on the heater. The high temperature setpoint is 100.0 C.
7. Enter a time (hrs:min:sec). 10 minutes is usually sufficient for daily, routine maintenance.
8. Click **Start**. When the time has expired, the heater and pumps will turn off, the Dewar valve will close, and a dialog box appears indicating the procedure is finished.
9. Open the Ion Mill program
10. Wait until the temperature drop back to 30~40 C. Temperature of the Dewar must be lower than 40 degree before filling with Liquid N. Wait. Otherwise, it will damage the dewar.
11. Click **Vent** to release the vacuum.

12. Disengage the Dewar conductor rod by rotating its knob counterclockwise, as viewed from the rear of the instrument. Rotate the Dewar knob until its pin contacts the pin stop, and no further rotation is possible.

IV. Loading TEM Specimens

1. Place the TEM specimen into the **recessed bottom plate** with manual or vacuum tweezers.
2. For a cross-section specimen, align the epoxy joints of the specimen parallel to the supporter.
3. Position **the top plate** and attached spring over the bottom plate.
4. Compressing the spring with manual tweezers, insert the left, top, and finally right leg of the spring into the available groove.
5. Align the double line on the gear so it points to the position 1 (6 o'clock direction) for using both ion sources, position 2 (7 o'clock direction) for using only top source, and position 3 (5 o'clock direction) for using only bottom source.

V. Ion Milling

1. Double click on the Ion Mill icon to start the **Ion Milling Program**.
2. Wait until the initializing phase is completed.
3. Click Vent to release the vacuum.
4. Load TEM Specimen. (**IV. Loading TEM Specimens**)
5. Click Pump to evacuate the specimen chamber.

6. Set the default parameters for the ion sources (**voltage** and **current**), **stage rotation**, and **milling angle, duration time, ending point**. If the sample is thick (ex. > 10 μm), start with high voltage (> 5 keV) and angle (18.0~23.0). If the sample is thin (< 5 μm), start with low voltage (3~4 keV) and angle (< 15.0)
7. Wait until reach a vacuum of about 2×10^{-5} torr.
8. If the specimen needs to be cooled, engage the conductor rod by rotating the Dewar knob clockwise, as viewed from the rear of the instrument. Rotate until the pin on the knob contacts the pin stop.

Skip steps 8~10 if the specimen is not to be cooled. Make sure perform step III before specimen cooling.

9. Fill the Dewar with liquid nitrogen.
10. Wait for the temperature to reach the minimum desired value, often -120.0 C.
11. Make sure **window shutter** close and click Start to execute the process. Stop ion milling once a small hole is found. Perform ion milling again at very low voltage (3 keV) and angle (5.0~10.0) to remove all the defects caused by ion milling.
12. When finished, if specimen cooling was used, disengage the conductor rod by rotating the Dewar knob counterclockwise until the knob's pin contacts the pin stop. Vent chamber, stage temperature will heat up to > 20.0 C and then vent automatically.
13. Take out specimen.

VI. Shutdown Procedure

1. If the instrument is vented, click Pump in the on Milling program. Verify that the vacuum level is 2×10^{-5} torr.
2. Close the Ion Mill program.
3. Shutdown the computer through Microsoft Windows.
4. Press the main power switch to turn it off.
5. Close the valves of gas and water supply to the instrument.
6. Sign out the login-sheet.

Appendix D

Operating Instructions for JEOL 2100F Field Emission TEM

The following is a brief outline of the operating instructions for the JEOL 2100F Field Emission TEM. This instrument should NOT be operated without proper training and certification by NISP Laboratory management. This outline is not a substitute for the official TEM operating manual.

PRELIMINARY STEPS

1. Load specimen onto double tilt holder. Specimen retainer is held down by a small screw. Make sure specimen is secure and centered. Check O-rings on the holder for lint which may compromise the vacuum.
2. Fill cold-trap to the left of the column with liquid nitrogen.
3. Raise High-Voltage Control window on the computer. Under Auto HT & Emission, click on StartUp to begin accelerating voltage. The status bar will show the time until the accelerating voltage of 200 kV is reached.

INSERTING SPECIMEN HOLDER INTO COLUMN

4. Open Specimen Property window on computer. Select Double Tilt Holder from drop down menu. Click Apply.
5. Align the specimen holder guide pin with the guide groove on the microscope column. Push the holder into the goniometer until it stops and set the goniometer

PUMP/AIR switch to PUMP. The yellow light will turn on and the evacuation will begin. It will take about 10 minutes to pump down, until the green light on the goniometer goes on.

6. When the green light is on, turn the specimen holder clockwise and push the holder into the goniometer as far as it will go.
7. Turn holder fully clockwise and push in into the yellow light on the goniometer goes off.
8. Connect the cable from the end of the double tilt holder into the port above the specimen holder.

Appendix E

Rotation Calibration for JEOL 2100F Field Emission TEM

The angle is rotation angle of bright field image from diffraction pattern.

Magnification/ Camera length	60 cm	80 cm	100 cm	120 cm	150 cm
50	71° CW	71° CW	71° CW	71° CW	71° CW
80	71° CW	71° CW	71° CW	71° CW	71° CW
100	71° CW	71° CW	71° CW	71° CW	71° CW
150	71° CW	71° CW	71° CW	71° CW	71° CW
200	71° CW	71° CW	71° CW	71° CW	71° CW
300	71° CW	71° CW	71° CW	71° CW	71° CW
400	64° CW	64° CW	64° CW	64° CW	64° CW
500	3° CCW	3° CCW	3° CCW	3° CCW	3° CCW
600	3° CCW	3° CCW	3° CCW	3° CCW	3° CCW
800	3° CCW	3° CCW	3° CCW	3° CCW	3° CCW
1000	3° CCW	3° CCW	3° CCW	3° CCW	3° CCW
1200	3° CCW	3° CCW	3° CCW	3° CCW	3° CCW
1500	3° CCW	3° CCW	3° CCW	3° CCW	3° CCW
2500	3° CCW	3° CCW	3° CCW	3° CCW	3° CCW
3k	3° CCW	3° CCW	3° CCW	3° CCW	3° CCW
4k	3° CCW	3° CCW	3° CCW	3° CCW	3° CCW
5k	3° CCW	3° CCW	3° CCW	3° CCW	3° CCW
6k	3° CCW	3° CCW	3° CCW	3° CCW	3° CCW
8k	3° CCW	3° CCW	3° CCW	3° CCW	3° CCW
10k	3° CCW	3° CCW	3° CCW	3° CCW	3° CCW
12k	3° CCW	3° CCW	3° CCW	3° CCW	3° CCW
15k	3° CCW	3° CCW	3° CCW	3° CCW	3° CCW
20k	3° CCW	3° CCW	3° CCW	3° CCW	3° CCW
30k	3° CCW	3° CCW	3° CCW	3° CCW	3° CCW
40k	3° CCW	3° CCW	3° CCW	3° CCW	3° CCW
50k	0°	0°	0°	0°	0°
60k	3° CW	3° CW	3° CW	3° CW	3° CW
80k	2° CCW	2° CCW	2° CCW	2° CCW	2° CCW
100k	2° CCW	2° CCW	2° CCW	2° CCW	2° CCW
120k	28° CW	28° CW	28° CW	28° CW	28° CW
150k	28° CW	28° CW	28° CW	28° CW	28° CW
200k	28° CW	28° CW	28° CW	28° CW	28° CW
300k	28° CW	28° CW	28° CW	28° CW	28° CW
400k	28° CW	28° CW	28° CW	28° CW	28° CW
500k	28° CW	28° CW	28° CW	28° CW	28° CW
600k	28° CW	28° CW	28° CW	28° CW	28° CW
800k	28° CW	28° CW	28° CW	28° CW	28° CW
1 M	28° CW	28° CW	28° CW	28° CW	28° CW
1.2 M	28° CW	28° CW	28° CW	28° CW	28° CW
1.5 M	28° CW	28° CW	28° CW	28° CW	28° CW

Appendix F

α Phase Coordinate Conversion to Parallel Directions in β

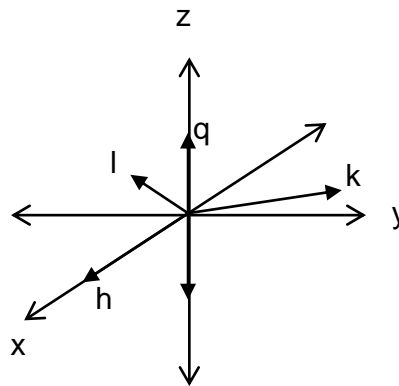
4 to 3 Coordinate Conversion Equations

Conversion of 4 coordinate directions [hklq] for the α phase (hcp) or ω phase (P6/mmm) to directions in the 3 coordinate [xyz] Cartesian system. Consideration for the c/a ratio hexagonal crystal must be taken to calculate the correct z coordinate with respect to the x and y coordinates.

$$x = h - k \sin 30^\circ - l \sin 30^\circ$$

$$y = k \cos 30^\circ - l \cos 30^\circ$$

$$z = \frac{\sqrt{x^2 + y^2}}{\sqrt{3}} \frac{c}{a}$$



$\alpha \rightarrow \beta$ Coordinate Conversion Matrix

Conversion matrix for the calculation of parallel directions in the β phase to a given direction in the α phase of a two-phase titanium alloy with a Burgers orientation relationship $\langle 1\bar{2}10 \rangle (0001)_\alpha // \langle 1\bar{1}1 \rangle (110)_\beta$. If this conversion is used for planes, care must be taken to make sure that the plane normal is actually perpendicular to the plane. Planes and directions in the HCP system are not necessarily perpendicular as they are in a cubic system.

$$\begin{bmatrix} -.2638797 & -.81902 & \frac{\sqrt{2}}{2} \\ .2638797 & .81902 & \frac{\sqrt{2}}{2} \\ -1.8392 & -1.72853 & 0 \end{bmatrix}$$

Appendix G

Prism Slip in Alpha - Resolved Shear Stress on Beta Twins

Alpha slip direction	Alpha slip direction	Alpha slip direction
1 1 -2 0	1 -2 1 0	-2 1 1 0
Parallel direction in beta	Parallel direction in beta	Parallel direction in beta
0.26 -0.26 -3.07	1.732 -1.732 1.732	-1.992 1.992 1.3
Slip plane in alpha	Slip plane in alpha	Slip plane in alpha
1 -1 0 0	-1 0 1 0	0 -1 1 0
Parallel plane in beta	Parallel plane in beta	Parallel plane in beta
1.241 -1.241 0.13	-0.75 0.75 1.472	0.491 -0.49 1.6

Vectors of twinning shear systems

Plane	Direction			
3 3 -2	1 1 3	0.056	-0.36	-0.305
3 -3 2	-1 1 3	-0.772	0.936	0.163
-3 3 2	1 -1 3	0.477	0.523	1
3 3 2	1 1 -3	0.056	-0.36	-0.305
3 -2 3	1 3 1	-0.06	0.473	0.413
3 2 -3	-1 3 1	-0.582	0.134	-0.448
3 2 3	1 -3 1	-0.578	0.25	-0.328
-3 2 3	1 3 -1	0.149	-0.5	-0.353
-2 3 3	3 1 1	-0.149	0.502	0.353
2 3 3	-3 1 1	0.582	-0.13	0.448
2 3 -3	3 -1 1	0.578	-0.25	0.328
2 -3 3	3 1 -1	0.06	-0.47	-0.413

Prism Slip in Alpha - Resolved Shear Stress on Martensite Shear System I

Alpha slip direction	1	1	-2	0
Parallel direction in beta	0.26	-0.26	-3.07	
Slip plane in alpha	1	-1	0	0
Parallel plane in beta	1.241	-1.241	0.13	

Alpha slip direction	1	-2	1	0
Parallel direction in beta	1.732	-1.732	1.732	
Slip plane in alpha	-1	0	1	0
Parallel plane in beta	-0.75	0.75	1.472	

Alpha slip direction	-2	1	1	0
Parallel direction in beta	-1.992	1.992	1.3	
Slip plane in alpha	0	-1	1	0
Parallel plane in beta	0.491	-0.49	1.6	

Vectors of martensite shear system I

Plane	Direction								
1	1	2	1	1	-1	0.069			-0.372
-1	1	2	1	-1	1	-0.508		1	0.492
1	-1	2	-1	1	1	0.147		0.783	0.93
1	1	-2	1	1	1	0.069		-0.44	-0.372
1	2	1	1	-1	1	-0.254		0.5	0.246
-1	2	1	1	1	-1	-0.456		-0.06	-0.515
1	-2	1	1	1	1	-0.525		0.383	-0.142
1	2	-1	-1	1	1	-0.073		-0.39	-0.465
2	1	1	-1	1	1	0.073		0.392	0.465
-2	1	1	1	1	1	0.456		0.058	0.515
2	-1	1	1	1	-1	0.525		-0.38	0.142
2	1	-1	1	-1	1	0.254		-0.5	-0.246

Prism Slip in Alpha - Resolved Shear Stress on Martensite Shear System II

Alpha slip direction	1	1	-2	0
Parallel direction in beta	0.26	-0.26	-3.07	
Slip plane in alpha	1	-1	0	0
Parallel plane in beta	1.241	-1.241	0.13	

Alpha slip direction	1	-2	1	0
Parallel direction in beta	1.732	-1.732	1.732	
Slip plane in alpha	-1	0	1	0
Parallel plane in beta	-0.75	0.75	1.472	

Alpha slip direction	-2	1	1	0
Parallel direction in beta	-1.992	1.992	1.3	
Slip plane in alpha	0	-1	1	0
Parallel plane in beta	0.491	-0.49	1.6	

Vectors of martensite shear system II

Plane	Direction			
1 0 1	1	1	-1	0.343
1 0 1	-1	1	1	0.127
-1 0 1	1	-1	1	-0.44
-1 0 1	1	1	1	0.224
1 1 0	1	-1	1	0
1 1 0	-1	1	1	0
-1 1 0	1	1	-1	-0.567
-1 1 0	1	1	1	0.567
0 1 1	1	1	-1	-0.224
0 1 1	1	-1	1	-0.44
0 -1 1	-1	1	1	0.127
0 -1 1	1	1	1	-0.343
				-0.48
				0.678
				0.866
				0.289
				0
				0
				0.188
				-0.19
				-0.29
				0.866
				0.678
				0.476
				-0.133
				0.805
				0.426
				0.512
				0
				0
				-0.379
				0.379
				-0.512
				0.426
				0.805
				0.133

Basal Slip in Alpha - Resolved Shear Stress on Beta Twins

Alpha slip direction	Alpha slip direction	Alpha slip direction	Alpha slip direction
1 1 -2 0	1 -2 1 0	-2 1 1 0	-2 1 1 0
Parallel direction in beta	Parallel direction in beta	Parallel direction in beta	Parallel direction in beta
0.26 -0.26 -3.07	1.732 -1.732 1.732	-1.992 1.992 1.3	-1.992 1.992 1.3
Slip plane in alpha	Slip plane in alpha	Slip plane in alpha	Slip plane in alpha
0 0 0 1	0 0 0 1	0 0 0 1	0 0 0 1
Parallel plane in beta	Parallel plane in beta	Parallel plane in beta	Parallel plane in beta
1 1 1 0	1 1 1 0	1 1 1 0	1 1 1 0

Vectors of twinning shear system

Plane	Direction				
3 3 -2	1 1 3	-0.632	0.367	-0.268	0.274
3 -3 2	-1 1 3	0	0	0.503	0
-3 3 2	1 -1 3	0	0	-0.542	0
3 3 2	1 1 -3	0.632	-0.37	0.777	-0.274
3 -2 3	1 3 1	-0.518	0.814	-0.268	-0.268
3 2 -3	-1 3 1	-0.023	-0.5	0.503	0.503
3 2 3	1 -3 1	0.114	0.446	-0.542	-0.542
-3 2 3	1 3 -1	-0.655	-0.13	0.777	0.777
-2 3 3	3 1 1	-0.655	-0.13	0.777	0.777
2 3 3	-3 1 1	-0.023	-0.5	0.503	0.503
2 3 -3	3 -1 1	0.114	0.446	-0.542	-0.542
2 -3 3	3 1 -1	-0.518	0.814	-0.268	-0.268

Basal Slip in Alpha - Resolved Shear Stress on Martensite Shear System I

Alpha slip direction	1	1	-2	0
Parallel direction in beta	0.26	-0.26	-3.07	
Slip plane in alpha	0	0	0	1
Parallel plane in beta	1	1	1	0

Alpha slip direction	1	-2	1	0
Parallel direction in beta	1.732	-1.732	1.732	
Slip plane in alpha	0	0	0	1
Parallel plane in beta	1	1	1	0

Alpha slip direction	-2	1	1	0
Parallel direction in beta	-1.992	1.992	1.3	
Slip plane in alpha	0	0	0	1
Parallel plane in beta	1	1	1	0

Vectors of martensite shear system I

Plane	Direction			
1	1	1	1	-1
-1	1	1	-1	1
1	-1	2	-1	1
1	1	-2	1	1
1	2	1	1	-1
-1	2	1	1	-1
1	-2	1	1	1
1	2	-1	-1	1
2	1	1	1	1
-2	1	1	1	1
2	-1	1	1	-1
2	1	-1	1	1

		0.192		0.143
		0		0
		0		0
		-0.19		-0.143
		0.866		-0.423
		-0.48		0.71
		0.674		-0.567
		-0.29		0.853
		-0.29		0.853
		-0.48		0.71
		0.674		-0.567
		0.866		-0.423

Basal Slip in Alpha - Resolved Shear Stress on Martensite Shear System II

Alpha slip direction	Alpha slip direction	Alpha slip direction
1 1 -2 0	1 -2 1 0	-2 1 1 0
Parallel direction in beta	Parallel direction in beta	Parallel direction in beta
0.26 -0.26 -3.07	1.732 -1.732 1.732	-1.992 1.992 1.3
Slip plane in alpha	Slip plane in alpha	Slip plane in alpha
0 0 0 1	0 0 0 1	0 0 0 1
Parallel plane in beta	Parallel plane in beta	Parallel plane in beta
1 1 1 0	1 1 1 0	1 1 1 0

Vectors of martensite shear system II

Plane	Direction			
1 0 1	1 1 -1	-0.238		-0.244
1 0 1	-1 1 1	-0.335	0.5	0.493
-1 0 1	1 -1 1	0.238	-0.17	0.244
-1 0 1	1 1 1	-0.335	-0.5	0.493
1 1 0	1 -1 1	-0.476	-0.17	-0.489
1 1 0	-1 1 1	-0.67	1	0.985
-1 1 0	1 1 -1	-0.097	-0.33	0.737
-1 1 0	1 1 1	-0.097	-0.67	0.737
0 1 1	1 1 -1	-0.335	-0.17	0.493
0 1 1	1 -1 1	-0.238	0.5	-0.244
0 -1 1	-1 1 1	0.335	0.167	-0.493
0 -1 1	1 1 1	-0.238	0.5	-0.244

1012 Twinning in Alpha - Resolved Shear Stress on Beta Twins

Alpha twinning direction	1	0	-1	1
Parallel direction in beta	1.882	0.381	-1.47	
Shear plane in alpha	-1	0	1	2
Parallel plane in beta	0.575	2.0762	1.472	

Alpha twinning direction	-1	0	1	1
Parallel direction in beta	0.381	1.882	1.472	
Shear plane in alpha	1	0	-1	2
Parallel plane in beta	2.076	0.575	-1.47	

Alpha twinning direction	0	1	-1	1
Parallel direction in beta	0.641	1.622	-1.6	
Shear plane in alpha	0	-1	1	2
Parallel plane in beta	1.817	0.835	1.6	

Vectors of twinning shear direction

Plane	Direction			
3 3 -2	1	1	3	0.591
3 -3 2	-1	1	3	0.188
-3 3 2	1	-1	3	-0.442
3 3 2	1	1	-3	0.672
3 -2 3	1	3	1	0.071
3 2 -3	-1	3	1	0.752
3 2 3	1	-3	1	-0.162
-3 2 3	1	3	-1	-0.192
-2 3 3	3	1	1	0.062
2 3 3	-3	1	1	-0.8
2 3 -3	3	-1	1	0.221
2 -3 3	3	1	-1	-0.093
				0.672
				0.188
				-0.44
				0.591
				0.093
				0.8
				-0.22
				-0.06
				0.192
				-0.75
				0.162
				-0.07
				0.662
				-0.498
				-0.032
				0.754
				-0.029
				0.306
				-0.733
				-0.023
				-0.026
				-0.263
				0.703
				-0.093

1012 Twinning in Alpha - Resolved Shear Stress on Beta Twins (continued)

Alpha twinning direction	0	-1	1	1
Parallel direction in beta	1.622	0.6405	1.602	
Shear plane in alpha	0	1	-1	2
Parallel plane in beta	0.835	1.8167	-1.6	

Alpha twinning direction	1	-1	0	1
Parallel direction in beta	2.373	-0.11	0.13	
Shear plane in alpha	-1	1	0	2
Parallel plane in beta	0.085	2.567	-0.13	

Alpha twinning direction	-1	1	0	1
Parallel direction in beta	-0.11	2.373	-0.1	
Shear plane in alpha	1	-1	0	2
Parallel plane in beta	2.567	0.085	0.1	

Vectors of twinning shear direction

Plane	Direction			
3 3 -2	1	1	3	0.754
3 -3 2	-1	1	3	-0.498
-3 3 2	1	-1	3	-0.032
3 3 2	1	1	-3	0.662
3 -2 3	1	3	1	0.093
3 2 -3	-1	3	1	0.263
3 2 3	1	-3	1	-0.703
-3 2 3	1	3	-1	0.026
-2 3 3	3	1	1	0.023
2 3 3	-3	1	1	-0.306
2 3 -3	3	-1	1	0.733
2 -3 3	3	1	-1	0.029
				0.384
				0.339
				0.434
				0.377
				0.501
				0.356
				-0.44
				-0.49
				0.403
				0.403
				0.448
				-0.535
				-0.403
				0.403
				-0.45
				0.535
				-0.4
				0.377
				0.384
				0.403
				0.448
				-0.535
				-0.403
				0.403
				-0.356
				0.444
				-0.501

1012 Twinning in Alpha - Resolved Shear Stress on Martensite Shear System I

Alpha twinning direction	1	0	-1	1
Parallel direction in beta	1.882	0.381	-1.47	
Shear plane in alpha	-1	0	1	2
Parallel plane in beta	0.575	2.0762	1.472	

Alpha twinning direction	-1	0	1	1
Parallel direction in beta	0.381	1.882	1.472	
Shear plane in alpha	1	0	-1	2
Parallel plane in beta	2.076	0.575	-1.47	

Alpha twinning direction	0	1	-1	1
Parallel direction in beta	0.641	1.622	-1.6	
Shear plane in alpha	0	-1	1	2
Parallel plane in beta	1.817	0.835	1.6	

Vectors of martensite shear system I

Plane	Direction			
1	1	1	-1	
-1	1	-1	1	
1	-1	1	1	
1	1	-2	1	
1	2	1	1	
-1	2	1	-1	
1	-2	1	1	
1	2	-1	1	
2	1	1	-1	
-2	1	1	1	
2	-1	1	-1	
2	1	-1	1	

0.75	0.793		0.841
0.009	0.009		-0.446
-0.321	-0.32		-0.202
0.793	0.75		0.889
0.005	0.004		-0.282
0.59	0.677		0.259
-0.116	-0.16		-0.65
0.096	0.225		0.087
-0.225	-0.1		-0.115
-0.677	-0.59		-0.239
0.16	0.116		0.581
-0.004	-0.01		0.165

1012 Twinning in Alpha - Resolved Shear Stress on Martensite Shear System I (continued)

Alpha twinning direction	Alpha twinning direction	Alpha twinning direction
0 -1 1 1	1 -1 0 1	-1 1 0 1
Parallel direction in beta	Parallel direction in beta	Parallel direction in beta
1.622 0.6405 1.602	2.373 -0.11 0.13	-0.11 2.373 -0.1
Shear plane in alpha	Shear plane in alpha	Shear plane in alpha
0 1 -1 2	-1 1 0 2	1 -1 0 2
Parallel plane in beta	Parallel plane in beta	Parallel plane in beta
0.835 1.8167 -1.6	0.085 2.567 -0.13	2.567 0.085 0.1

Vectors of martensite shear system I

Plane	Direction			
1 1 2	1 1 -1	0.889	0.467	0.463
-1 1 2	1 -1 1	-0.446	0.447	0.447
1 -1 2	-1 1 1	-0.202	0.497	0.497
1 1 -2	1 1 1	0.841	0.463	0.467
1 2 1	1 -1 1	-0.165	0.282	0.165
-1 2 1	1 1 -1	0.239	0.14	0.25
1 -2 1	1 1 1	-0.581	-0.21	-0.326
1 2 -1	-1 1 1	0.115	-0.3	-0.196
2 1 1	-1 1 1	-0.087	0.196	0.301
-2 1 1	1 1 1	-0.259	-0.25	-0.14
2 -1 1	1 1 -1	0.65	0.326	0.213
2 1 -1	1 -1 1	0.282	-0.17	-0.282

1012 Twinning in Alpha - Resolved Shear Stress on Martensite Shear System II

Alpha twinning direction	1	0	-1	1
Parallel direction in beta	1.882	0.381	-1.47	
Shear plane in alpha	-1	0	1	2
Parallel plane in beta	0.575	2.0762	1.472	

Alpha twinning direction	-1	0	1	1
Parallel direction in beta	0.381	1.882	1.472	
Shear plane in alpha	1	0	-1	2
Parallel plane in beta	2.076	0.575	-1.47	

Alpha twinning direction	0	1	-1	1
Parallel direction in beta	0.641	1.622	-1.6	
Shear plane in alpha	0	-1	1	2
Parallel plane in beta	1.817	0.835	1.6	

Vectors of martensite shear system II

Plane	Direction				
1 0 1	1 1 -1	0.526	0.525	0.821	
1 0 1	-1 1 1	-0.315	-0.24	-0.183	
-1 0 1	1 -1 1	0.008	0.008	-0.353	
-1 0 1	1 1 1	-0.849	-0.77	-0.651	
1 1 0	1 -1 1	7E-04	-0	-0.068	
1 1 0	-1 1 1	-0.075	0.075	-0.016	
-1 1 0	1 1 -1	0.248	0.324	-0.186	
-1 1 0	1 1 1	-0.324	-0.25	0.237	
0 1 1	1 1 -1	0.774	0.849	0.635	
0 1 1	1 -1 1	0.008	0.008	-0.42	
0 -1 1	-1 1 1	-0.24	-0.32	-0.167	
0 -1 1	1 1 1	-0.525	-0.53	-0.889	

1012 Twinning in Alpha - Resolved Shear Stress on Martensite Shear System II (continued)

Alpha twinning direction	Alpha twinning direction	Alpha twinning direction
0 -1 1 1	1 -1 0 1	-1 1 0 1
Parallel direction in beta	Parallel direction in beta	Parallel direction in beta
1.622 0.6405 1.602	2.373 -0.11 0.13	-0.11 2.373 -0.1
Shear plane in alpha	Shear plane in alpha	Shear plane in alpha
0 1 -1 2	-1 1 0 2	1 -1 0 2
Parallel plane in beta	Parallel plane in beta	Parallel plane in beta
0.835 1.8167 -1.6	0.085 2.567 -0.13	2.567 0.085 0.1

Vectors of martensite shear system II

Plane	Direction			
1 0 1	1 1 -1	0.889	0.458	0.39
1 0 1	-1 1 1	-0.167	0.4	0.461
-1 0 1	1 -1 1	-0.42	0.354	0.421
-1 0 1	1 1 1	-0.635	-0.41	-0.351
1 1 0	1 -1 1	0.068	0.068	-0.068
1 1 0	-1 1 1	0.016	-0.06	0.061
-1 1 0	1 1 -1	-0.237	-0.11	0.021
-1 1 0	1 1 1	0.186	-0.02	0.107
0 1 1	1 1 -1	0.651	0.351	0.412
0 1 1	1 -1 1	-0.353	0.421	0.354
0 -1 1	-1 1 1	-0.183	0.461	0.4
0 -1 1	1 1 1	-0.821	-0.39	-0.458

Appendix H

Compliance Tensors of α and β Titanium

The original compliance tensor for α -Ti in units of 10^{-11} Pa^{-1} is:

0.9581	-0.4623	-0.1893	0	0	0
	0.9581	-0.1893	0	0	0
		0.6980	2.141	0	0
			2.141	0	0
				2.141	0
					2.938

The original compliance tensor for β -Ti in units of 10^{-11} Pa^{-1} is:

1.857	-0.774	-0.774	0	0	0
	1.857	-0.774	0	0	0
		1.857	0	0	0
			2.342	0	0
				2.342	0
					2.342

The transformed compliance tensor for α -Ti in units of 10^{-11} Pa^{-1} for the bi-crystal model is:

0.9581	-0.1893	-0.4623	0	0	0
	0.6980	-0.1893	0	0	0
		0.9581	0	0	0
			2.141	0	0
				2.8408	0
					2.1410

The transformed compliance tensor for the twinned α -Ti in units of 10^{-11} Pa^{-1} for the bi-crystal model is:

0.9581	-0.4623	-0.1893	0	0	0
	0.9581	-0.4623	0	0	0
		0.9581	0	0	0
			2.1410	0	0
				2.2948	0
					2.1410

The transformed compliance tensor for β -Ti in units of 10^{-11} Pa^{-1} for the bi-crystal model is:

0.9445	-0.4090	-0.2265	0	-0.3650	0
	1.1270	-0.4090	0	0.7300	0
		0.9445	0	-0.3650	0
			3.8020	0	1.460
				4.532	0
					2.342

Appendix I

Transformation Equations for Cubic Crystals

Direction Cosines:

	x	y	z
x'	l ₁	m ₁	n ₁
y'	l ₂	m ₂	n ₂
z'	l ₃	m ₃	n ₃

Transformation Equations:

$$S_C = S_{11} - S_{12} - \frac{S_{44}}{2}$$

$$S'_{11} = S_{11} - 2S_C(m_1^2 n_1^2 + l_1^2 n_1^2 + l_1^2 m_1^2)$$

$$S'_{12} = S_{12} + S_C(l_1^2 l_2^2 + m_1^2 m_2^2 + n_1^2 n_2^2)$$

$$S'_{13} = S_{12} + S_C(l_1^2 l_3^2 + m_1^2 m_3^2 + n_1^2 n_3^2)$$

$$S'_{14} = 2S_C(l_2 l_3 l_1^2 + m_2 m_3 m_1^2 + n_2 n_3 n_1^2)$$

$$S'_{15} = 2S_C(l_1^3 l_3 + m_1^3 m_3 + n_1^3 n_3)$$

$$S'_{16} = 2S_C(l_1^3 l_2 + m_1^3 m_2 + n_1^3 n_2)$$

$$S'_{22} = S_{11} - 2S_C(m_2^2 n_2^2 + l_2^2 n_2^2 + l_2^2 m_2^2)$$

$$S'_{23} = S_{12} + S_C(l_2^2 l_3^2 + m_2^2 m_3^2 + n_2^2 n_3^2)$$

$$S'_{24} = 2S_C(l_2^3 l_3 + m_2^3 m_3 + n_2^3 n_3)$$

$$S'_{25} = 2S_C(l_3 l_2^2 l_1 + m_3 m_2^2 m_1 + n_3 n_2^2 n_1)$$

$$S'_{26} = 2S_C(l_2^3 l_1 + m_2^3 m_1 + n_2^3 n_1)$$

$$\begin{aligned}
S'_{33} &= S_{11} - 2S_C(l_3^2 m_3^2 + l_3^2 n_3^2 + m_3^2 n_3^2) \\
S'_{34} &= 2S_C(l_3^3 l_2 + m_3^3 m_2 + n_3^3 n_2) \\
S'_{35} &= 2S_C(l_3^3 l_1 + m_3^3 m_1 + n_3^3 n_1) \\
S'_{36} &= 2S_C(l_1 l_3^2 l_2 + m_2 m_3^2 m_1 + n_2 n_3^2 n_1) \\
S'_{44} &= S_{44} + 4S_C(l_2^2 l_3^2 + m_2^2 m_3^2 + n_2^2 n_3^2) \\
S'_{45} &= 4S_C(l_1 l_2 l_3^2 + m_1 m_2 m_3^2 + n_1 n_2 n_3^2) \\
S'_{46} &= 4S_C(l_1 l_3 l_2^2 + m_1 m_3 m_2^2 + n_1 n_3 n_2^2) \\
S'_{55} &= S_{44} + 4S_C(l_1^2 l_3^2 + m_1^2 m_3^2 + n_1^2 n_3^2) \\
S'_{56} &= 4S_C(l_3 l_2 l_1^2 + m_3 m_2 m_1^2 + n_3 n_2 n_1^2) \\
S'_{66} &= S_{44} + 4S_C(l_1^2 l_2 l_3 + m_1^2 m_2 m_3 + n_1^2 n_2 n_3)
\end{aligned}$$

Transformation Equations for Hexagonal Crystals

Direction Cosines:

	x	y	z
x'	l ₁	m ₁	n ₁
y'	l ₂	m ₂	n ₂
z'	l ₃	m ₃	n ₃

Transformation Equations:

$$S_a = (S_{11} - 2S_{13} - S_{44} + S_{33})$$

$$S_h = \left(S_{11} - S_{13} - \frac{S_{44}}{2} \right)$$

$$S'_{11} = S_{11} + S_a n_1^4 - 2S_h n_1^2$$

$$S'_{12} = S_{13} + S_a n_1^2 n_2^2 + S_{12} (l_2 m_1 - l_1 m_2)^2 - S_{13} n_3^2$$

$$S'_{13} = S_{13} + S_a n_1^2 n_3^2 + S_{12} (l_3 m_1 - l_1 m_3)^2 - S_{13} n_2^2$$

$$S'_{14} = 2[S_a n_1^2 n_2 n_3 + S_{12} (m_1 l_2 - m_2 l_1)(m_1 l_3 - m_3 l_1) + S_{13} n_2 n_3]$$

$$S'_{15} = 2[S_a n_1^3 n_3 - S_h n_1 n_3]$$

$$S'_{16} = 2[S_a n_1^3 n_2 - S_h n_1 n_2]$$

$$S'_{22} = S_{11} + S_a n_2^4 - 2S_h n_2^2$$

$$S'_{23} = S_{13} + S_a n_2^2 n_3^2 + S_{12} (l_3 m_2 - l_2 m_3)^2 - S_{13} n_1^2$$

$$S'_{24} = 2[S_a n_2^3 n_3 - S_h n_2 n_3]$$

$$S'_{25} = 2[S_a n_2^2 n_1 n_3 + S_{12} (m_2 l_1 - m_1 l_2)(m_2 l_3 - m_3 l_2) + S_{13} n_1 n_3]$$

$$\begin{aligned}
S'_{26} &= 2[S_a n_2^3 n_1 - S_h n_2 n_1] \\
S'_{33} &= S_{11} + S_a n_3^4 - 2S_h n_3^2 \\
S'_{34} &= 2[S_a n_3^3 n_2 - S_h n_2 n_3] \\
S'_{35} &= 2[S_a n_3^4 n_1 - S_h n_3 n_1] \\
S'_{36} &= 2[S_a n_3^2 n_1 n_2 + S_{12}(m_3 l_2 - m_2 l_3)(m_3 l_1 - m_1 l_3) + S_{13} n_1 n_2] \\
S'_{44} &= S_{44} + 4S_a n_2^2 n_3^2 + 2(S_{11} - S_{12})(m_3 l_2 - m_2 l_3)^2 - S_{44} n_1^2 \\
S'_{45} &= 4S_a n_1 n_2 n_3^2 + 2(S_{11} + S_{12})(m_3 l_2 - m_2 l_3)(m_2 l_1 - m_1 l_2) \\
&\quad + (S_{44} - 4S_{11})n_1 n_2 \\
S'_{46} &= 4S_a n_1 n_3 n_2^2 + 2(S_{11} + S_{12})(m_3 l_2 - m_2 l_3)(m_2 l_1 - m_1 l_2) \\
&\quad + (S_{44} - 4S_{11})n_1 n_3 \\
S'_{55} &= S_{44} + 4S_a n_1^2 n_3^2 + 2(S_{11} - S_{12})(m_1 l_3 - m_3 l_1)^2 - S_{44} n_2^2 \\
S'_{56} &= 4S_a n_2 n_3 n_1^2 + 2(S_{11} + S_{12})(m_2 l_1 - m_1 l_2)(m_1 l_3 - m_3 l_1) \\
&\quad + (S_{44} - 4S_{11})n_2 n_3 \\
S'_{66} &= S_{44} + 4S_a n_1^2 n_2^2 + 2(S_{11} - S_{12})(m_2 l_1 - m_1 l_2)^2 - S_{44} n_3^2
\end{aligned}$$

Appendix J

ANSYS Operating Instructions for Simple Model Development

The following steps were used to build this model and run the simulation

- 1) Define Element Type
Preprocessor > Element Type > Add/Edit/Delete
The element type SOLID185 was selected.
- 2) Set Material Properties
Preprocessor > Material Props > Material Model
The elastic, linear, anisotropic model was selected. “Material 1” was set to the properties of the α phase. “Material 2” was set to the properties of the β phase. “Material 3” was set to the properties of the α twin.
- 3) Create Volumes
Preprocessor>Modeling>Create>Volumes>By Keypoints
- 4) Glue Areas
Preprocessor>Modeling>Operate>Booleans>Glue>Areas
The two areas created in step 3 were glued together to avoid issues with Node overlap.
- 5) Set Material Properties
Preprocessor>Meshing>Mesh Attributes>Picked Areas
Each area was picked separately and set to the material properties as listed above.
- 6) Create Mesh
Preprocessor > Meshing > Mesh Tool
The mesh tool was used to auto-generate the mesh for the piece.
- 7) Set Constrains
Preprocessor > Coupling/Ceqn > Couple DOFs
- 8) Define Loads and Displacements
Solution > Define Loads > Apply > On Nodes
- 9) Solve
Solution>Solve

References

1. Collings, E.W., *The Physical Metallurgy of Titanium Alloys*. 1984, Metals Park, OH: American Society for Metals.
2. Elliot, P., *Constitution of Binary Alloys, First Supplement*. 1965, New York: McGraw-Hill Inc. 617.
3. Grewal, G. and S. Ankem, *Solubility of Vanadium in Alpha-Titanium and Beta-Titanium*. Metallurgical Transactions a-Physical Metallurgy and Materials Science, 1989. **20**(2): p. 334-337.
4. Ankem, S., et al., *Mechanical properties of alloys consisting of two ductile phases*. Progress in Materials Science, 2006. **51**(5): p. 632-709.
5. Neuberger, B.W., Greene, C., Gute, G., *Creep Analyses of Titanium Drip Shield Subjected to Rockfall Static Loads in the Proposed Geologic Repository at Yucca Mountain*. Mat. Res. Soc. Symp. Proc., 2002. **716**: p. JJ11.7.1-JJ11.7.8.
6. *Air Force Technology F-35 Lightning II*. © Lockheed Martin Aeronautics Company 2011; Available from: <http://www.airforce-technology.com/projects/jsf/>.
7. *F-22 Raptor Team Website*. © Lockheed Martin Aeronautics Company 2009; Available from: <http://www.f22-raptor.com/>.
8. Akahori, T., et al., *Improvement in fatigue characteristics of newly developed beta type titanium alloy for biomedical applications by thermo-mechanical treatments*. Materials Science & Engineering C-Biomimetic and Supramolecular Systems, 2005. **25**(3): p. 248-254.
9. Ankem, S., *Unpublished Research*. University of Maryland, College Park, 2008. **Patent Pending**.
10. Cachinho, S.C.P. and R.N. Correia, *Titanium scaffolds for osteointegration: mechanical, in vitro and corrosion behaviour*. Journal of Materials Science-Materials in Medicine, 2008. **19**(1): p. 451-457.
11. Geetha, M., et al., *Ti based biomaterials, the ultimate choice for orthopaedic implants - A review*. Progress in Materials Science, 2009. **54**(3): p. 397-425.
12. Rack, H.J. and J.I. Qazi, *Titanium alloys for biomedical applications*. Materials Science & Engineering C-Biomimetic and Supramolecular Systems, 2006. **26**(8): p. 1269-1277.

13. Yamamoto, O., Alvarez, K., Kikuchi, T., Fukuda, M., *Fabrication and characterization of oxygen-diffused titanium for biomedical applications*. Acta Biomaterialia, 2009. **5**: p. 3605-3615.
14. Yamada, T., Kawabata, K., Sato, E., Kuribayashi, K., Jimbo, I., *Presences of primary creep in various phase metals and alloys at ambient temperature*. Materials Science and Engineering A, 2004. **387-389**: p. 719-722.
15. Aiyangar, A.K., et al., *The effects of stress level and grain size on the ambient temperature creep deformation behavior of an alpha Ti-1.6 wt pct V alloy*. Metallurgical and Materials Transactions a-Physical Metallurgy and Materials Science, 2005. **36A**(3): p. 637-644.
16. Ankem, S., C.A. Greene, and S. Singh, *Time-Dependent Twinning during Ambient-Temperature Creep of Alpha-Ti-Mn Alloy*. Scripta Metallurgica Et Materialia, 1994. **30**(6): p. 803-808.
17. Doraiswamy, D. and S. Ankem, *The effect of grain size and stability on ambient temperature tensile and creep deformation in metastable beta titanium alloys*. Acta Materialia, 2003. **51**(6): p. 1607-1619.
18. Greene, C.A., Ankem, S., *Ambient Temperature Tensile and Creep Deformation Behavior of Alpha and Beta Titanium Alloys*. Beta Titanium Alloys in the 1990's, ed. D. Eylon, Boyer, R.R., and Koss, D.A. 1993: TMS.
19. Greene, C.A., Ankem, S., Singh, S., *The Effect of Morphology and Alloying Elements on the Ambient Temperature Creep of Alpha and Alpha-Beta Titanium Alloys*. Proceedings of the Eighth World Conference on Titanium, 1995. **II**(Birmingham, U.K., Eds. P.A. Blenkinshop, W.J. Evans, and H.M. Flower): p. 1315-1322.
20. Hultgren, C.A., C.A. Greene, and S. Ankem, *Time-dependent twinning during ambient temperature compression creep of alpha Ti-0.4Mn alloy*. Metallurgical and Materials Transactions a-Physical Metallurgy and Materials Science, 1999. **30**(6): p. 1675-1679.
21. Jaworski, A. and S. Ankem, *Influence of the second phase on the room-temperature tensile and creep deformation mechanisms of alpha-beta titanium alloys: Part I. Tensile deformation*. Metallurgical and Materials Transactions a-Physical Metallurgy and Materials Science, 2006. **37A**(9): p. 2739-2754.
22. Jaworski, A. and S. Ankem, *Influence of the second phase on the room-temperature tensile and creep deformation mechanisms of alpha-beta titanium alloys, Part II: Creep deformation*. Metallurgical and Materials Transactions a-Physical Metallurgy and Materials Science, 2006. **37A**(9): p. 2755-2765.
23. Oberson, P.G. and S. Ankem, *Why twins do not grow at the speed of sound all the time*. Physical Review Letters, 2005. **95**(16): p. -.

24. Oberson, P.G. and S. Ankem, *The effect of time-dependent twinning on low temperature ($< 0.25 \cdot T_m$) creep of an alpha-titanium alloy*. International Journal of Plasticity, 2009. **25**(5): p. 881-900.
25. Ramesh, A. and S. Ankem, *The effect of grain size on the ambient temperature creep deformation behavior of a beta Ti-14.8 V alloy*. Metallurgical and Materials Transactions a-Physical Metallurgy and Materials Science, 2002. **33**(4): p. 1137-1144.
26. Ankem, S. and H. Margolin, *A Rationalization of Stress-Strain Behavior of 2-Ductile Phase Alloys*. Metallurgical Transactions a-Physical Metallurgy and Materials Science, 1986. **17**(12): p. 2209-2226.
27. Andenstedt, H., *Creep of Titanium at Room Temperature*. Metal Progress, 1949. **56**: p. 658.
28. Luster, D.R., Wentz, W.W., Kaufman, D.W., *Creep Properties of Titanium*. Materials and Methods, 1953. **37**: p. 100.
29. Thompson, A.W. and B.C. Odegard, *Influence of Microstructure on Low-Temperature Creep of Ti-5 Al-2.5 Sn*. Metallurgical Transactions, 1973. **4**(4): p. 899-908.
30. Chu, H.P., *Room Temperature Creep and Stress Relaxation of a Titanium Alloy*. Journal of Materials, 1970. **5**: p. 633.
31. Imam, M.A. and C.M. Gilmore, *Room-Temperature Creep of Ti-6al-4v*. Metallurgical Transactions a-Physical Metallurgy and Materials Science, 1979. **10**(4): p. 419-425.
32. Miller, W.H., R.T. Chen, and E.A. Starke, *Microstructure, Creep, and Tensile Deformation in Ti-6al-2nb-1ta-0.8mo*. Metallurgical Transactions a-Physical Metallurgy and Materials Science, 1987. **18**(8): p. 1451-1468.
33. Neeraj, T., et al., *Phenomenological and microstructural analysis of room temperature creep in titanium alloys*. Acta Materialia, 2000. **48**(6): p. 1225-1238.
34. Odegard, B.C. and A.W. Thompson, *Low-Temperature Creep of Ti-6 Al-4 V*. Metallurgical Transactions, 1974. **5**(5): p. 1207-1213.
35. Suri, S., et al., *Mechanisms of primary creep in alpha/beta titanium alloys at lower temperatures*. Materials Science and Engineering a-Structural Materials Properties Microstructure and Processing, 1997. **234**: p. 996-999.
36. Suri, S., et al., *Room temperature deformation and mechanisms of slip transmission in oriented single-colony crystals of an alpha/beta titanium alloy*. Acta Materialia, 1999. **47**(3): p. 1019-1034.

37. Greene, C.A., *Fundamental Studies on the Ambient Temperature Creep Deformation Behavior of Alpha, Beta, and Alpha-Beta Titanium Alloys*, in *Department of Materials Science and Engineering*. 1994, University of Maryland, College Park: College Park, MD. p. 92.
38. Huang, C. and M.H. Loretto, *The Microstructure and Creep-Behavior of Ti-25al-10nb-3v-1mo (Super a(2))*. *Materials Science and Engineering a-Structural Materials Properties Microstructure and Processing*, 1995. **193**: p. 722-728.
39. Ponsonnet, L., C. Quesne, and R. Penelle, *Microstructure and creep deformation of a near beta titanium alloy 'beta-CEZ'*. *Materials Science and Engineering a-Structural Materials Properties Microstructure and Processing*, 1999. **262**(1-2): p. 50-63.
40. Viswanathan, G.B., et al., *Creep behaviour of Ti-6Al-2Sn-4Zr-2Mo: II. Mechanisms of deformation*. *Acta Materialia*, 2002. **50**(20): p. 4965-4980.
41. Ankem, S. and H. Margolin, *Alpha-Beta Interface Sliding in Ti-Mn Alloys*. *Journal of Metals*, 1980. **32**(12): p. 38-38.
42. Christian, J.W. and S. Mahajan, *Deformation Twinning*. *Progress in Materials Science*, 1995. **39**(1-2): p. 1-157.
43. Song, S.G. and G.T. Gray, *Structural Interpretation of the Nucleation and Growth of Deformation Twins in Zr and Ti .1. Application of the Coincidence Site Lattice (Csl) Theory to Twinning Problems in Hcp Structures*. *Acta Metallurgica Et Materialia*, 1995. **43**(6): p. 2325-2337.
44. Song, S.G. and G.T. Gray, *Structural Interpretation of the Nucleation and Growth of Deformation Twins in Zr and Ti .2. Tem Study of Twin Morphology and Defect Reactions during Twinning*. *Acta Metallurgica Et Materialia*, 1995. **43**(6): p. 2339-2350.
45. Oberson, P.G., Z.W. Wyatt, and S. Ankem, *Modeling interstitial diffusion controlled twinning in alpha titanium during low-temperature creep*. *Scripta Materialia*, 2011. **65**: p. 638-641.
46. Liu, Z. and G. Welsch, *Literature Survey on Diffusivities of Oxygen, Aluminum, and Vanadium in Alpha-Titanium, Beta-Titanium, and in Rutile*. *Metallurgical Transactions a-Physical Metallurgy and Materials Science*, 1988. **19**(4): p. 1121-1124.
47. Aiyangar, A.K., et al., *The effects of stress level and grain size on the ambient temperature creep deformation behavior of an alpha Ti-1.6 wt pct V alloy*. *Metallurgical and Materials Transactions A*, 2005. **36A**(3): p. 637-644.

48. Gray, G.T., et al., *Influence of strain rate & temperature on the mechanical response of ultrafine-grained Cu, Ni, AND Al-4Cu-0.5Zr*. Nanostructured Materials, 1997. **9**(1-8): p. 477-480.
49. Grosdidier, T., et al., *Effect of microstructure variations on the formation of deformation-induced martensite and associated tensile properties in a beta metastable Ti alloy*. Metallurgical and Materials Transactions A, 2000. **31**(4): p. 1095-1106.
50. Meyers, M.A., O. Vohringer, and V.A. Lubarda, *The onset of twinning in metals: A constitutive description*. Acta Materialia, 2001. **49**(19): p. 4025-4039.
51. Ramesh, A. and S. Ankem, *The effect of grain size on the ambient temperature creep deformation behavior of a beta Ti-14.8 V alloy*. Metallurgical and Materials Transactions A, 2002. **33**(4): p. 1137-1144.
52. Thompson, A.W. and B.C. Odegard, *Influence of Microstructure on Low-Temperature Creep of Ti-5 Al-2.5 Sn*. Metallurgical Transactions A, 1973. **4**(4): p. 899-908.
53. Wyatt, Z.W. and S. Ankem, *Advances in Low Temperature (<0.25T_m) Creep Deformation Mechanisms of alpha, alpha + beta, and beta Titanium Alloys*. The Proceedings of the 12th World Conference on Titanium, 2011.
54. Edington, J.W., *Practical Electron Microscopy in Materials Science*. Out of Print ed. 1976, Marietta, OH: CBLIS Publisher & Book Distributor. 344.
55. Dieter, E., *Mechanical Metallurgy*. Third Edition. 1986, New York: McGraw-Hill Book Company. 439.
56. Chichili, D.R., K.T. Ramesh, and K.J. Hemker, *The high-strain-rate response of alpha-titanium: Experiments, deformation mechanisms and modeling*. Acta Materialia, 1998. **46**(3): p. 1025-1043.
57. Nemat-Nasser, S., W.G. Guo, and J.Y. Cheng, *Mechanical properties and deformation mechanisms of a commercially pure titanium*. Acta Materialia, 1999. **47**(13): p. 3705-3720.
58. Ramesh, K.T., *Effects of high rates of loading on the deformation behavior and failure mechanisms of hexagonal close-packed metals and alloys*. Metallurgical and Materials Transactions a-Physical Metallurgy and Materials Science, 2002. **33**(3): p. 927-935.
59. Zhou, W. and K.G. Chew, *The rate dependent response of a titanium alloy subjected to quasi-static loading in ambient environment*. Journal of Materials Science, 2002. **37**(23): p. 5159-5165.

60. Zeng, Z.P., S. Jonsson, and H.J. Roven, *The effects of deformation conditions on microstructure and texture of commercially pure Ti*. Acta Materialia, 2009. **57**(19): p. 5822-5833.
61. Conrad, H., *Effect of Interstitial Solutes on the Strength and Ductility of Titanium*. Progress in Materials Science, 1981. **26**(2-4): p. 123-404.
62. Williams, J.C., R.G. Baggerly, and N.E. Paton, *Deformation behavior of HCPTi-Al alloy single crystals*. Metallurgical and Materials Transactions a-Physical Metallurgy and Materials Science, 2002. **33**(3): p. 837-850.
63. Zaefferer, S., *A study of active deformation systems in titanium alloys: dependence on alloy composition and correlation with deformation texture*. Materials Science and Engineering a-Structural Materials Properties Microstructure and Processing, 2003. **344**(1-2): p. 20-30.
64. Dieter, G.E., *Mechanical Metallurgy*. 1988, London: McGraw-Hill Book Co. 708.
65. Reed-Hill, R., Abbaschian, R., *Physical Metallurgy Principles*. 1992, Boston: PWS-Kent.
66. Song, S.G. and G.T. Gray, *Influence of Temperature and Strain-Rate on Slip and Twinning Behavior of Zr*. Metallurgical and Materials Transactions a-Physical Metallurgy and Materials Science, 1995. **26**(10): p. 2665-2675.
67. Shan, Z.W., et al., *The effect of twin plane spacing on the deformation of copper containing a high density of growth twins*. Jom, 2008. **60**(9): p. 71-74.
68. Charit, I., S. Gollapudi, and K.L. Murty, *Creep mechanisms in Ti-3Al-2.5V alloy tubing deformed under closed-end internal gas pressurization*. Acta Materialia, 2008. **56**(10): p. 2406-2419.
69. Savrun, E., W.D. Scott, and D.C. Harris, *The effect of titanium doping on the high-temperature rhombohedral twinning of sapphire*. Journal of Materials Science, 2001. **36**(9): p. 2295-2301.
70. Yoo, M.H., *Twinning and mechanical behavior of titanium aluminides and other intermetallics*. Intermetallics, 1998. **6**(7-8): p. 597-602.
71. Karthikeyan, S. and M.J. Mills, *The role of microstructural stability on compression creep of fully lamellar gamma-TiAl alloys*. Intermetallics, 2005. **13**(9): p. 985-992.
72. Chen, M.W., et al., *Deformation twinning in nanocrystalline aluminum*. Science, 2003. **300**(5623): p. 1275-1277.
73. Dorosinskii, L.A., et al., *Kinetics of the Changes in the Twin Structure in Yba2cu3o7-X Single-Crystals*. Jetp Letters, 1989. **49**(3): p. 182-187.

74. Dorosinskii, L.A., et al., *Kinetics of Twin Boundary Migration in Yba2cu3o7-X Single-Crystals*. Physica C, 1992. **203**(3-4): p. 342-346.
75. Salje, E.K.H., et al., *Needle twins and right-angled twins in minerals: Comparison between experiment and theory*. American Mineralogist, 1998. **83**(7-8): p. 811-822.
76. Gumbsch, P. and H. Gao, *Dislocations faster than the speed of sound*. Science, 1999. **283**(5404): p. 965-968.
77. Zerilli, F.J. and R.W. Armstrong, *Dislocation mechanics based analysis of material dynamics behavior: Enhanced ductility, deformation twinning, shock deformation, shear instability, dynamic recovery*. Journal De Physique Iv, 1997. **7**(C3): p. 637-642.
78. Kalidindi, S.R., *Incorporation of deformation twinning in crystal plasticity models*. Journal of the Mechanics and Physics of Solids, 1998. **46**(2): p. 267-+.
79. Tome, C.N.e.a., *Symposium on HCP Metals*. TMS/AIME, 2001. **New Orleans**.
80. Bevis, M. and A.G. Crocker, *Twinning Shears in Lattices*. Proceedings of the Royal Society of London Series a-Mathematical and Physical Sciences, 1968. **304**(1476): p. 123-&.
81. Partridge, P.G., *The crystallography of deformation modes of hexagonal close-packed metals*. Metallurgical Reviews, 1967. **118**: p. 169-194
82. Pond, R.C., et al., *The Crystallography and Atomic-Structure of Line Defects in Twin Boundaries in Hexagonal-Close-Packed Metals*. Metallurgical Transactions a-Physical Metallurgy and Materials Science, 1991. **22**(6): p. 1185-1196.
83. Serra, A., D.J. Bacon, and R.C. Pond, *The Crystallography and Core Structure of Twinning Dislocations in Hcp Metals*. Acta Metallurgica, 1988. **36**(12): p. 3183-3203.
84. Yoo, M.H. and J.K. Lee, *Deformation Twinning in Hcp Metals and Alloys*. Philosophical Magazine a-Physics of Condensed Matter Structure Defects and Mechanical Properties, 1991. **63**(5): p. 987-1000.
85. McCabe, R.J., et al., *Quantitative analysis of deformation twinning in zirconium*. International Journal of Plasticity, 2009. **25**(3): p. 454-472.
86. Crocker, A.G., *Twinned Martensite*. Acta Metallurgica, 1962. **10**(Feb): p. 113-&.
87. Crocker, A.G.a.B., M., *The Science, Technology, and Application of Titanium*, ed. R.I.J.a.N.E. Promisel. 1968, London.

88. Oberson, P.G., *An Experimental and Theoretical Investigation of the Low Temperature Creep Deformation Behavior of Single Phase Titanium Alloys*, in *Department of Materials Science and Engineering*. 2006, University of Maryland: College Park, Maryland, USA. p. 208.
89. Cerreta, E., Gray, G.T., Lawson, A.C., Morris, C.E., Mason, T.A., Hixson, R.S., Rigg, P.A., *The Influence of Oxygen Content on the Pressure Induced Phase Transformation and Shock Hardening of Titanium*. *Journal of Applied Physics*, 2006. **100**: p. 0135301-9.
90. Cerreta, E., et al., *The influence of interstitial oxygen and peak pressure on the shock loading behavior of zirconium*. *Acta Materialia*, 2005. **53**(6): p. 1751-1758.
91. Khan, A.S., et al., *Effect of oxygen content and microstructure on the thermo-mechanical response of three Ti-6Al-4V alloys: Experiments and modeling over a wide range of strain-rates and temperatures*. *International Journal of Plasticity*, 2007. **23**(7): p. 1105-1125.
92. Greene, C.A., *PhD Dissertation: Fundamental studies on ambient temperature creep deformation behavior of alpha and alpha-beta titanium alloys*, in *Department of Materials Science and Engineering*. 1994, University of Maryland, College Park: College Park, MD.
93. Conrad, H., *Rate Controlling Mechanism during Yielding and Flow of Alpha-Titanium at Temperatures Below 0.4 T_m*. *Acta Metallurgica*, 1966. **14**(11): p. 1631-&.
94. Capolungo, L., et al., *On the interaction between slip dislocations and twins in HCP Zr*. *Materials Science and Engineering a-Structural Materials Properties Microstructure and Processing*, 2009. **513-14**: p. 42-51.
95. Xiao, G.H., N.R. Tao, and K. Lu, *Effects of strain, strain rate and temperature on deformation twinning in a Cu-Zn alloy*. *Scripta Materialia*, 2008. **59**(9): p. 975-978.
96. Lu, K., et al., *Effect of the Zener-Hollomon parameter on the microstructures and mechanical properties of Cu subjected to plastic deformation*. *Acta Materialia*, 2009. **57**(3): p. 761-772.
97. Li, B. and E. Ma, *Atomic Shuffling Dominated Mechanism for Deformation Twinning in Magnesium*. *Physical Review Letters*, 2009. **103**(3): p. -.
98. Porter, D.A. and K.E. Easterling, *Phase Transformations in Metals and Alloys*. Vol. 2nd ed. 1993, London: Chapman & Hall.
99. Moriya, N., et al., *Boron-Diffusion in Strained Si1-Xgex Epitaxial Layers*. *Physical Review Letters*, 1993. **71**(6): p. 883-886.

100. Baumann, F.H., et al., *Multilayers as Microlabs for Point-Defects - Effect of Strain on Diffusion in Semiconductors*. Physical Review Letters, 1994. **73**(3): p. 448-451.
101. Cowern, N.E.B., et al., *Diffusion in Strained Si(Ge)*. Physical Review Letters, 1994. **72**(16): p. 2585-2588.
102. Kuo, P., et al., *Comparison of Boron-Diffusion in Si and Strained Si_{1-x}Ge_x Epitaxial Layers*. Applied Physics Letters, 1993. **62**(6): p. 612-614.
103. Armstrong, R.W. and S.M. Walley, *High strain rate properties of metals and alloys*. International Materials Reviews, 2008. **53**(3): p. 105-128.
104. Mostafa, M.M., *Stress Enhanced Diffusion Process in Al-10wt-Percent Zn Alloy*. Czechoslovak Journal of Physics, 1991. **41**(9): p. 865-870.
105. Nazarov, A.V. and A.A. Mikheev, *Theory of diffusion under stress in interstitial alloys*. Physica Scripta, 2004. **T108**: p. 90-94.
106. Aziz, M.J., et al., *Pressure and stress effects on the diffusion of B and Sb in Si and Si-Ge alloys*. Physical Review B, 2006. **73**(5).
107. Aziz, M.J., *Pressure and stress effects on diffusion in Si*. Defect and Diffusion Forum, 1998. **153**: p. 1-10.
108. Aziz, M.J., *Thermodynamics of diffusion under pressure and stress: Relation to point defect mechanisms*. Applied Physics Letters, 1997. **70**(21): p. 2810-2812.
109. Aziz, M.J., *Stress effects on defects and dopant diffusion in Si*. Materials Science in Semiconductor Processing, 2001. **4**(5): p. 397-403.
110. Salem, A.A., S.R. Kalidindi, and R.D. Doherty, *Strain hardening of titanium: role of deformation twinning*. Acta Materialia, 2003. **51**(14): p. 4225-4237.
111. Salem, A.A., et al., *Strain hardening due to deformation twinning in alpha-titanium: Mechanisms*. Metallurgical and Materials Transactions a-Physical Metallurgy and Materials Science, 2006. **37A**(1): p. 259-268.
112. Salem, A.A., S.R. Kalidindi, and S.L. Semiatin, *Strain hardening due to deformation twinning in alpha-titanium: Constitutive relations and crystal-plasticity modeling*. Acta Materialia, 2005. **53**(12): p. 3495-3502.
113. Mahajan, S., et al., *Formation of annealing twins in f.c.c. crystals*. Acta Materialia, 1997. **45**(6): p. 2633-2638.
114. Pande, C.S., M.A. Imam, and B.B. Rath, *Study of Annealing Twins in Fcc Metals and Alloys*. Metallurgical Transactions a-Physical Metallurgy and Materials Science, 1990. **21**(11): p. 2891-2896.

115. Follansbee, P.S. and G.T. Gray, *An Analysis of the Low-Temperature, Low and High Strain-Rate Deformation of Ti-6al-4v*. Metallurgical Transactions a-Physical Metallurgy and Materials Science, 1989. **20**(5): p. 863-874.
116. Wiezorek, J.M.K., et al., *Deformation mechanisms in a binary Ti-48 at.%Al alloy with lamellar microstructure*. Philosophical Magazine Letters, 1997. **75**(5): p. 271-280.
117. Bania, P.J., *Beta-Titanium Alloys and Their Role in the Titanium Industry*. Jom-Journal of the Minerals Metals & Materials Society, 1994. **46**(7): p. 16-19.
118. Brotzen, F.R., E.L. Harmon, and A.R. Troiano, *Decomposition of Beta Titanium*. Transactions of the American Institute of Mining and Metallurgical Engineers, 1955. **203**(2): p. 413-419.
119. Greene, C.A., Ankem, S., *Beta Titanium Alloys in the 1990's*, ed. D.B. Eylon, R.R., Koss, D.A. 1993, Warrendale, PA: TMS.
120. Grosdidier, T., et al., *Effect of microstructure variations on the formation of deformation-induced martensite and associated tensile properties in a beta metastable Ti alloy*. Metallurgical and Materials Transactions a-Physical Metallurgy and Materials Science, 2000. **31**(4): p. 1095-1106.
121. Karasevskaya, O.P., et al., *Deformation behavior of beta-titanium alloys*. Materials Science and Engineering a-Structural Materials Properties Microstructure and Processing, 2003. **354**(1-2): p. 121-132.
122. Kim, H.S., et al., *Stress-induced martensitic transformation of metastable beta-titanium alloy*. Materials Science and Engineering a-Structural Materials Properties Microstructure and Processing, 2007. **449**: p. 322-325.
123. Koul, M.K. and J.F. Breedis, *Phase Transformations in Beta Isomorphous Titanium Alloys*. Acta Metallurgica, 1970. **18**(6): p. 579-&.
124. Ling, F.W., E.A. Starke, and B.G. Lefevre, *Deformation Behavior and Texture Development in Beta Ti-V Alloys*. Metallurgical Transactions, 1974. **5**(1): p. 179-187.
125. Paris, H.G., B.G. Lefevre, and E.A. Starke, *Deformation Behavior in Quenched and Aged Beta Ti-V Alloys*. Metallurgical Transactions a-Physical Metallurgy and Materials Science, 1976. **7**(2): p. 273-278.
126. Sil, D., Greene, C.A., Ankem, S., *Les Alliages Des Titane Beta*, ed. A. Vassel, Eylon, D., Combres, Y. 1994: Soceite Francaise de Metallurgie et de Materiaux.
127. Weiss, I. and S.L. Semiatin, *Thermomechanical processing of beta titanium alloys - an overview*. Materials Science and Engineering a-Structural Materials Properties Microstructure and Processing, 1998. **243**(1-2): p. 46-65.

128. Xu, W., et al., *Phase stability and its effect on the deformation behavior of Ti-Nb-Ta-In/Cr beta alloys*. Scripta Materialia, 2006. **54**(11): p. 1943-1948.
129. Zhao, Y.Q., S.W. Xin, and W.D. Zeng, *Effect of major alloying elements on microstructure and mechanical properties of a highly beta stabilized titanium alloy*. Journal of Alloys and Compounds, 2009. **481**(1-2): p. 190-194.
130. Ivasishin, O.M., et al., *Aging response of coarse- and fine-grained beta titanium alloys*. Materials Science and Engineering a-Structural Materials Properties Microstructure and Processing, 2005. **405**(1-2): p. 296-305.
131. Ankem, S. and H. Margolin, *Alpha-Beta Interface Sliding in Ti-Mn Alloys*. Metallurgical Transactions a-Physical Metallurgy and Materials Science, 1983. **14**(3): p. 500-503.
132. Ankem, S., et al., *The Effect of Volume Per Cent of Phases on the High-Temperature Tensile Deformation of 2-Phase Ti-Mn Alloys*. Materials Science and Engineering a-Structural Materials Properties Microstructure and Processing, 1989. **111**: p. 51-61.
133. Greene, C.A., *Fundamental Studies on Ambient Temperature Creep Deformation Behavior of Alpha and Alpha-Beta Titanium Alloys*, in *Materials Science and Engineering*. 1994, University of Maryland: College Park.
134. Grewal, G. and S. Ankem, *Isothermal Particle Growth in 2-Phase Titanium-Alloys*. Metallurgical Transactions a-Physical Metallurgy and Materials Science, 1989. **20**(1): p. 39-54.
135. Jepson, K.S., Brown, A.R.G., Gray, J.A. *The Science Technology and Application of Titanium*. in *Proceedings of the First International Conference on Titanium*. 1970. London: Pergamon Press.
136. Balcerza, At and S.L. Sass, *Formation of Omega- Phase in Ti-Nb Alloys*. Metallurgical Transactions, 1972. **3**(6): p. 1601-&.
137. Sass, S.L., *Structure and Decomposition of Zr and Ti Bcc Solid-Solutions*. Journal of the Less-Common Metals, 1972. **28**(1): p. 157-&.
138. Silcock, J.M., *An X-Ray Examination of the Omega-Phase in Tiv, Timo and Ticr Alloys*. Acta Metallurgica, 1958. **6**(7): p. 481-493.
139. Kuan, T.S., R.R. Ahrens, and S.L. Sass, *Stress-Induced Omega Phase-Transformation in Ti-V Alloys*. Metallurgical Transactions a-Physical Metallurgy and Materials Science, 1975. **6**(9): p. 1767-1774.
140. Partridg, Pg and R.W. Gardiner, *Indices of Planes and Directions in Hcp Crystals*. Acta Metallurgica, 1967. **15**(2): p. 387-&.

141. Bowen, A.W., *Omega Phase Embrittlement in Aged Ti-15 Percent Mo*. Scripta Metallurgica, 1971. **5**(8): p. 709-&.
142. Bowen, A.W., *Effect of Heat-Treatment on Fracture Toughness of a Ti-15mo Alloy*. Metals Technology, 1978. **5**(Jan): p. 17-23.
143. Gysler, A., Lutjerin.G, and V. Gerold, *Deformation Behavior of Age-Hardened Ti-Mo Alloys*. Acta Metallurgica, 1974. **22**(7): p. 901-909.
144. Williams, J.C., B.S. Hickman, and H.L. Marcus, *Effect of Omega Phase on Mechanical Properties of Titanium Alloys*. Metallurgical Transactions, 1971. **2**(7): p. 1913-&.
145. Greene, C.A., Ankem, S., Singh, S. *The Effect of Morphology and Alloying Elements on the Ambient Temperature Creep of Alpha and Alpha-Beta Titanium Alloys*. in *Proceedings of the Eighth World Conference on Titanium*. 1995. Birmingham, U.K.
146. Gerland, M., et al., *Deformation and damage mechanisms in an alpha/beta 6242 Ti alloy in fatigue, dwell-fatigue and creep at room temperature. Influence of internal hydrogen*. Materials Science and Engineering a-Structural Materials Properties Microstructure and Processing, 2009. **507**(1-2): p. 132-143.
147. Guo, Z., et al., *Influence of stacking-fault energy on high temperature creep of alpha titanium alloys*. Scripta Materialia, 2006. **54**(12): p. 2175-2178.
148. Malakondaiah, G. and P.R. Rao, *Creep of Alpha-Titanium at Low Stresses*. Acta Metallurgica, 1981. **29**(7): p. 1263-1275.
149. Smith, D.J. and R.L. Jones, *The Uniaxial Rate-Dependent Deformation-Behavior of Alpha-Titanium at Room-Temperature*. Mechanics of Materials, 1989. **8**(2-3): p. 219-235.
150. Seward, G.G.E., et al., *In situ SEM-EBSD observations of the hcp to bcc phase transformation in commercially pure titanium*. Acta Materialia, 2004. **52**(4): p. 821-832.
151. Oka, M. and Y. Taniguchi, *[332] Deformation Twins in a Ti-15.5 Pct-V Alloy*. Metallurgical Transactions a-Physical Metallurgy and Materials Science, 1979. **10**(5): p. 651-653.
152. Ramesh, A., *Effect of Stability and Grain Size on Ambient Temperature Tensile and Creep Behavior of Beta Titanium Alloys*, in *Materials Science and Engineering*. 1998, University of Maryland: College Park. p. 162.
153. Grosdidier, T. and M.J. Philippe, *Deformation induced martensite and superelasticity in a beta-metastable titanium alloy*. Materials Science and

- Engineering a-Structural Materials Properties Microstructure and Processing, 2000. **291**(1-2): p. 218-223.
154. Williams, B., Carter, CB, *Transmission Electron Microscopy*. Vol. II. 1996, New York: Plenum Press.
 155. Menon, E.S.K. and R. Krishnan, *Phase-Transformations in Ti-V Alloys .I. Martensitic Transformations*. Journal of Materials Science, 1983. **18**(2): p. 365-374.
 156. Jaworski, A. and S. Ankem, *Influence of the omega phase on the tensile and creep deformation mechanisms of alpha-beta titanium alloys*. Reviews on Advanced Materials Science, 2005. **10**(1): p. 11-20.
 157. Ankem, S. and H. Margolin, *The Role of Elastic Interaction Stresses on the Onset of Plastic-Flow for Oriented 2 Ductile Phase Structures*. Metallurgical Transactions a-Physical Metallurgy and Materials Science, 1980. **11**(6): p. 963-972.
 158. Ankem, S. and H. Margolin, *Modeling Deformation in 2-Phase Alloys*. Journal of Metals, 1986. **38**(4): p. 25-29.
 159. Greene, C.A. and S. Ankem, *Modeling of Elastic Interaction Stresses in 2-Phase Materials by Fem*. Materials Science and Engineering a-Structural Materials Properties Microstructure and Processing, 1995. **202**(1-2): p. 103-111.
 160. *ANSYS Manual-Engineering Analysis System*. 2005, Swanson Analysis Systems (SAS) Inc.
 161. Flowers Jr, J.W., Brien, K.C.O., McElency, P.C., *Elastic Constants of Alpha-Titanium single crystals at 25C*. Journal of Less Common Metals, 1964. **7**.
 162. Ikehata, H., et al., *First-principles calculations for development of low elastic modulus Ti alloys*. Physical Review B, 2004. **70**(17).
 163. Fisher, E.S., Dever, D., Jaffee, R.I. and Promisel, N.E. (eds.), *The Science, Technology, and Applications of Titanium*. 1968, New York: Pergamon Press. 373.
 164. Greene, C.A., *Finite Element Method (FEM) Modeling of Elastic Interaction Stresses in Two-Phase Materials*, in *Department of Materials Science and Engineering*. 1992, University of Maryland, College Park: College Park, MD. p. 94.
 165. Nye, J.F., *Physical Properties of Crystals*. 2nd ed. 1985, New York: Oxford University Press.

Zane W. Wyatt

zane.w.wyatt@gmail.com

Mobile: (443) 844-0185

10141 Tanfield Ct.
Ellicott City, MD 20142
United States Citizen

Education:

- University of Maryland, College Park, MD.
Ph.D. Materials Science and Engineering, GPA: 3.91/4.00 **November 2011**
“The Effect of Phase Constitution and Morphology on Room Temperature Deformation Behavior of Two-Phase Titanium Alloys”
- University of Maryland, College Park, MD.
M.S. Materials Science and Engineering, GPA: 3.90/4.00 **May 2010**
“The Effect of Metastability on Room Temperature Deformation Behavior of Beta and Alpha + Beta Titanium Alloys”
- University of Utah, Salt Lake City, UT.
B.S. Metallurgical Engineering, GPA: 3.80/4.00 **May 2007**
“An Investigation into the Ballistic Performance of a Titanium-Boride (TiB) Personal Body Armor Material”

Employment Experience:

- Materials Engineering Intern **May – August 2006**
Caterpillar Inc. (CAT: NYSE), Peoria, IL
Performed statistical reliability study on debris damage of alloyed titanium turbocharger compressor wheels for large displacement engines
Developed a IE Spec to dictate internal manufacturing requirements for high-temperature enamel exhaust manifold coatings
- Bicycle Mechanic/Ski Tuner **April 2009 - Current**
Princeton Sports, Columbia, MD
- Ski-Lift Operator **Winter 2004-05/2006-07**
Park City Mountain Resort, Park City, UT
- Farm Hand **Summer 2003/2004**
Idaho Trout Co., Buhl, ID

Publications and Awards:

- 1) Wyatt, Z.W., Zhu, D., Ankem, S., “Deformation mechanisms and kinetics of time-dependent twinning in an alpha-titanium alloy”, Submitted to the *International Journal of Plasticity*.
 - 2) Oberson, P.G., Wyatt, Z.W., Ankem, S., “Modeling interstitial diffusion controlled twinning in alpha titanium during low-temperature creep”, *Scripta Materialia* 65 (2011) 638 – 641.
 - 3) Wyatt, Z.W., Ankem, S., “Advances in low temperature (<0.25T_m) creep deformation mechanisms of alpha, alpha + beta, and beta titanium alloys”, The Conference Proceedings of the 12th World Conference on Titanium (Ti-2011).
 - 4) Wyatt, Z.W., Ankem, S., “Recent developments in mechanisms and the kinetics of deformation twinning in titanium alloys”, *Materials Science Forum* 654 – 656 (2010) 863 – 866.
 - 5) Wyatt, Z.W., Ankem, S., “The effect of metastability on room temperature deformation behavior of beta and alpha + beta titanium alloys”, *Journal of Materials Science* 45(18) (2010) 5022 – 5031.
- Oblad Silver Medal of Excellence for Outstanding Research, University of Utah, May 2007
 - College of Mines & Earth Sciences Top Ranked Student, University of Utah, May 2005, 2006, 2007

Other Pertinent Experience:

- ANSYS Finite Element Method simulations of phase interaction stresses in two-phase titanium alloys